

Imaging the North Anatolian Fault Zone

with

Fault Zone Head Waves,

Reflected and Converted Phases

Inaugural-Dissertation

to obtain the academic degree

Doctor rerum naturalium (Dr. rer. nat.)

submitted to the Department of Earth Sciences

of Freie Universität Berlin

by

Seyedehtita Najdahmadi

Berlin, June 2017

Eidesstattliche Erklärung

Ich erkläre hiermit an Eides statt, dass ich die vorliegende Dissertation selbstständig und nur unter Verwendung der angegebenen Quellen und Hilfsmittel angefertigt habe.

Berlin, den 08.06.2017

Referent	Prof. Dr. Marco Bohnhoff
Korreferent	Prof. Dr. Serge A. Shapiro
Datum der Disputation	18.07.2017



Freie Universität Berlin
Fachbereich Geowissenschaften
Institut für Geologische Wissenschaften
Malteserstr. 74 – 100
12249 Berlin

Summary

Complex seismograms consist of different phases, that can be generated while waveforms travel through the heterogeneous subsurface from source to receiver. Analyzing these phases can help to image and interpret the structures of the Earth's crust within faults with special features such as bimaterial interfaces.

In the first study of this thesis, I imaged the velocity contrast (bimaterial interface) along the Karadere fault of the North Anatolian Fault Zone (NAFZ), which is located at the eastern part of the 1999 Izmit Mw7.4 rupture in NW Turkey, using waveforms recorded by a local seismic network. By applying an automatic procedure for identification and picking arrival times of fault zone head waves (FZHW) and direct P waves, and manually revising the picks through particle motion analysis, two different groups of FZHW as well as fault zone reflected waves (FZRW) are identified. The first group of FZHW has a moveout with respect to the direct P arrivals with distance traveled along the fault, indicating a deep bimaterial interface down to the base of the seismogenic crust with an average velocity contrast of ~3.4%. The second group of FZHW has a constant travel-time difference with respect to the direct P wave irrespective of the distance traveled along the fault, and is associated with a shallow local interface bounding a low velocity damage zone or basin structure that extends to a depth of 4-5 km. While the first group of FZHW can only be observed on the slower crustal block, the second group of FZHW and the FZRW are present generally on both sides of the fault. These phases add to the richness and complexity of the early P waveforms observed at stations close to a large fault. The relatively low velocity contrast across the Karadere fault compared to values to the west may have helped stopping the Izmit rupture.

In the second study that I performed in this thesis, waveforms of local seismicity occurring before, between, and after the two consecutive 1999 Mw > 7 İzmit and Düzce earthquakes were analyzed. The waveforms were recorded at three seismic stations located around the Mudurnu segment of the North Anatolian Fault Zone. The main focus is on the interpretation of two distinct secondary phases contained in the P-wave coda that are well separated from the direct P wave. The phases are produced by a structure near the stations, because they are visible at all waveforms and have a constant travel-time difference to the direct P-wave arrivals irrespective of epicentral distance, hypocentral depth, or back-azimuth. Based on

a polarization analysis, the major secondary phase is a PS-converted wave. Its particle motion is consistent with the particle motion of the direct S wave and displays shear-wave splitting produced by the anisotropic upper crust. The particle motion of the minor secondary phase is nearly vertical and consistent with the particle motion of the P wave. Synthetic modeling indicates that the PS phase is converted at a horizontal interface at a depth of ~ 4 km. The role of the steep Mudurnu fault zone as a generator of the PS reflected conversions at shallow depths is discussed. This interpretation is in agreement with the near-surface setting indicating a juvenile pull-apart structure along the Mudurnu fault and fits well into the eastward progressing transtensional tectonic setting known for the region.

The results of the two studies performed in this thesis show the potential of phases (FZHW, reflected and/or converted phases) to image near fault structures. In particular, it was shown that techniques applied allowed to image the Karadere fault and the near-vertical Mudurnu fault along the NAFZ in NW Turkey. The results imply that such studies serve to analyze near-fault recordings and to determine potential hazard-prone faults, thereby contributing to a better constrain of future rupture planes and associated seismic hazard and risk.

Zusammenfassung

Komplexe Seismogramme bestehen aus verschiedenen Phasen, die während der Ausbreitung von elastischen Wellen durch den heterogenen Untergrund von Quelle zu Empfänger erzeugt werden können. Die Analyse dieser Phasen kann dazu beitragen, die Geometrie und Geschwindigkeitsstruktur der Erdkruste oder von Verwerfungen zu identifizieren.

In der ersten Studie dieser Dissertation untersuche ich die Geometrie und einen Geschwindigkeitskontrast entlang des Karadere-Segments der Nordanatolischen Verwerfungszone (NAFZ). Das Karadere-Segment befindet sich innerhalb der Izmit-Düzce-Bruchzone östlich von Istanbul, zwischen den Epizentren der Izmit- und Düzce-Beben von 1999 im Nordwesten der Türkei. Es wurden entlang der Verwerfungszone geführte Wellen (Fault Zone Head Waves; Abkürzung: FZHW) und P-Wellen untersucht. FZHW, P-Wellen und deren Ankunftszeiten wurden automatisch detektiert und gepickt. Anschließend wurden die automatischen Detektionen der FZHW- und P-Wellen unter Einsatz einer Polarisationsanalyse manuell überprüft. Hierbei wurden erstmals zwei verschiedene Gruppen von FZHW, sowie eine Gruppe von an der Verwerfungszone reflektierten Wellen (Fault Zone Reflected Waves; Abkürzung: FZRW) identifiziert: Die erste Gruppe von FZHW weist einen Moveout auf, also einen mit der Epizentralentfernung wachsenden Laufzeitunterschied zwischen FZHW und P-Welle. Dies weist auf einen Geschwindigkeitskontrast von $\sim 3,4\%$ in der seismogenen Tiefe des Karadere-Segments hin. Bei der zweiten Gruppe von FZHW bleibt der Laufzeitunterschied zwischen FZHW und P-Welle mit zunehmender Entfernung zur Störung konstant, wobei FZHW an Stationen zu beiden Seiten der Verwerfung beobachtet wurden. Dieser Typ FZHW wurde hier erstmals beobachtet weist auf ein sich entwickelndes Pull-Apart-Sedimentbecken in Form einer oberflächennahen lokalen Niedriggeschwindigkeitszone hin, die sich bis in eine Tiefe von 4-5 km erstreckt. Die genannten Phasen tragen zur Komplexität von P-Wellenformen bei, die nahe einer Verwerfung aufgezeichnet werden, und enthalten wertvolle Informationen über die Struktur aktiver Verwerfungszonen. Der relativ niedrige Geschwindigkeitskontrast am Karadere-Segment im Vergleich zum Geschwindigkeitskontrast westlich des Karadere-Segments könnte die Bruchausbreitung vom Izmit-Beben gestoppt haben und beinhaltet somit wichtige Informationen zur Diskussion, was Erdbeben stoppen lässt.

In der zweiten Studie wurden Wellenformen lokaler Seismizität aus dem Zeitraum vor, zwischen und nach den zwei aufeinanderfolgenden von 1999 $M_w > 7$ İzmit- und Düzce-Erdbeben analysiert. Die Wellenformen wurden an drei seismischen Stationen entlang des Mudurnu-Segments der NAFZ aufgezeichnet. Es wurden zwei konsistente Sekundärphasen identifiziert und analysiert, die in ausreichend zeitlichem Abstand von der direkten P-Welle in der P-Wellen-Coda enthalten sind, um sie im Detail studieren zu können. Diese Phasen wurden durch eine Struktur in der Nähe der Stationen erzeugt. Diese Schlussfolgerung ergibt sich, weil die Phasen bei allen Wellenformen sichtbar sind und unabhängig von der Epizentralentfernung, Hypozentraltiefe und Backazimuth einen konstanten Laufzeitunterschied zur direkten P-Welle haben. Ergebnisse der Polarisationsanalyse weisen darauf hin, dass die prominentere Sekundärphase eine PS-konvertierte Welle (PS-Phase) ist. Die Richtung ihrer Polarisation stimmt mit der der direkten S-Welle überein und zeigt Shear-Wave-Splitting, welches durch die anisotrope obere Kruste erzeugt wird. Die Polarisationsrichtung der anderen Sekundärphase ist nahezu vertikal und konsistent mit der Polarisationsrichtung der P-Welle. Synthetische Modellierungen zeigen, dass die PS-Phase an einer horizontalen Grenzfläche in einer Tiefe von ~ 4 km konvertiert wird. Die Studie geht außerdem der Frage nach, ob die PS-reflektierten Wellen in flachen Tiefen an der steilen Mudurnu-Verwerfung entstehen. Diese Interpretation ist in Übereinstimmung mit den oberflächennahen Strukturen einer Pull-Apart-Struktur im Anfangsstadium entlang des Mudurnu-Verwerfungssegmentes und weist auf das sich nach Osten ausbreitende transtensionale tektonische System hin, welches für diese Region bekannt ist.

Die Ergebnisse der beiden Studien zeigen das Potenzial der detaillierten Analyse von Phasen wie FZHW, reflektierten und konvertierten Wellenzügen in Seismogrammen lokaler Seismizität für die Untersuchungen von seismisch aktiven Störungen. Insbesondere wurde durch die hier angewandten Techniken gezeigt, dass die Beschaffenheit der Karadere-Verwerfung und die nahezu vertikale Mudurnu-Verwerfung im Nordwesten der Türkei rein passiv abgebildet und ihre aktuelle tektonische Entwicklung daraus abgeleitet werden können. Die Ergebnisse implizieren, dass diese Studien dazu dienen können, potenzielle gefährdungsrelevante Segmente der NAFZ zu ermitteln und somit zukünftige Rupturzonen und das damit verbundene seismische Gefährdungspotenzial im Vorfeld von Starkbeben besser zu charakterisieren.

Contents

Summary	IV
Zusammenfassung.....	VI
Contents	IX
1. General Introduction	1
1.1 Motivation and Outline	3
2. Theory	7
2.1. Imaging bimaterial interfaces using Fault Zone Head Waves.	7
2.1.1. Bimaterial Interfaces	7
2.1.2. Fault Zone Head Waves	7
2.1.3. Directivity Effect of bimaterial interfaces and damage asymmetry across an interface	11
2.1.4. Previous Investigations	13
2.2. Imaging Crustal discontinuities Using Reflected and Converted Phases	15
2.2.1. Snell's law and travel-time curves	16
2.2.2. Reflection and Refraction and conversion of waves	17
2.2.3. Conversions to other types in seismic phases from local and regional events.....	19
2.2.4. Synthetic seismograms.....	21
2.2.5. Imaging crustal discontinuities with local earthquake data	22
3. Tectonic setting of areas of study.....	25
4. Bimaterial interfaces at the Karadere segment of the North Anatolian Fault, northwestern Turkey	29
4.1. Introduction	30
4.2. Data	31
4.3. Data Analysis and results	33
4.4. Discussion and Conclusions.....	49
5. Imaging Mudurnu Segment of the North Anatolian Fault Zone from Waveforms of Small Earthquakes	55
5.1. Introduction	56
5.2. Data	58
5.3. Data Analysis.....	58

5.3.1. Waveform Processing	58
5.3.2. Epicentral and Depth Sorting Complemented by Azimuthal Analysis.....	62
5.3.3. Detected Secondary Phases.....	64
5.3.4. Particle Motion Analysis.....	65
5.4. Synthetics and Interpretation.....	67
5.5. Discussion and Conclusions.....	70
6. Further Remarks on FZHW analysis.....	75
7. Conclusion and Perspectives.....	81
7.1. Perspectives	84
References.....	87
List of Figures	98
Curriculum Vitae	100
Acknowledgements.....	101

1. General Introduction

Fault zones are complex structures that provide information on several characteristics of earthquakes such as source properties, evolutionary processes on long (tectonic) and short (e.g., precursory) time scales. Observing and monitoring fault rock damages can provide information on brittle rock rheology. Fault zones can control crustal fluid flow such as subsurface storage, hydrology and oil. In general, fault zones have high apparent geometrical complexity including hierarchy of damage zones and slip localization surfaces that can spread to branching structures. This apparent complexity typically diminishes at depth [Rockwell and Ben-Zion, 2007].

Large fault zones may have high crack density which can lead to prominent scattering [e.g. Benites *et al.*, 1992; Nishigami, 2000; Revenaugh, 2000], higher attenuation [e.g. Jongmans and Malin, 1995; Korneev *et al.*, 2003] and lower seismic velocities [e.g. Thurber *et al.*, 2006; Li *et al.*, 2007]. Furthermore, having a preferred crack orientation can lead to higher anisotropy of seismic velocities and higher attenuation [e.g. Cochran *et al.*, 2003; Peng and Ben-Zion, 2004; Liu *et al.*, 2005; Boness and Zoback, 2006]. All the mentioned features [Lewis and Ben-Zion, 2010] indicate the importance of nature of damage zones around faults. Elements of fault zone structures such as damage zones and bimaterial interfaces (separating different crustal blocks) control future (and reflect past) earthquake rupture properties [e.g. Ben-Zion and Sammis, 2003; Rowe and Griffith, 2015].

Bimaterial interfaces have important implications on rupture properties of earthquakes. Rupture on a bimaterial interface produce changes of normal stress that are proportional to the spatial derivative of in-plane slip (Figure 1.1). In the simpler homogeneous framework these two quantities are not coupled [e.g., Aki and Richards, 2002]. The interaction between slip and normal stress along a bimaterial interface can reduce dynamically the frictional strength – potentially to zero – making material interfaces mechanically favored surfaces for rupture propagation [Ben-Zion, 2001; Brietzke and Ben-Zion, 2006]. Furthermore, asymmetric damage pattern across a seismogenic fault may indicate repeating occurrence of large earthquake ruptures with statistically preferred propagation direction [e.g., Ben-Zion and Shi, 2005; Dor *et al.*, 2006; 2008; Lewis *et al.*, 2005]. Other possible consequences of existence of a bimaterial interface are generation of very high slip velocities behind the propagating rupture front [e.g., Ben-Zion, 2001; Ampuero and Ben-Zion, 2008], asymmetric

distributions of aftershocks on the fault [e.g., *Rubin and Gillard, 2000; Zaliapin and Ben-Zion, 2011*], and asymmetric geodetic fields across the fault [e.g., *Le Pichon et al., 2005; Wdowinski et al., 2007*]. Therefore, it is important to understand the velocity structures along and across fault zones to the highest possible extent [*Allam et al., 2014; Qiu et al., 2017*].

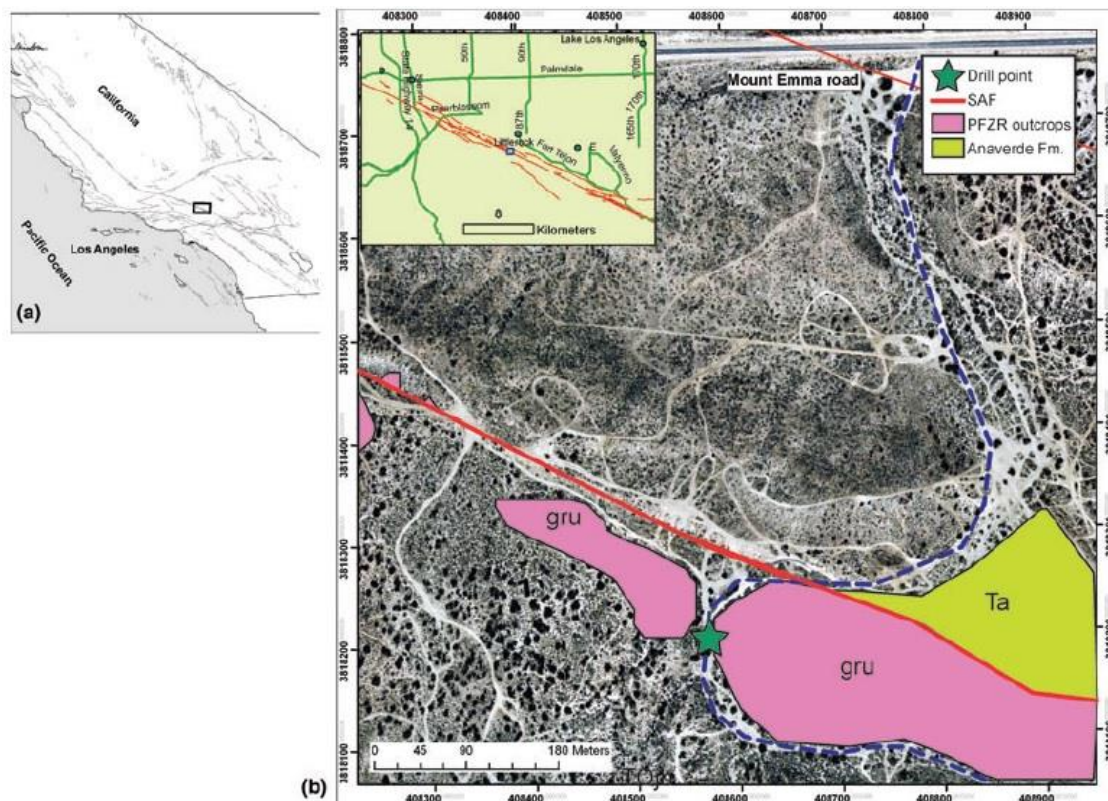


Figure 1.1. An example of bimaterial interface. (a) General location and major faults in southern California. The Littlerock area of San Andreas Fault shown in b) is enclosed in the box. (b) An air-photo of the location of a drill site (star). “gru” represents Mesozoic granitoids and “Ta” represents Neogene Anaverde Fm. PFZR stands for ‘pulverized fault zone rocks’. Pulverization is thought to be associated with dynamic reduction of normal stress during earthquake ruptures, which is expected to be enhanced for ruptures on a bimaterial interface. Figure and caption after *Wechsler et al. [2011]*.

Imaging fault zones in detail is very challenging task due to possible non-linear wave propagation effects and temporal changes of seismic properties [*Wu et al., 2009*], strong geometrical and material heterogeneities and strong attenuation effect of fault zones [*Lewis and Ben-Zion, 2010*]. The imaging of fault zones is done best by using several signals and techniques. The possible signals are body waves, head waves, trapped waves, scattered waves, anisotropy, surface waves. Some of the possible techniques are travel time and waveform tomography as well as noise correlations. Each signal and technique has its own advantages and can carry information on certain fault zone features. Between all the

mentioned signals that can be used to study fault zones, Fault Zone Head Wave (FZHW) is the best tool to study the existence and characteristics of the bimaterial interface of a fault zone.

Meanwhile, in other research branches, a large contribution in imaging crustal structures has been done by investigating waveforms of active (active seismics) or passive sources (earthquakes), reaching the stations with possible reflected and converted phases. Investigating the structure beneath a seismic station using data from passive sources can be performed using several methods such as exploiting stacked correlograms of three-component records from teleseismic events [*Sun and Kennett, 2016*] and by using the converted phases between the P and S arrivals from local earthquakes [*Latorre et al., 2004*].

Furthermore, microseismic data from local earthquakes represent seismic waves generated by weak local earthquakes and can be used to image crustal discontinuities. According to *Hrubcová et al. [2016]*, the number of microearthquakes is normally quite large and their hypocenters are clustered in space and time. The waveforms are of high frequency and very responsive to local crustal heterogeneities. The waveforms typically display distinct direct P and S waves followed by coda waves. The reflected PPP and converted SP and PS waves, which are secondarily generated at subsurface layers represent the most pronounced coda phases. These phases can serve for detecting discontinuities within the crust and for determining their depth. If the microseismicity is monitored by a dense network of sensitive seismic stations with a good azimuthal distribution, it is possible to retrieve a detailed crustal structure and to map lateral variations and topography of crustal discontinuities [*Hrubcová et al., 2016*].

1.1 Motivation and Outline

Imaging and characterizing faults that are believed to produce large earthquakes in the near future are crucial for the resulting seismic hazard, risk assessment and subsequent preparedness of nearby population centers. However, this is a challenging task and not a standard procedure is available. In fact, this needs high-resolution waveform recordings and sophisticated processing procedure.

Having knowledge about the fault-zone structure at depth and quantifying bimaterial interfaces across faults can have several important implications for earthquake behavior. As

previously mentioned, some of the consequences of the existence of bimaterial interfaces include changing dynamically the strength of the fault, suppressing branching of ruptures, reducing the generation of frictional heat, and finally and most importantly producing a statistical preference for the propagation direction of earthquakes [e.g., *Ben-Zion*, 2001], which can have strong influence on seismic shaking hazard, since rupture directivity can amplify the ground motion in the propagation direction by a factor 3 or more [*Bulut et al.*, 2012a]. Previous studies [e.g., *Ben-Zion and Malin*, 1991] have shown the importance of considering the existence of a bimaterial interface, since it can help to avoid errors in inferred velocity structures and earthquake source properties [*Bulut et al.*, 2012a]. When FZHW are present they are likely to be misidentified in manual picking of phases or by the STA/LTA and kurtosis pickers as direct P arrivals. This problem was noted by the early observational papers on FZHW [*Ben-Zion and Malin*, 1991] and was demonstrated clearly by *Allam et al.* [2014]; the P-wave picks of the Northern California Earthquake Data Center at near-fault stations on the slow side of the Hayward fault were commonly FZHW rather than direct P waves [*Ross and Ben-Zion*, 2014].

The best diagnostic signal to detect and study velocity contrast across a fault is provided by FZHWs that propagate along the interface and are radiated from there to the slow side of the fault [*Ben-Zion*, 1989; 1990]. Previous studies performed in sections such as the San Andreas Fault (SAF) in central California [e.g. *Zhao et al.*, 2010] showed existence of velocity contrast across the fault, that could be detected precisely using FZHW. The simplicity of the method with the possibility to extract information on velocity structures at depth across the fault with only a few stations was a reason to further investigate the North Anatolian Fault Zone (NAFZ) using FZHW. This is of high importance in faults such as the NAFZ, with many large earthquakes (including $M > 7$) in history.

Furthermore, *Hrubcová et al.* [2016] investigated the crustal discontinuities using local microseismic waves with a new approach that will be described in section 2.2.5. Due to the limitations in imaging vertical structures in earth using active seismics and high cost of the investigations in using boreholes, developing other methods in order to image rather vertical structures such as strike slip faults is of high importance.

To address these topics, FZHW analysis for imaging bimaterial interfaces and modification of the method of *Hrubcová et al.* [2016] in order to image near vertical

structures are performed in different segments of the NAFZ. First, to study the possible existence of bimaterial interfaces in the structure associated with the Karadere fault, waveform data recorded by the local seismic PASSCAL network that was deployed within one week after the Izmit earthquake along and around the Karadere-Düzce sections of the NAFZ is used. The study has been published in *the Journal of Geophysical Research, Solid Earth* (Chapter 4). Second, the technique of *Hrubcová et al.* [2013 ; 2016] is extended to near-fault zone recordings along the North Anatolian Fault Zone (NAFZ) in northwestern Turkey and aims to image the structure around the strike-slip Mudurnu segment as a major NAFZ branch. In this study, data from the seismic network SABONET with stations near the Mudurnu segment of the NAFZ is used. A manuscript of this study is recently submitted to the *Journal of Geophysical Research, Solid Earth* (Chapter 5).

The research performed and explained in chapter 4 and 5 brings new insights into systematic imaging of fault zones and provides knowledge on the structure of the NAFZ at the investigated segments. The outline of the material presented in this thesis is as follows:

Chapter 2 includes the theory and background of the investigations. First, the theory of FZHW, some of the important features of bimaterial interfaces and previous investigations using FZHW signals are described in detail in section 2.1 of this chapter. Second, the basics of ray theory as well as converted and reflected phases, synthetics used in the method of *Hrubcová et al.* [2016] and related previous investigations are described in section 2.2.

Chapter 3 provides information on the tectonic setting of the NAFZ and the main segments of the NAFZ that are analyzed later in chapters 4, 5 and 6. This information is provided in the published paper [*Najdahmadi et al.*, 2016] and the submitted manuscript [*Najdahmadi*, 2017, in review], therefore it is not included in chapters 4 and 5 of this thesis, but combined together and described in chapter 3.

Chapter 4 focuses on the investigation of bimaterial interfaces across and along the Karadere segment of the NAFZ using FZHW.

Chapter 5 presents modification of the method of *Hrubcová et al.* [2016] in order to image near vertical structures of the Mudurnu segment of the NAFZ.

Chapter 6 covers some of the important issues that need to be considered carefully in FZHW analysis following a preliminary attempt to detect bimaterial interfaces in another

section of the NAFZ further to the east using a fully manual approach. The essential points in the evaluation of apparent FZHW are specified as well.

Chapter 7 summarizes the studies performed within this thesis and notes the achievements followed by perspectives and future work suggestions.

2. Theory

2.1. Imaging bimaterial interfaces using Fault Zone Head Waves.

2.1.1. Bimaterial Interfaces

The juxtaposition of different lithologies in contact across a fault can be expressed as a sharp contrast in velocity, termed a bimaterial interface. The sites of most earthquakes are along geological faults which are surfaces of material discontinuity with different rock bodies in the earth. In contrary to other common theoretical models of seismic ruptures, which usually simplified the source region by assuming that slip took place along a surface that was situated in a homogeneous region, *Ben-Zion*, [1989] studied some consequences of allowing material discontinuity to exist in the source region. It was shown that the resulting fields differed from that of a homogeneous half space in the distribution of travel times, wave amplitudes and polarity of first motions. In other words comparison of near-fault synthetic seismograms in faster and slower joined quarter-spaces was performed; Due to the difference observed, the importance of using response functions that includes material heterogeneity in the source region when constructing synthetics was demonstrated [*Ben-Zion*, 1989].

2.1.2. Fault Zone Head Waves

The best diagnostic signal to detect and study a bimaterial fault interface is provided by fault zone head waves (FZHW) that refract along the interface and are radiated from there to the slow side of the fault [*Ben-Zion*, 1989; 1990].

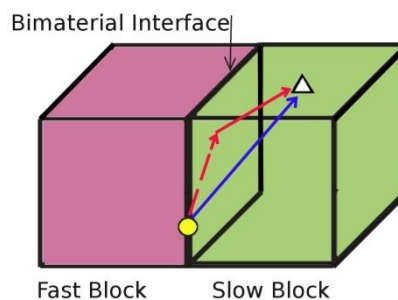


Figure 2.1. A schematic sketch for a bimaterial interface. Red dashed arrow represents FZHW while propagating along the bimaterial interface with the speed of the fast block. Next the FZHW is radiated to the slow side of the fault (red arrow) and reaches the station (white triangle). The blue arrow represents direct P wave, which propagates from earthquake (yellow circle) with the speed of the slow block (green) to the station (figure plotted after *Ben-Zion*, [2013])

In a simple structure consisting of two solids in contact, FZHW are the first arrivals at stations on the side with slower seismic velocity that are within a critical distance x_c from the interface given by [Ben-Zion, 1989]

$$x_c = r \cdot \tan(\cos^{-1}(\alpha_s / \alpha_f)), \quad (2.1)$$

where r is the distance the FZHW travel along the fault and α_f, α_s are the average P-wave velocities of the faster and slower media, respectively. Several characteristics can be used to identify FZHW in general: they are short emergent pulses truncated by the closely following sharper direct P wave, have opposite first-motion polarity than the more impulsive following direct waves, and have arrival time moveout (Δt) from the direct wave that increases with distance traveled along the fault (r) as

$$\Delta t \sim r \Delta\alpha / \alpha^2, \quad (2.2)$$

with α and $\Delta\alpha$ denoting the average and differential P waves velocities, respectively [Ben-Zion and Malin, 1991]. In addition, since FZHW are radiated from the fault they should have particle motion with significant fault-normal component, in contrast to the particle motion of the direct P waves that points to the epicenter direction [Bulut et al., 2012a; Allam et al., 2014].

Since fault zone head waves are restricted to the vicinity of bimaterial interface, they can reveal detailed information on earthquake processes and fault zone structures. If their existence is ignored, they can be mistakenly attributed to various sources and medium effects. For example a headwave traveling with high speed can continue its propagation in the faster medium as an S wave and arrive shortly after direct P arrival, which can lead to assumptions of a complex source behavior such as a multiple-slip event [Ben-Zion and Malin, 1991].

As mentioned, in case the distance of station and earthquake is less than x_c of Eq. 2.1, FZHW arrive sooner than body P waves to the station. FZHW and direct P phase have several differences (such as FZHW being an emergent phase) that can be used to distinguish between them. According to Bulut et al. [2012a] one can use the polarization changes from the horizontal components of waveforms as a tool to distinguish between FZHW and direct P as well. After propagation along the interface with the speed of the fast block, FZHW are radiated from the bimaterial interface to the slow block and reach the station. Direct P waves propagate in the back-azimuth direction (slow block) as shown in Figure 2.1. This can lead to difference in polarizations of FZHW and direct P as they reach the station to distinguish

between them and measure their arrival times. Therefore the polarization is first expected to show random motion due to noise and later changes to the fault normal direction as FZHW reaches the station, and finally turns to event-station back-azimuth, as direct P phase arrives to the station [Bulut et al., 2012a; Allam et al., 2014].

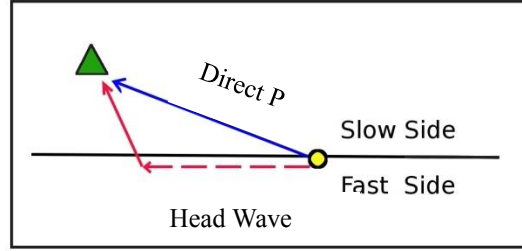


Figure 2.2. Schematic diagram showing a bimaterial interface between a fast and a slow block and the resulting different polarization of the direct P wave compared to the first-arriving FZHW. The FZHW has polarization more normal to the fault, while the direct P has polarization directly along the source receiver back-azimuth (plotted after Allam et al. [2014]).

The polarization direction can be computed using the *Jurkevics*, [1988] algorithm by solving the eigenproblem for a covariance matrix S [Bulut et al., 2012a; Allam et al., 2014] as follows:

$$S = \frac{XX^T}{N} = \begin{bmatrix} S_{zz} & S_{zn} & S_{ze} \\ S_{zn} & S_{nn} & S_{ne} \\ S_{ze} & S_{ne} & S_{ee} \end{bmatrix} \quad (2.3)$$

where the three components (Z, N, E) of motion are combined in a single time window of length N (samples) into an $N \times 3$ matrix X . The principal axes of the polarization ellipsoid are found by solving the eigenproblem for the covariance matrix S . The eigenvalues of S ($\lambda_1, \lambda_2, \lambda_3$) correspond to the amplitudes of the axes of the polarization ellipse and eigenvectors of S (u_1, u_2, u_3) give the directions of it [Bulut et al., 2012a; Allam et al., 2014]. The polarization of P waves (Az) is assumed to be the horizontal orientation of rectilinear motion, given by the eigenvector u_1 , corresponding to the largest eigenvalue λ_1 :

$$Az = \tan^{-1}\left(\frac{u_{21}}{u_{31}}\right) \quad (2.4)$$

The Az for a direct P wave should be along the source-receiver back-azimuth and for a FZHW it should be oriented towards the fault interface. Using consecutive time windows

to look for arrival of each phase, λ_1 of a head wave is larger than λ_1 of the noise before it, and the next incoming direct P wave has larger λ_1 than the λ_1 value corresponding to the previous headwave. The arrivals of the head and direct P waves can be checked further and picked more precisely by identifying the exact time of transitions of particle motion from approximately random towards the fault-normal and from there towards the back-azimuth direction [Allam et al., 2014].

So far, general characteristics of FZHW in comparison to direct P and quantified polarization analysis as an additional tool to distinguish between the two phases are described. However, performing only manual analysis on the vertical components to find possible existing FZHW and using polarization analysis to confirm their existence or arrival times is time consuming and can lead to false detections of FZHW as will be described in chapter 6. False detections can also happen in the case one picks the very first arrival on the seismogram recorded by a station located on the slow side as direct P instead of FZHW [Allam et al., 2014], which can be the case when an automatic picker algorithm or the person who manually picks the phases, is not aware of possibility of existence of FZHWs. As an example, Allam et al. [2014] showed how for stations located on the slow side and close to the fault, the former manually picked direct P phases of the Northern California Earthquake Data Center were mostly FZHW and not direct P waves.

In order to analyze larger amount of data systematically, faster and avoid false detections an algorithm for automatic picking of FZHW and direct P was developed by Ross and Ben-Zion, [2014]. The algorithm's first stage is making a pick on the vertical component for the earliest onset of the seismic motion over the noise. In case of existence of a head wave, this pick stays on the onset of the head wave. Otherwise the direct P arrival will be picked. The latter picking step is performed using an STA/LTA detector. Later two additional pickers are used simultaneously to find the sharpest arrival in order to specifically pick a direct P-wave arrival. The picker uses the kurtosis function and a moving skewness function [Saragiotis et al., 2002]. The derivatives of both functions are very sensitive to the abrupt changes of the waveforms, which is a characteristic of direct P wave arrivals. The skewness measures statistical asymmetry and in particular indicates whether the sample is left-skewed or right-skewed. In addition, to avoid picking onsets that are not FZHW but are associated with other effects, such as free-surface reflections at borehole instruments or arrivals from different earthquakes, another characteristic of FZHW, which is having opposite first motion polarity from the direct P wave is an option included in the algorithm. This is performed by

the skewness function without being too sensitive to small fluctuations. Next the time difference between each tentative pick of the direct P-wave and the first motion pick is calculated and compared to basic theoretical expectations for FZHW. For more information see *Ross and Ben-Zion*, [2014].

The algorithm mentioned above using vertical components of seismograms, combined with the polarization analysis (including the two horizontal components) has been used to detect and pick FZHW and direct P phases in recording from the Karadere segment of the NAFZ as described in chapter 4.

2.1.3. Directivity Effect of bimaterial interfaces and damage asymmetry across an interface

Here, a few details on a model of dynamic rupture along an interface separating different elastic solids [*Andrews and Ben-Zion*, 1997; *Ben-Zion*, 2001] and its implications on damage asymmetry across the NAFZ with regard to velocity contrast across the fault is described.

Andrews and Ben-Zion, [1997] and *Ben-Zion*, [2001] modeled particle velocities at a given time for rupture along a fault (denoted by y in Figure 2.3, equivalent to $y=0$) separating two different elastic solids. The fault is marked by the thin horizontal line separating two different elastic solids (faster below the interface and slower above the interface). Due to the material contrast, the radiation on the different sides of the fault is asymmetric. On the faster block the faster P and S body wave fronts propagate, however as describe before on the slower block, in addition to the slower P and S body wave head wave fronts propagate. Due to the larger displacement occurring on the more compliant side, the rupture leads to different amplitudes of particle velocity in different directions (propagation direction and the opposite. The higher displacement of the material ahead of the rupture on the slower block produces dilation. The frictional strength reduces dynamically as a result of the dilation ahead of the rupture. As a result, slip can occur ahead of the rupture [*Andrews and Ben-Zion*, 1997; *Ben-Zion*, 2001]. On the other hand, at short distance behind the rupture front, the particle velocities lead to compression in the system, which clamps the fault. As a result, the motion is strongly asymmetric across the fault and a narrow wrinkle-like pulse is generated that propagates in the direction of slip in the slower block [*Ben-Zion*, 2001].

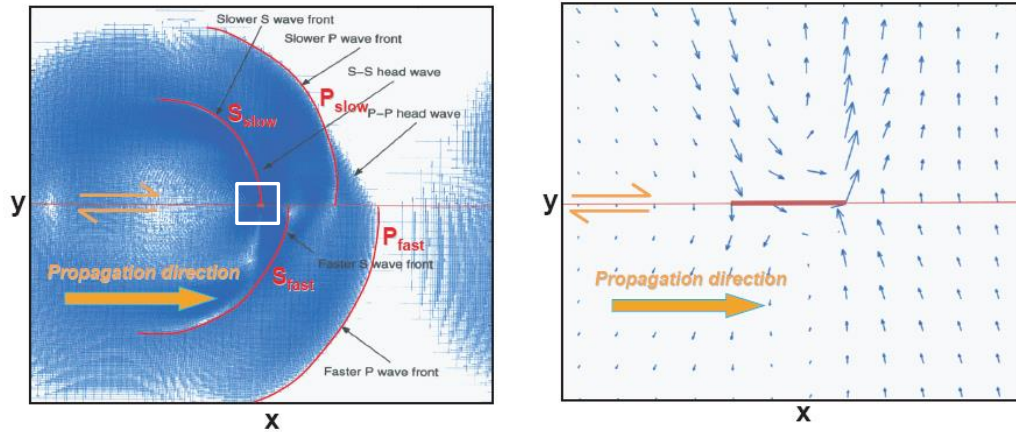


Figure 2.3. (a) Particle velocities at a given time generated by a wrinkle-like rupture pulse (small red bar within the white box) propagating to the right along a right-lateral strike-slip fault (thin red horizontal line), which is between different elastic solids. The slower velocity block (with 20 per cent lower shear wave velocity) is above the fault as seen by the fronts of the radiated seismic waves. (b) Enlarged view of the part enclosed in the white box in a) showing asymmetric particle velocities around the rupture pulse. The asymmetric dynamic stress fields in different directions produce a statistical tendency of ruptures to propagate further to the right and include more potential sites of immediate aftershocks in that direction. From Zaliapin and Ben-Zion, [2011] after Ben-Zion [2001].

In the case of North Anatolian Fault, a sequence of large magnitude earthquakes (larger than M7) began with the 1939 (M7.9) earthquake near Erzincan at east, and proceeded westward. The sequence of earthquakes was referred to successive failures of fault segments due to stress transfer from failed neighboring segments according to Stein *et al.* [1997]. There were two main exceptions in the sequence of earthquakes: The 1943 earthquake, which did not nucleate in the region of stress increase and the August 1999 Izmit earthquake that ruptured eastward and was followed by the November 1999 Düzce earthquake with the continuation of eastward rupture. The general westward propagation of earthquakes is a result of the southern block of North Anatolian Block, being the slower block [e.g., Sengör *et al.*, 2005]. For the cases of 1943 and 1999 earthquake a reversal in local velocity with the southern block being the faster block might have caused the eastward propagation of earthquakes [Dor *et al.*, 2006].

Regarding possible damage asymmetry caused by velocity contrast across the fault, according to Dor *et al.* [2008], NAF is expected to have more rock damage on the faster block at depth due to cumulative effect of many ruptures on a lithology contrast between the opposite sides of the fault if the NAF makes a moderate to high angle with the maximum principle stress and if ruptures propagate with subshear velocities [Ben-Zion and Shi, 2005]. The moderate or high angle between the maximum principle stress and the fault has been the case for the SAF [e.g. Hickman, 1991] and subshear velocities for rupture propagation has been the case for most earthquakes (e.g. Mai, 2004). If both conditions are met, faster seismic

velocities at depth are expected on the sides with higher rock damage, which would be the southern side of 1943 section and the southern side of 1999 Izmit rupture. In case the first condition is not met or if the angle between the maximum compressive stress and the fault is shallower than 15° [Templeton and Rice, 2008], the damage is expected to be more symmetric. If the second condition is not met (i.e. rupture propagations with super shear velocities), according to Weertman, [2002] the damage asymmetry mentioned can be reversed [Dor et al., 2008].

2.1.4. Previous Investigations

FZHW analysis has been mainly performed in several sections of the San Andreas Fault system in California. A summary of the previous research performed on bimaterial interfaces and FZHW analysis is as follows:

Ben-Zion and Malin, [1991] found that the apparent direct P arrivals on the microearthquake seismograms recorded by a borehole seismic network on the SAF near Parkfield were indeed FZHWs. They estimated the velocity contrast across the SAF near Parkfield to be approximately 4 percent and emphasized the importance of further studies on FZHW.

McGuire and Ben-Zion, [2005] used data from a dense temporary array in the region of the SAF and showed the sensitivity of FZHW to the structure of the fault zone in the seismogenic zone, including an estimation of velocity contrast across the fault in that segment. *Lewis et al.* [2007] used the arrival time data of direct P and FZHW in the SAF south of Hollister, to perform a joint inversion in order to obtain a high-resolution local velocity structure. According to their findings, the velocity contrast across the fault is higher at shallower depths (about 50 per cent) and decreases with depth, so that below 3 km, a velocity contrast of 10-20 per cent, with the faster southwest side exists.

Directivity effects of bimaterial interface as described in the previous section (2.1.3) and asymmetric damage zones associated with bimaterial interfaces are studied in detail for fault segments of the SAF [e.g. *Dor et al.*, 2006; ; *Wechsler et al.*, 2011] and NAFZ [*Dor et al.*, 2008].

Zhao et al. [2010] investigated the seismic velocity contrast across the SAF in the Parkfield area using FZHW. On the NE side of the fault where the SAF is creeping north of Middle Mountain (MM), FZHW were observed (Figure 2.4). The velocity contrast north of

MM was about 5–10 per cent, and further to the south, near Gold Hill (GH) it decreased to 0–2 per cent.

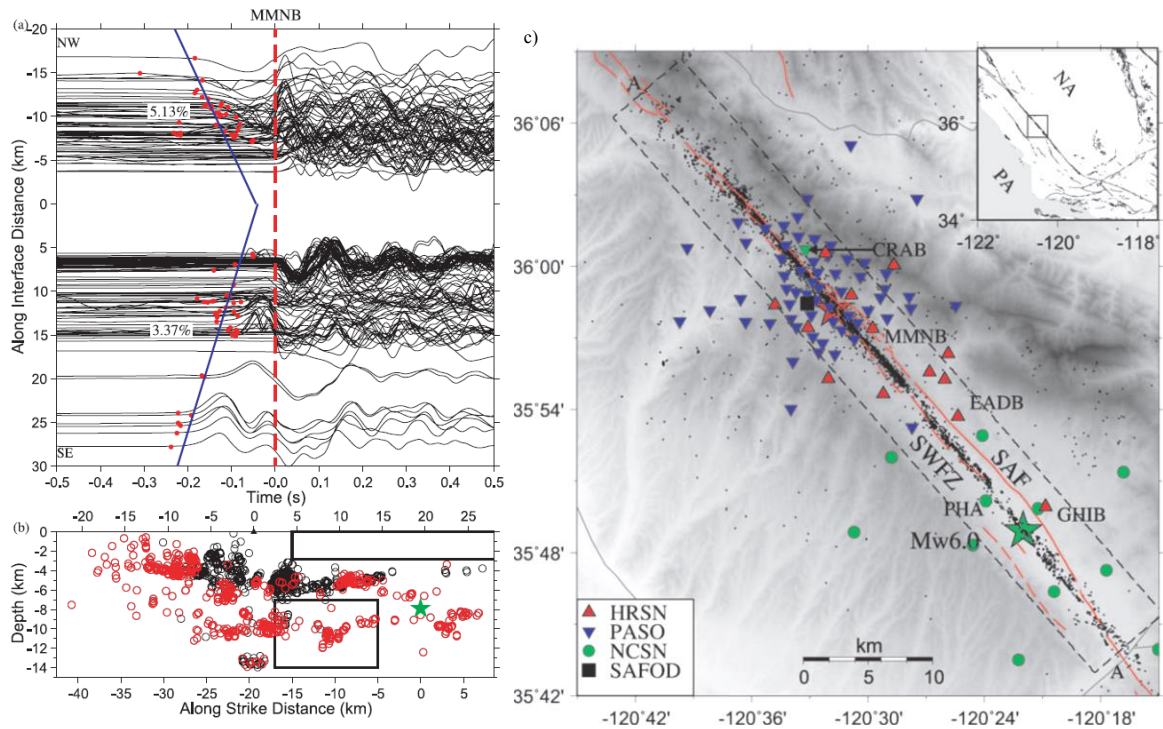


Figure 2.4. An example of previous investigations performed in the Parkfield area of the SAF. (a) Vertical displacement seismograms recorded by station MMNB aligned on the direct P arrivals (red vertical dashed lines). The red dots mark the onset of FZHW and the blue line shows the least-squares fitting of the moveout. The obtained velocity contrasts are 5.13% at NW and 3.37% at SE. (b) A cross-section view of the seismicity with corresponding waveforms shown in a). Events with FZHW are marked by red circles. The values on the horizontal axis at the top show distance of events from the station and the values on the bottom of the panel show distance of events from the 2004 Parkfield earthquake (green star) projected along the SAF strike. (c) Map of the Parkfield section of the SAF. The background seismicity from 1984 and 2005 (small dots) and the 2004 M6 Parkfield earthquake (green star) are marked on the map. The red lines denote surface traces of faults. Seismic station MMNB is marked with a red triangle [Zhao *et al.*, 2010].

The velocity contrast found at this section of the SAF fits to the geological setting and explains the propagation directions of the (M6) Parkfield earthquakes. Since at north, a strong velocity contrast around MM exists, if an earthquake happens near it, the expected preferred propagation direction is to the south east (e.g. the 1934 and 1966 Parkfield earthquakes). Since further to the south, near GH the velocity contrast decreases - and multiple fault branches exist- earthquakes that nucleate near GH (e.g. the 2004 Parkfield earthquake) are not expected to have a preferred propagation direction to the south east and rather other factors such as structural and stress heterogeneities control the preferred propagation direction [Zhao *et al.*, 2010].

The first FZHW analysis in the NAFZ was performed by Bulut *et al.* [2012a] across the Mudurnu segment with polarization analysis of early P waveforms. The analysis used

changes in particle motion of near fault seismicity from fault–normal to source–receiver directions to distinguish between the FZHW and direct P arrivals. A velocity contrast of at least 6% was found across Mudurnu segment of the NAFZ with the southern block having faster P wave velocities [Bulut *et al.*, 2012a]. In chapter 5 of this thesis, the structure of Mudurnu fault further to the east is studied.

Meanwhile, *Allam et al.* [2014] studied Hayward fault in the San Francisco Bay area and following the method of *Bulut et al.* [2012a], calculated the polarizations of the recorded horizontal displacement seismograms with the algorithm of *Jurkevics*, [1988] as described previously in section 2.1.2. The results indicated average velocity contrasts of 3–8 %, with the southwest side being the faster side, which was in agreement with tomographic images.

The mentioned studies were followed by an automatic picker of P, S seismic phases and FZHWs developed by *Ross and Ben-Zion*, [2014] described with more details in section 2.1.2, which is used in the FZHW analysis performed in this thesis (chapter 4). Finally, the other recent studies that also implemented FZHW analysis are performed by *H Yang*, [2015], *Share and Ben-Zion*, [2016], *Qiu et al.*, [2017] and *Share et al.* [In review, 2017].

2.2. Imaging Crustal discontinuities Using Reflected and Converted Phases

Seismic waves propagating through the Earth are subject to reflections, refractions and conversion of phases as they reach interfaces that separate materials with different properties. Several factors can affect the behavior of waves (e.g. amount of energy of the seismic wave reflected or refracted, angle of the reflected or refracted phase from the interface) as they interact with an interface. Some of these factors and the methods of analysis of waveform changes are briefly described here.

The relationship between stress and strain in an elastic isotropic medium is governed by the generalized Hook’s law, where the independent parameters in the elastic tensor reduce to two Lamé parameters (for more information see page 50 & 51, *Stein and Wysession*, [2003]). These elastic parameters can affect the velocity with which a seismic wave propagates. Comparing the Newton’s acceleration with the divergence of the stress tensor and the body force, *the equation of motion for a continuum* as follows:

$$\rho \frac{\partial^2 u_i}{\partial t^2} = \partial_j \tau_{ij} + f_i \quad (2.5)$$

where ρ is the density of the medium, u_i is the displacement, τ_{ij} is the stress tensor and f_i is the body force that in general refers to gravity and source terms [Bormann, 2012]. An

important form of the equation of motion is when there is no body force applied ($f_i = 0$). This form is called the homogenous equation of motion. This equation describes seismic wave propagation except as a source, such as an earthquake or an explosion, when a body force generates seismic waves [Stein and Wysession, 2003]. The solutions of equation of motion, give the ground motion at distance away from source, the synthetic seismograms [Bormann, 2012], which will be described in section 2.2.4 of this chapter.

Using the relationship between stress and strain, Eq. 2.5 will have a complicated form involving gradients in the Lamé parameters for an inhomogeneous medium. Therefore, according to Bormann, [2012] some methods for synthetic seismogram model the material as a series of homogeneous layers with no gradients in the Lamé parameters. The solutions for waves at two sides of an interface are linked by reflection and transmission coefficients governed by Snell's law [e.g. Fuchs and Müller, 1971; Bouchon, 1981; Kennett, 1983]. A different approach is by assuming that variations in the Lamé parameters are negligible over a wavelength and thus these terms tend to zero at high frequencies as in methods of Červený and Pšenčík, [1977] or Chapman, [2002] [Bormann, 2012]. The methods of Bouchon, [1981] and Červený, [2001] will be described more in section 2.2.4 of this chapter and are used in chapter 5 of this thesis to calculate the synthetics seismograms.

2.2.1. Snell's law and travel-time curves

According to Snell's law, having an interface between two homogenous mediums with different velocities V_1 and V_2 (Fig. 2.5) and an incoming wave reaching the interface with an angle of i_1 , which is measured from the normal of the boundary the result can be a refracted wave with an angle i_2 is as follows:

$$\frac{\sin i_1}{V_1} = \frac{\sin i_2}{V_2} \equiv p = \text{constant} \quad (2.6)$$

where p is slowness of the medium or ray parameter.

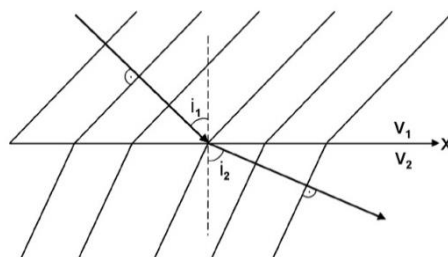


Figure 2.5. A plane wave reaching an interface between two homogeneous layers. Due to the higher velocity in the bottom layer, the wavefront is scattered further apart [Bormann, 2012].

Compressional and shear seismic velocities increases with depth in the Earth in general. Considering layers above each other, a downward wave is transmitted with higher angle (from the normal) till the turning point (tp), after which it propagates upward to the station. This propagation pattern and the corresponding arrival times (travel time curves) can be modeled for various velocities and the corresponding travel time can be modeled. Fig 2.6 shows an example for the case of continuous velocity increase with depth [Bormann, 2012].

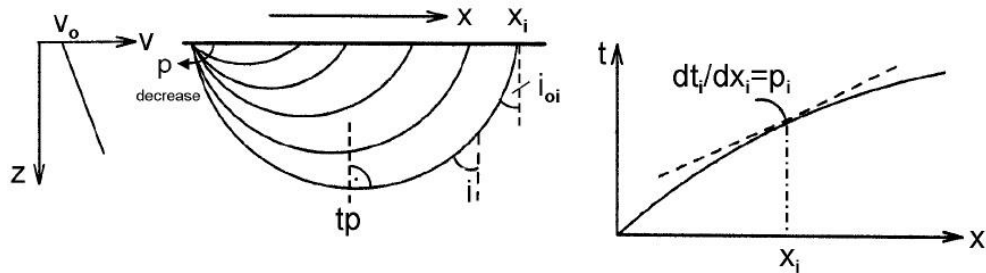


Figure 2.6. Simple model of continuous velocity increase with depth (left) and corresponding ray paths (middle) and travel-time curve (right). TP represents the turning point. On the travel-time curve, the slope at each point represents the ray parameter at distance x_i at depth (after Bormann, [2012]).

The velocity model is subject to changes in other area which leads to changes in the corresponding travel-time curves. Possible velocity model changes include existence of sharp velocity increase, which can be increase in gradient (second-order discontinuity) or an instantaneous velocity jump (first order discontinuity) and existence of a low velocity zone due to changes in material such as presence of water or melts [Bormann, 2012]. The case of a low velocity zone creates a gap or shadow zone on the travel time curves. It can also possibly trap waves and create a wave guide capable of propagating long distances in case of low attenuation [Shearer, 2009]. Depending on the complexity of the problem, an appropriate ray tracing solution is needed to calculate the ray paths, travel times and ray amplitudes [Červený, 2001].

2.2.2. Reflection and Refraction and conversion of waves

When a seismic wave reaches an interface, some part of its energy is transmitted and another portion of its energy can be reflected. In addition to reflected and refracted waves of the same type, the seismic waves can also convert to other types. For example, a P wave reaching an interface, can be followed by four different rays (reflected P wave, transmitted P wave, reflected converted SV wave which is polarized in the vertical plane of propagation

and transmitted converted SV wave) as illustrated in Fig 2.7. The –converted- reflected and refracted waves also follow the Snell’s law as follows:

$$\frac{\sin i}{V_{P1}} = \frac{\sin j}{V_{S1}} = \frac{\sin i'}{V_{P2}} = \frac{\sin j'}{V_{S2}} \quad (2.7)$$

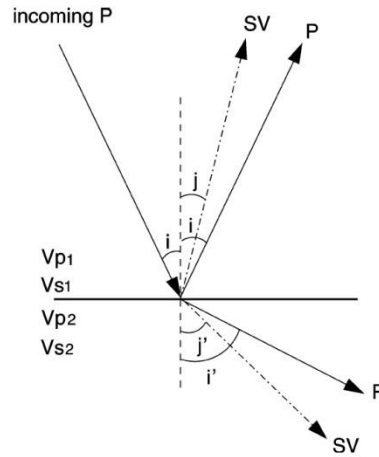


Figure 2.7. An incident P wave at a solid-solid boundary and $v_1 < v_2$ and the following –converted- reflected and refracted waves (after *Bormann*, [2012b]).

Considering velocities of P wave and S wave, the angles of transmission and reflection of the S waves are less than the ones for P waves. Furthermore, as an SH wave with purely horizontal polarization reaches and interface, only a transmitted and reflected SH wave is generated. Each case of reflection, transmission and conversion of waveforms (SH wave or P-SV waves) at each type of interface (e.g. solid-solid, solid-liquid, free interface) can be studied in detail separately. The angles of reflection and transmission, the ray paths and travel times, depend only on the velocities, while the amplitudes depend on the elastic properties of the medium. Therefore, the amplitudes include valuable information for studying crustal structures and potentially fault zone structures [*Stein and Wysession*, 2003]. Analysis of the amount of energy that is transmitted is possible by calculation of reflection and transmission coefficients with the following simple formulation:

$$\begin{aligned} \text{Reflection coefficient: } R &\equiv \frac{A_{\text{reflected}}}{A_{\text{incoming}}} \\ \text{Transmission coefficient: } T &\equiv \frac{A_{\text{transmitted}}}{A_{\text{incoming}}} \end{aligned} \quad (2.8)$$

where A represents the amplitude of the waves. Detailed information can be found in *Introduction to Seismology*, *Stein and Wysession*, [2003].

Finally an example of calculated reflection coefficients for P and SV waves as a function of incidence angle is shown in Figure 2.8. *Huang and Ampuero*, [2011] used reflection coefficients as a part of studying the behavior of low velocity zones.

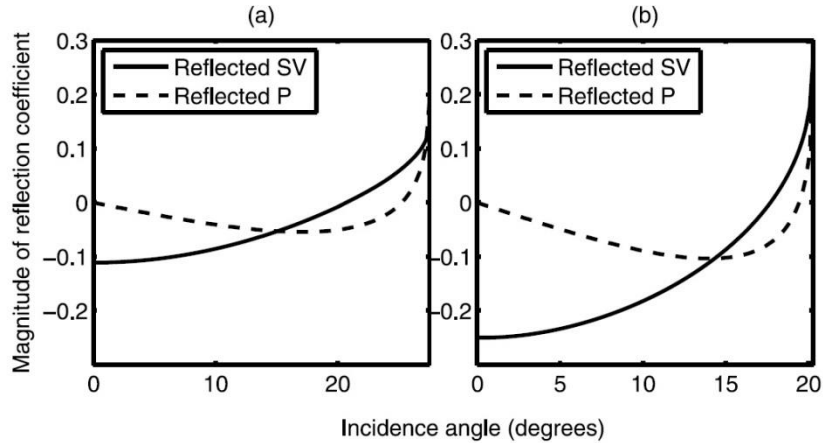


Figure 2.8. Reflection coefficients for incident SV waves at the boundary between country rock and LVFZs with velocity reductions of (a) 20% and (b) 40% respectively, as a function of incidence angle. After *Huang and Ampuero*, [2011].

In their study, the amplitude of a wave reflected back to the fault from the boundary of a low velocity fault zone (LVFZ) has an opposite sign to the one for incident wave for a certain range of incidence angles (Figure 2.8), which could mean that under certain conditions the reflected wave could unload the fault and heal the rupture, generating a slip pulse [*Huang and Ampuero*, 2011].

2.2.3. Conversions to other types in seismic phases from local and regional events.

Reflections, refractions and conversions that occur while striking an interface can reveal useful information for velocity and geological structure of the medium. At short distance, a range of seismic phases can be received by a station. Some of the common phases observed and expected of local and regional events are as follows:

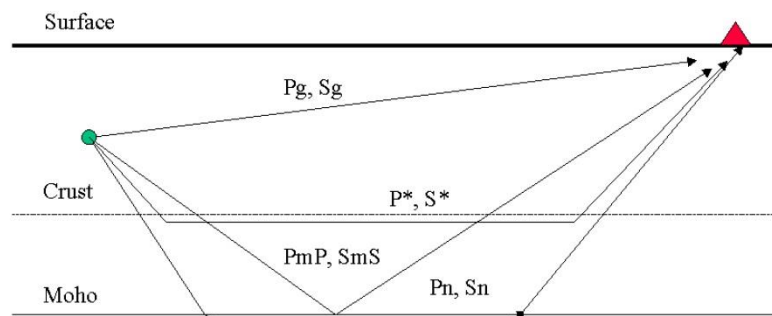


Figure 2.9. Example of various crustal phases and the corresponding ray traces observed for near (local and regional) earthquakes (after *Bormann*, [2012b]).

P_n and S_n phases propagate through the interface between the crust (with lower velocity) and mantle (with higher velocity) or basically through the uppermost mantle below the Moho [Shearer, 2009]. Rays traveling in the upper crust are denoted P_g and waves reflected in the Moho are denoted $P_M P$. Waves refracted in the lower crust are called P^* (Figure 2.9). For S waves the nomenclature is similar. As mentioned, at an interface, conversions of waves (incident P or S waves reflected or transmitted as S or P) can also occur. For rays reflected in the Moho, they are denoted $P_M S$ and $S_M P$. Depending on several factors such as thickness of the crusts, velocity profile in the area and the distance of earthquake and station, the P_g and P_n phases arrive to the station at different times [Udias, 2000]. As an example, the arrival of such phases on the seismograms, including the calculated travel-time curves and the obtained crustal model from ray tracing is shown in Figure 2.10.

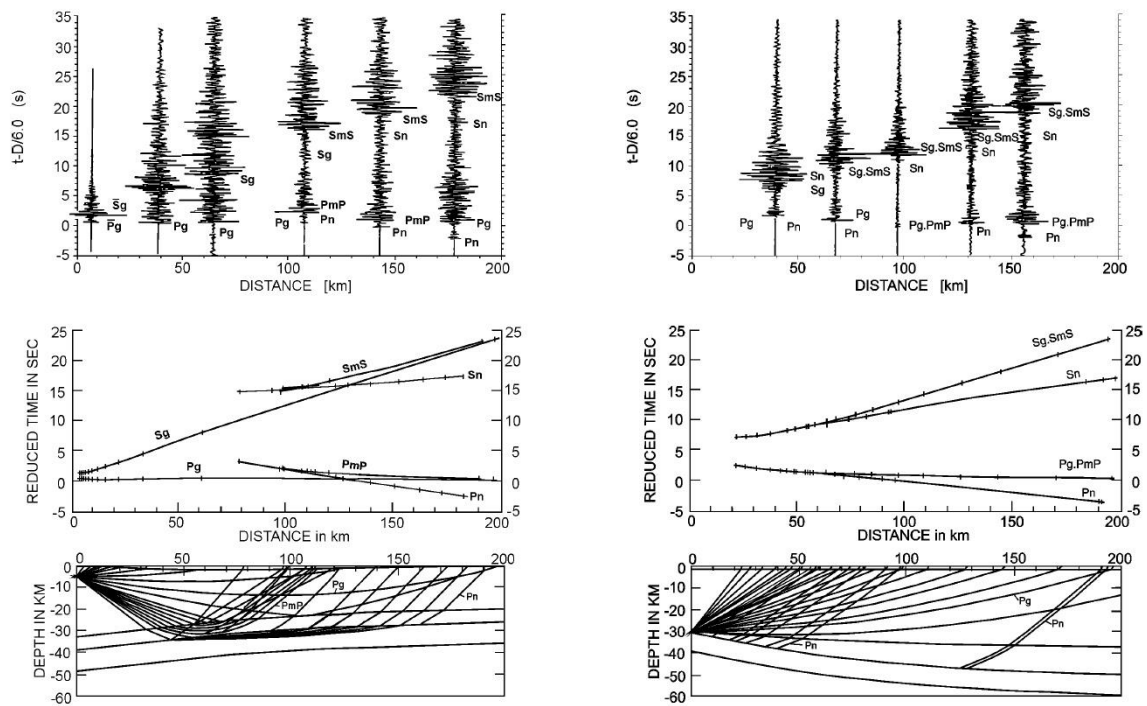


Figure 2.10 Examples of travel-time curves and ray-tracing crustal models for regional earthquakes. “Records (above) of two regional earthquakes of Oct. 9, 1986 at Sierre (left) and of July 7, 1985 at Langenthal, Switzerland together with the calculated reduced travel-time curves (middle) and ray-tracing crustal models, redrawn and complemented from Kulhánek [1990], Anatomy of Seismograms, plate 4, pp. 83-84” by Bormann *et al.* [2012, P. 56].

An important arrival on a seismogram can be a $P_M P$ phase, with large amplitudes, which can be used to determine the thickness of the crust. In seismograms of local earthquakes, the same phases mentioned above can be observed, but P_g phase has larger amplitudes beyond the critical distance and S phase have large amplitudes in the horizontal components. P_1 or P^* and S_1 or S^* rays that can be refracted or reflected at internal discontinuities of the crust, have in general small amplitudes and are observed better in seismograms of earthquakes than in seismic profiles [Udias, 2000].

2.2.4. Synthetic seismograms

The wiggles observed on a seismogram are results of several factors such as the source effects (e.g. source radiation directivity, source-time function), the propagation effects (e.g. structure and attenuation), the influence of the seismogram (e.g. sensor and recorder) and the data processing [Bormann *et al.*, 2012]. By modeling the effect of these factors on the final seismogram, one can calculate synthetic seismograms. A seismogram $u(t)$ can be written as the result of convolution of three basic filters:

$$u(t) = s(t)*g(t)*i(t) \quad (2.9)$$

where $s(t)$ is the signal from the seismic source, $g(t)$ is the propagation filter, and $i(t)$ represents the instrument response [Bormann *et al.*, 2012]. With respect to the propagation term in Eq. 2.9 it may be modelled, solving Eq. 2.5 for a media consisting of stacks of homogeneous horizontal layers. To proceed, matrixes of reflection and transmission coefficients for several layers can be used, which is also known as the propagator algorithm [Thomson, 1950; Haskell, 1953]. Another option is using generalized reflection and transmission coefficients for the entire stack of layers as performed in the discrete wavenumber method by Fuchs and Müller [1971], Bouchon, [1981]; Kennett, [1983]; Müller, [1985]. Finally, the ray tracing of Červený and Pšenčík, [1977] or Červený, [2001] is possible when assuming that variations in the elastic parameters of the media are negligible over a wavelength and for the case of high frequencies (e.g. microseismicity) their gradients tend to zero [Bormann *et al.*, 2012]. This high frequency approximation used in ray tracing methods of Červený and Pšenčík, [1977] or Červený, [2001] has the advantage, that it makes it possible decompose the wavefield into independent contributions called elementary waves. Elementary waves which propagate along rays may represent various seismic body waves propagating in different types of medium such as heterogeneous, isotropic or anisotropic layers or block structures. These possible waves include direct, reflected, converted or

multiply reflected/transmitted waves. The great advantage of the ray method is that the individual elementary waves can be treated separately [Červený *et al.*, 2007]. The ray tracing method of Červený and Pšenčík,[1984] is used to calculate the synthetic seismograms considering a steeply inclined interface as reflector/convertor of phases as will be described in chapter 5 of this thesis.

According to Brossier and Virieux, [2011], the approximations used by Červený, [2001] are useful for interpretation, but face difficulties in complex geological setting, therefore a different approach for solving the complete differential equations (or corresponding integral equations) with numerical methods is needed. These alternatives use boundary discretization, which makes them more efficient and include reflectivity methods [Kennett, 1983] or generalized screen methods [Wu, 2003] or Bouchon's [Bouchon *et al.*, 1989] discrete wavenumber methods [Brossier and Virieux, 2011]. Bouchon, [1981] presented a new method to calculate Green's functions (propagator role in Eq. 2.11) for an elastic layered media, where the Green's functions can be expressed as a double integral over frequency and horizontal wavenumber. The wavenumber integral for each time window can be represented by a discrete summation. "This discretization is achieved by considering, centered on the point source, an infinite set of specified circular sources distributed at equal radial interval. By choosing this interval such that disturbances from the circular sources arrive at the observation point after the time of interest, the single source solution may be retrieved from the time domain calculation" [Bouchon, 1981, P. 971]. This approach will be used in chapter 5 to calculate the synthetic seismograms for a horizontal converting interface.

2.2.5. Imaging crustal discontinuities with local earthquake data

In local earthquake tomography parameters of earthquake hypocenters and velocities of P- and S-waves are inverted by using first-arrival delay-times [e.g., Thurber, 1983; Michelini and McEvilly, 1991; Hole, 1992; Le Meur, 1997; Monteiller *et al.*, 2005], which can be used for subsurface imaging. Recent studies [e.g. Chavez-Perez S. and Louie, 1998; Stroujkova and Malin, 2000; Chavarria *et al.*, 2003; Latorre *et al.*, 2004, Nisii *et al.*, 2004] used microearthquakes as controlled sources for crustal-scale imaging with reflected, transmitted and converted waves in addition to the analysis of travel-times of other common phases such as direct P and surface waves [Latorre *et al.*, 2008].

As an example *Stroujkova and Malin*, [2000] used the recordings of a forty-station seismographic network operating in Long Valley caldera in California with secondary phases (some of which were converted *S*-to-*P* reflections), that could be seen on several stations throughout the network. The reflection point of the observed converted *S*-to-*P* phases was imaged using time-domain signal migration and stacking under the assumptions of first-order scattering theory [*Stroujkova and Malin*, 2000].

Furthermore recently *Hrubcová et al.* [2016] used microearthquakes to image crustal discontinuities in two separate case studies of KTB drill site and west Bohemia swarm area. In their method the depth of discontinuities is modeled using several independent tools provided by refraction and reflections seismics combined with the earthquake source analysis. Ray tracing [Červený, 2001] was used for calculating travel times of converted and/or reflected phases. Focal mechanisms and radiation patterns for converted/reflected phases were analyzed as well. Furthermore, full waveform modeling using the discrete wave number method [*Bouchon*, 1981] as described in section 2.2.4. was performed for comparing synthetic full wavefields with the observed data.

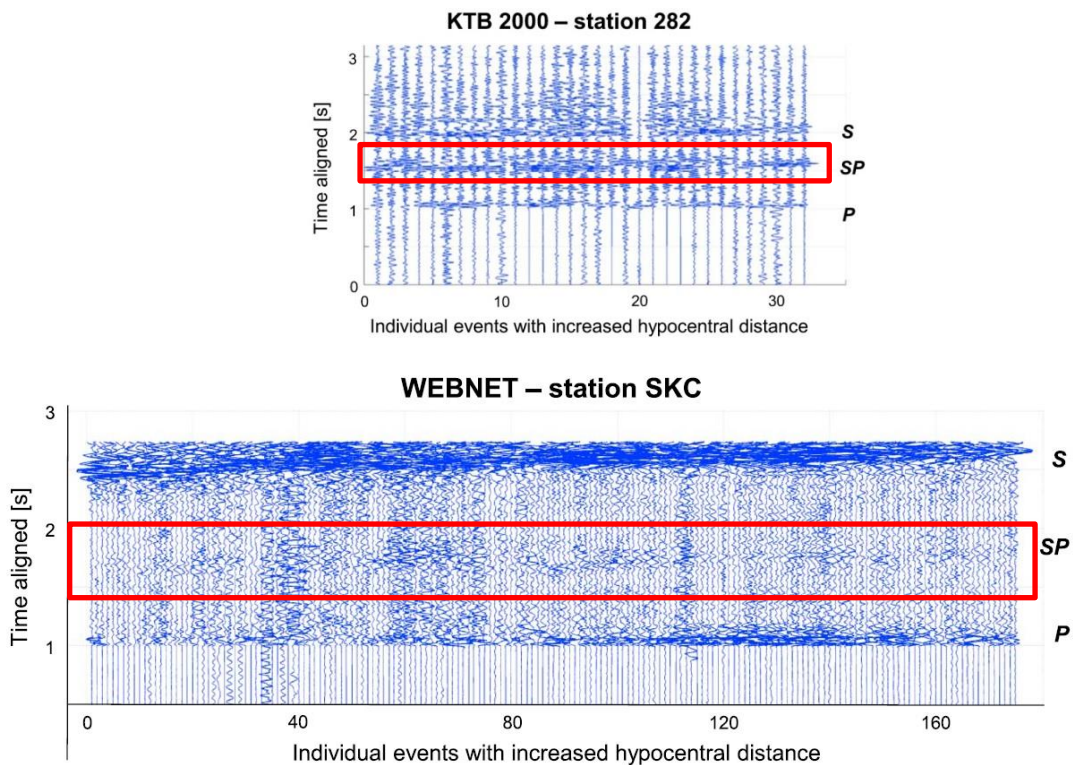


Figure 2.11: Example of the vertical component high-frequency velocity waveforms with converted *SP* phases. The waveforms are recorded at a station of the KTB network (filtered by 10–40 Hz and hypocentral distance 7.1–7.7 km) and station SKC of the WEBNET network (filtered by 2. 5–30 Hz and hypocentral

distance 11.2–13.1 km). The converted SP phases (enclosed by red box) can be clearly identified in between the P and S waves and are generated at a shallow local subsurface structure [Hrubcová *et al.*, 2016].

Alignment of traces and their stacking for amplifying studied phases, and finally a grid search method for the inversion was used. In their analysis, they mainly focused on the SP converted (Figure 2.11) waves generated at shallow crustal interfaces above seismoactive hypocentral zones at depths between 2 and 6 km. At these depths, the SP phases were well pronounced and reasonably separated from the P wave coda. Also the PPP reflections from local uppermost structure, which mostly represent reflections from the top of unweathered crystalline rocks or bottom of a sedimentary layer with depths of 200–500 m were analyzed [Hrubcová *et al.*, 2016].

In both cases of KTB (induced seismicity associated with fluid injections) and west Bohemia (natural swarm seismicity), the analysis were successful and provided interesting results with tectonic implications.

3. Tectonic setting of areas of study

The North Anatolian fault zone (NAFZ) is one of the largest plate-bounding transform faults separating the Anatolian and Eurasian plates. Located in the NW Turkey it trends approximately east-west along a 1300 km boundary between the Eastern Anatolia and the Northern Aegean [e.g., *Sengör et al.*, 2005; *Bohnhoff et al.*, 2016a]. The westward movement of Anatolia is a result of the northward moving Arabian plate and the southward rollback of the Hellenic Subduction Zone where the African lithosphere is subducted below the Aegean [e.g., *Flerit et al.*, 2004; *Bohnhoff et al.*, 2005; *Bulut et al.*, 2012b]. The current right-lateral slip rate along the NAFZ is 20-30 mm/yr [e.g., *Barka*, 1992, 1999; *McClusky et al.*, 2000], repeatedly producing major ($M_w > 7$) strike-slip earthquakes. During the 20th century, the NAFZ has ruptured over 900 km of its length [*Ambraseys and Zatopek*, 1969; *Barka et al.*, 2002] with a series of large earthquakes migrating generally westward towards the Istanbul-Marmara region in the NW Turkey. The most recent $M_w > 7$ earthquakes in the NAFZ occurred in 1999: the M_w 7.4 İzmit earthquake and the M_w 7.1 Düzce earthquake (Figure 3.1) [e.g., *Tibi et al.*, 2001; *Bohnhoff et al.*, 2016a]. They occurred, where the NAFZ splays into two branches: the Karadere-Düzce fault in the north and the Mudurnu fault in the south with the Paleozoic-Eocene rocks of the Almacik block in-between (Figure 3.1b).

In the first study explained in chapter 4, the structural properties of the Karadere segment of the NAFZ located towards the eastern part of the 120 km long surface rupture of the İzmit event (Figure 3.1b+c) is studied. The Karadere segment is important for understanding the seismo-mechanical setting of this region, since it is located between the extensional Akyazi and Düzce Basins [*Bulut et al.*, 2007; *Görgün et al.*, 2010]. The Karadere fault has a local strike of $N65^\circ E$ while the NAFZ strikes EW on average. The Karadere fault sustained a right-lateral coseismic slip of about 1.5 m during the İzmit earthquake, which is substantially less than at the nearby Sapanca segment to the east that had a coseismic displacement of 5-6 m [e.g., *Tibi et al.*, 2001; *Barka et al.*, 2002]. This variation in lateral slip caused EW-extensional normal faulting aftershocks at the Akyazi pull-apart basin that is located in between (Fig 3.1b) [*Bohnhoff et al.*, 2006]. Further to the east where the İzmit rupture stopped within the transition from the Düzce fault towards the Düzce Basin, the M_w 7.1 Düzce rupture nucleated after 87 days extending the rupture by

~40 km to the east and re-rupturing parts of the Düzce fault [Hartleb *et al.*, 2002; Hearn *et al.*, 2002].

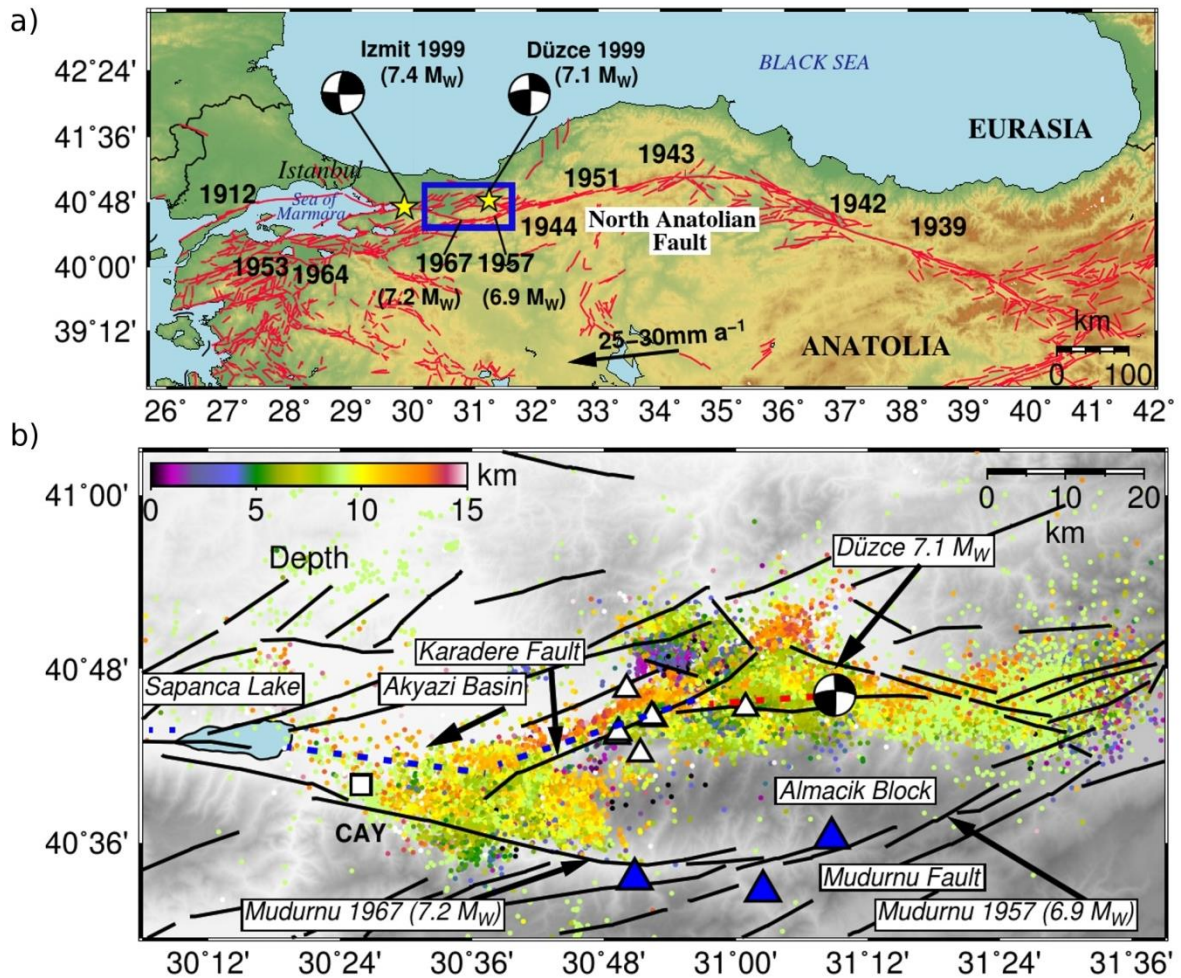


Figure 3.1. Areas of study. (a) Regional tectonic framework of the northern Anatolian region with the North Anatolian Fault Zone (NAFZ, red lines) as the right-lateral transform plate boundary between Anatolia and Eurasia. Current right-lateral slip along the NAFZ is 20-30 mm/yr increasing from east to west [McClusky *et al.*, 2000]. Black numbers indicate year and location of $M > 7$ earthquakes in the 20th century. The most recent ones, the 1999 Izmit and Düzce earthquakes are marked by yellow stars with corresponding focal mechanisms (data after Özalaybey *et al.* [2002]). The blue rectangle marks the area of study and is enlarged in (b). (b) Study area including the eastern part of the Izmit rupture (blue dashed line) and the Düzce rupture (red dashed line) after Barka *et al.* [2002], Sapanca, Akyazi and Karadere segments, and the Mudurnu fault (a NAFZ branch that was not activated during the 1999 earthquakes). Additional NAFZ branches and nearby mapped faults are indicated by the black lines (data after <http://deprem.gov.tr/>). The seismicity represents aftershocks of the Izmit and Düzce events and is color-encoded with depth. The focal mechanism shows the location and faulting mechanism of the Düzce earthquake. White triangles are selected seismic stations of the PASSCAL-network [Seeber *et al.*, 2000] that were used in FZHW analysis study as described in chapter 4. Blue triangles stand for SABONET [Milkereit, 2000] stations used in the study of imaging the Mudurnu

segment of the NAFZ as described in chapter 5. The white square is station CAY from the SABONET network, where a velocity contrast across the NAFZ of at least 6% was found [Bulut *et al.*, 2012a].

The Karadere segment is located between the Akyazi and Düzce releasing bends and is a steeply ($\sim 67^\circ$) N-dipping strike slip fault [Bulut *et al.*, 2007], reflecting mostly right-lateral strike slip aftershocks in general correspondence with the regional stress field [Bohnhoff *et al.*, 2006; Görgün *et al.*, 2010]. At present no information on the crustal velocity structure on the opposite sides of the fault is available.

In the second study, described in chapter 5, the main focus is on the Mudurnu segment of the NAFZ (figure 3.1b). The Mudurnu segment of NAFZ connects with the Karadere fault below the Akyazi pull-apart basin in the west and the Düzce fault in the east. It represents the southern boundary of the uplifted crustal Almacik Block and ruptured most recently during the 1957 Mw 6.9 and 1967 Mw 7.1 earthquakes [Ambraseys and Zatopek, 1969].

Based on teleseismic tomography, further to the west of Almacik block was identified as a high-velocity body down to the base of the crust [Papaleo *et al.*, 2017]. Velocity contrast across the western part of the Mudurnu fault was studied using FZHW by Bulut *et al.* [2012a], where an average contrast of at least 6%, with the south block being the faster side was found.

The moment tensors and focal mechanisms of aftershocks of the 1999 İzmit earthquake were studied by Stierle *et al.* [2014a;b]. Though the events located in the Karadere-Düzce segment displayed significant differences in moment tensor solutions, they exhibited only a small percentage of non-DC components, which, if existed, were mainly positive and decreased with time after the mainshock indicating a crustal healing process [Stierle *et al.*, 2014b]. These results correlated well with the predominant strike-slip stress regime along the Karadere-Düzce segment and also with the mainshock rupture being right-lateral strike-slip and temporarily introducing a dominantly normal-faulting regime [Bohnhoff *et al.*, 2006; Ickrath *et al.*, 2014, 2015]. This is also in agreement with the fault plane solutions of Örgülü and Aktar [2001] reflecting the complex source processes of the August 17, 1999 İzmit earthquake and local variations in the seismotectonic setting [Li *et al.*, 2002].

The shear-wave splitting analysis of aftershocks following the 1999 Mw 7.4 İzmit earthquake enabled to delineate stress- and structure-controlled anisotropy in the upper crust along the western NAFZ [Hurd and Bohnhoff, 2012; Eken *et al.*, 2013]. Dominant fast

shear-wave polarization of the NW-SE direction is parallel or subparallel with the strike of the regional maximum horizontal compressive stress and suggests a stress-controlled anisotropy in the study area. At some places, structure-controlled anisotropy was determined as possibly related to aligned macroscopic features associated with the Mudurnu fault [*Hurd and Bohnhoff, 2012*].

The maximum observed earthquake magnitudes along different sections of the North Anatolian Fault Zone (NAFZ) in relation to the age of the fault activity, cumulative offset, and slip rate and maximum length of coherent fault segments was discussed by *Bohnhoff et al.* [2016b]. According to that study, the largest M7.8–8.0 earthquakes are exclusively observed along the older eastern part of the NAFZ that also has longer coherent fault segments. One of these segments is examined for existence of bimaterial interfaces in this thesis, which will be described in chapter 6. In contrast to the older eastern parts of the NAFZ, the maximum observed events on the younger western part where the fault branches into two or more strands are smaller [*Bohnhoff et al., 2016b*].

The occurrence of several $M > 7$ earthquakes particularly in the 20th century along the NAFZ and the expectation upcoming large earthquakes especially in the vicinity of cities with large population such as Istanbul [*Bohnhoff et al., 2013*] shows the importance of analysis of fault zone structures across and along the NAFZ.

4. Bimaterial interfaces at the Karadere segment of the North Anatolian Fault, northwestern Turkey

Summary

We image velocity contrast (bimaterial) interfaces along the Karadere Fault of the North Anatolian Fault Zone, toward the eastern part of the 1999 Izmit Mw 7.4 rupture in NW Turkey, using waveforms recorded by a local seismic network. Applying an automatic procedure for identification and picking of fault zone head waves (FZHW) and direct P arrivals, and manually revising the picks through particle motion analysis, we identify two different groups of FZHW as well as fault zone reflected waves (FZRW). The first group of FZHW has a moveout with respect to the direct P arrivals with distance traveled along the fault, indicating a deep bimaterial interface down to the base of the seismogenic crust with an average velocity contrast of $\sim 3.4\%$. The second group of FZHW has a constant time difference from the direct P arrivals and is associated with a shallow local interface bounding a low-velocity damage zone or basin structure that extends to a depth of 4–5 km. While the first group of FZHW exists on the slower crustal block, the second group of FZHW and the FZRW are present generally on both sides of the fault. These phases add to the richness and complexity of the early P waveforms observed at stations close to a large fault. The relatively low velocity contrast across the Karadere Fault compared to values to the west may have helped stopping the Izmit rupture.

4.1. Introduction

Large fault zones have bimaterial interfaces that separate different lithologies. These are generated by the long-term offset along the fault, cumulative rock damage products and other fault-zone-related structures such as basins and mountains. The existence of different rock types within and across fault zones can modify the properties of the local seismic and geodetic fields [e.g., *Ben-Zion and Aki, 1990; Le Pichon et al., 2005; Özeren and Holt, 2010*]. This is relevant for numerous topics including earthquake locations, focal mechanisms, Moho topography below the fault, delay times of teleseismic waves, interseismic strain fields and near-fault amplification of ground motion [e.g., *Oppenheimer et al., 1988; Ben-Zion and Malin, 1991; Schulte-Pelkum and Ben-Zion, 2012; Ozakin et al., 2012; Wdowinski et al., 2007; Kurzon et al., 2014*]. Moreover, bimaterial fault interfaces can affect significantly the mode, dynamic properties and propagation direction of earthquake ruptures [e.g., *Ben-Zion, 2001; Ampuero and Ben-Zion, 2008; Lengliné and Got, 2011; Calderoni et al., 2015*], along with space-time variations of seismicity along the fault [e.g., *Rubin and Gillard, 2000; Zaliapin and Ben-Zion, 2011*] and generation of small-scale local structural properties [e.g., *Dor et al., 2008; Wechsler et al., 2009; Ben-Zion et al., 2012*].

Basin structures are common along faults and are known to be generated in "pull-apart" places where transtensional deformation separates neighboring crustal blocks by a lateral offset in combination with an extensional stress field [e.g., *Burchfiel and Stewart, 1966; Crowell, 1974; Sibson, 1986, Hubert-Ferrari et al., 2002; Bohnhoff et al., 2006*]. In addition to pull-apart basins, local structures with low velocity rocks can be generated by the cumulative damage process along the fault [e.g., *Lyakhovsky and Ben-Zion, 2009; Finzi et al., 2009*]. Broad zones with damaged low velocity rocks have been documented around numerous large faults based on seismic, gravity, geodetic and other data. As examples, *Hamiel and Fialko, [2007]* inferred on the existence of several km wide damage zone around the North Anatolian Fault Zone (NAFZ) from InSAR observations associated with the 1999 Izmit earthquake. *Allam and Ben-Zion, [2012]* and *Zigone et al., [2015]* imaged with earthquake- and noise-based tomography zones with similar width of reduced seismic velocities around the San Jacinto fault zone in southern California.

In the present chapter we use the above properties to identify and analyze FZHW and direct P arrivals in near-fault seismic data recorded along the Karadere segment of the NAFZ. In the next section we describe the study area and employed seismic data. In section

4.3 we perform detailed analysis of the early portions of P waveforms recorded close to the Karadere segment. We find abundant evidence for two different groups of FZHW that propagate both along a deep bimaterial interface and along an edge of a shallow low velocity zone or a basin structure around the fault. In addition to FZHW, we observe secondary P waves that appear to be reflected from interfaces in the fault zone structure. We refer to these phases as fault zone reflected waves (FZRW). The results are discussed and summarized in section 4.4 of the paper.

4.2. Data

To study the possible existence of bimaterial interfaces in the structure associated with the Karadere fault, we use waveform data recorded by the local seismic PASSCAL network that was deployed within one week after the Izmit earthquake along and around the Karadere-Düzce sections of the NAFZ (Figure 4.1b+c) [Seeber *et al.*, 2000; Ben-Zion *et al.*, 2003]. The network operated for about 6 months with the goals of monitoring local aftershock activity at low-magnitude detection threshold and studying the subsurface structure of the Karadere-Düzce sections. Most sites had a mixture of 3-component L22 sensors and 3-component force-balance accelerometers. Sites MO (for the full deployment) and GE (for the first two months) had three-component broad-band (Guralp CMG-40T) sensors. The choice of location was fortunate since three months after the deployment the Düzce earthquake nucleated, propagating back to the network location and further to the east. The network recorded waveforms at on- and off-fault stations generated by > 25,000 earthquakes detected with standard techniques. This data set was used previously to image trapping fault zone structure [Ben-Zion *et al.*, 2003], crustal anisotropy [Peng and Ben-Zion, 2004; 2005], temporal changes of seismic velocities [Peng and Ben-Zion, 2006; C Wu *et al.*, 2009] and earthquake source properties [Yang *et al.*, 2009]. However, bimaterial interfaces that are the focus of this work were not targeted for imaging so far. To image bimaterial interfaces we use 7 stations from the network that recorded significant amount of data at on- and off-fault locations along the Karadere fault, including one station (BV) further east at the Düzce fault (Figure 4.1b+c).

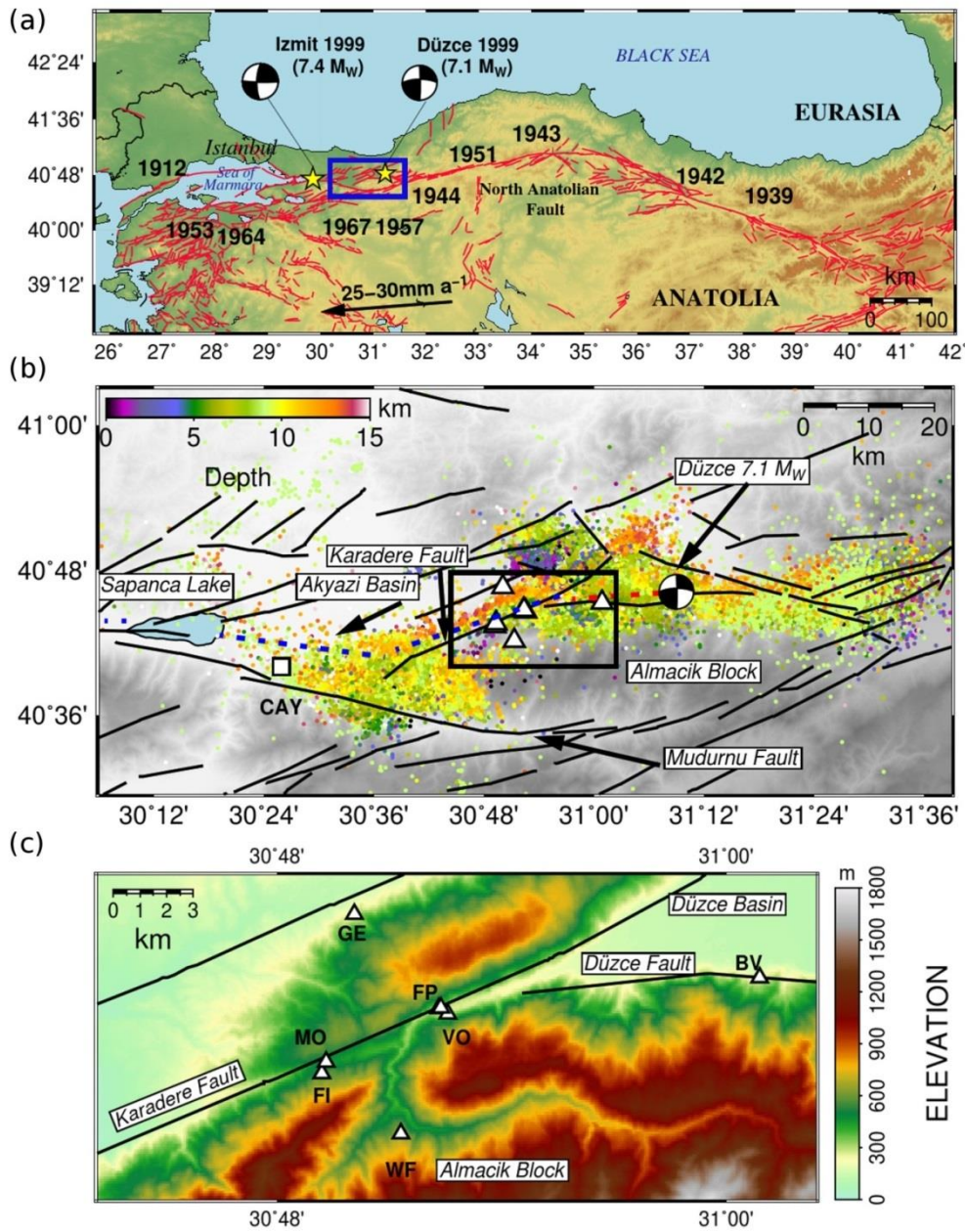


Figure 4.1. Karadere Fault and the seismicity studied (a) Regional tectonic framework of the northern Anatolian region with the North Anatolian Fault Zone (NAFZ, red lines) as the right-lateral transform plate boundary between Anatolia and Eurasia. Current right-lateral slip along the NAFZ is 20–30 mm/yr increasing from east to west [McClusky *et al.*, 2000]. Black numbers indicate year and location of $M > 7$ earthquakes in the 20th century. The most recent ones, the 1999 Izmit and Düzce earthquakes are marked by yellow stars with corresponding focal mechanisms (data after Özalaybey *et al.*, 2002). The blue rectangle marks the area of study and is enlarged in b). (b) Study area including the eastern part of the Izmit rupture (blue dashed line) and the Düzce rupture (red dashed line) after Barka *et al.* [2002], Sapanca, Akyazi and Karadere segments, and the Mudurnu fault (a NAFZ branch that was not activated during the 1999 earthquakes). Additional NAFZ branches and nearby mapped faults are indicated by the black lines (data after <http://deprem.gov.tr/>). The

seismicity represents aftershocks of the Izmit and Düzce events and is color-encoded with depth. The focal mechanism shows the location and faulting mechanism of the Düzce earthquake. White triangles are selected seismic stations of the PASSCAL-network [Seeber *et al.*, 2000] that were used in this study. The white square is station CAY from the SABONET network [Milkereit, 2000], where a velocity contrast across the NAFZ of at least 6% was found [Bulut *et al.*, 2012a]. The black rectangle indicates the area of the stations used and is enlarged in c). (c) Seismic stations along the Karadere Fault that is bounded by the Düzce Basin and Düzce Fault in the northeast, by the elevated crustal Almacik Block in the southeast.

4.3. Data Analysis and results

To analyze the data systematically, we follow the processing steps shown in the flowchart of Figure 4.2. We begin with comprehensive automatic identification and picking of candidate FZHW and direct P arrivals using the algorithm of *Ross and Ben-Zion*, [2014] based on various characteristics of both wave types, including first-motion polarities, time difference, sharpness and amplitude variations. The method was shown to perform well on data recorded near the Parkfield section of the San Andreas fault, the Hayward fault and sections of the San Jacinto fault zone in California [Ross and Ben-Zion, 2014; Share *et al.*, 2015; Qiu *et al.*, 2015].

The algorithm has several parameters including a frequency range for filtering in a preprocessing stage, values of short-term average/long-term average (STA/LTA) time windows, a range of time differences between FZHW and direct P arrivals (corresponding to minimum and maximum expected velocity contrast). The values of the parameters used in this study (Table 4.1) are the same as in *Ross and Ben-Zion*, [2014].

The locations of the used events were determined by standard analysis with an approximate velocity model [Seeber *et al.*, 2000; Ben-Zion *et al.*, 2003] and they have uncertainties of about 2-3 km or more. The event locations are distributed broadly around the main NAFZ (Figure 4.1b) reflecting, at least partially, structural complexity in the study area. The location uncertainties prevent us from selecting a subset of events that are highly localized along the fault. Instead we simply run the automatic picker on all data and analyze candidate detections as summarized in Figure 4.2 and described below.

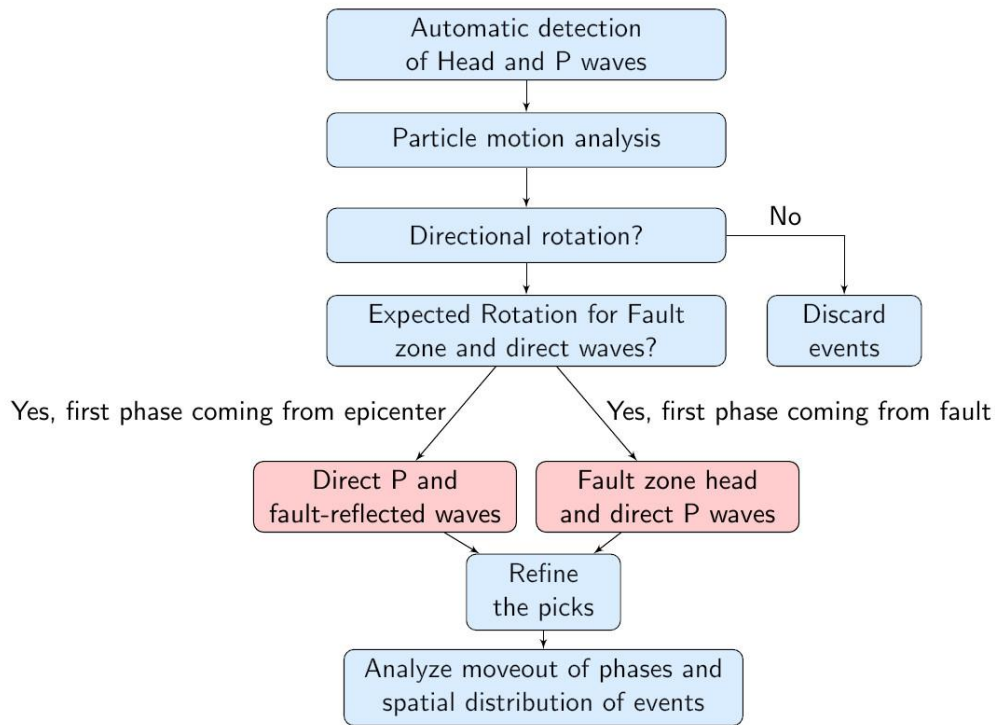


Figure 4.2. Flow chart showing the data analysis procedure applied in this study. The two important pairs of seismic phases (direct P and FZRW, or FZHW and direct P) identified and analyzed in this study are indicated in the two pink boxes.

Maximum velocity contrast	0.1
Minimum distance allowed	0
Corner frequency of high-pass filter (Hz)	0.5
Padding to be added (sec) to start of trace if not enough	0
Short-term average (STA) and long-term average (LTA) time windows	0.1, 10
Minimum time separation allowed between FZHW and direct P	0.065
P-wave velocity on fast side (km/s)	5.5
Sliding window length (sec) for kurtosis/skewness	5
Start/end coordinates of fault	40.7,30.6 - 40.77,31.35

Table 4.1. Parameters used in the algorithm of automatically picking Fault Zone Head Waves (FZHW) and direct P waves.

We examine about 100,000 waveforms at the different stations (Table 4.2). In most cases the analysis does not provide evidence for fault related phases, but we detect several hundreds of FZHW that are used for detailed analyses.

Figure 4.3 shows as an example detection results for station FP with (a) automatic picks of FZHW and direct P waves for hypocenters located east of the station and (b) locations of all events generating detected FZHW by the algorithm of *Ross and Ben-Zion, [2014]*.

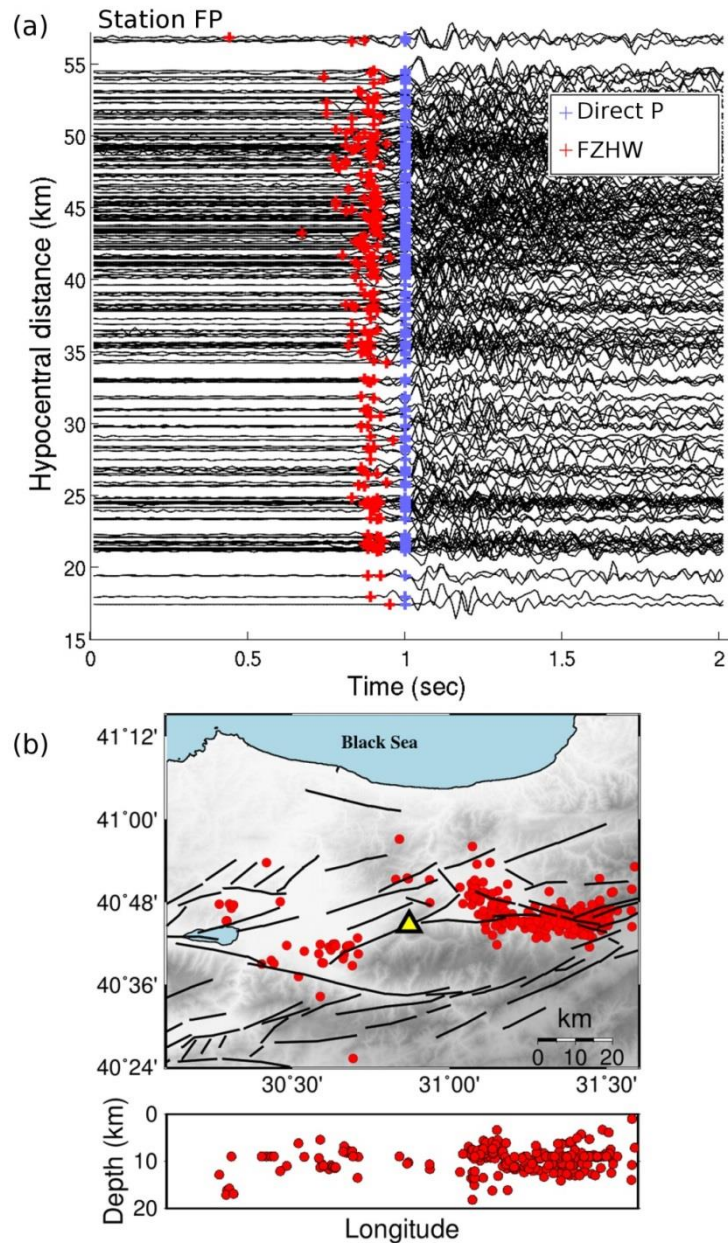


Figure 4.3. (a) Preliminary results for station FP after running the automatic algorithm to detect direct P and FZHW on all vertical seismograms of local events recorded by the station. We only show vertical seismograms on which FZHW (red crosses marking first arrivals) were detected for hypocenters located east of the station. Waveforms are aligned on the direct P arrivals (light blue crosses marking second arrivals) and plotted with hypocentral distance. (b) Epicentral map and depth section for the earthquakes used in a), as well as hypocenters of events located west of station producing detected FZHW. Station FP is marked with the yellow triangle.

Name of Station	Archive data	Examined seismograms	Detected FZHW	Final FZHW	Final FZRW
MO	1999/08/26 - 2000/12/31	14050	420	16	22
FI	1999/09/04 - 2000/02/13	13100	870	35	36
WF	1999/09/11 - 2000/02/13	17780	480	31	42
GE	1999/08/27 - 2000/02/12	16700	250	2	22
FP	1999/10/29 - 2000/02/12	11300	333	88	41
VO	1999/09/02 - 2000/02/12	19900	459	11	20
BV	1999-09/14 - 2000/02/12	15700	547	4	32

Table 4.2. List of the stations used in this analysis with their operation period, number of the seismograms that we analyzed with the automatic picker, number of FZHW detected after using the automatic picker (before any particle motion analysis), final FZHW left after the particle motion analysis and the number of FZRW found beside the final FZHW.

As a first step of our in-depth study we perform particle motion analysis on the FZHW and direct P arrivals flagged by the automatic picker, as done and described in detail by *Bulut et al.* [2012a] and *Allam et al.*, [2014]. If the directions of both waves are similar (e.g. within about 50°) the event is not used for further FZHW analysis. An event is also discarded if the two directions were different but neither is close to the fault normal direction. However, if the particle motion of one phase points approximately to the fault and the other points approximately to the epicenter of the event, the data are retained for further analysis. If the first phase appears to be radiated from the fault, as found in the previous studies mentioned above, it is labeled FZHW and the following phase is labeled direct P wave. In the course of the analysis we found a set of waveforms with reversed order of directions, namely the first phase points approximately to the epicenter direction and the second pointing to the fault. We also find that in such cases the impulsiveness of the second phase is similar to that of the first. We consider such cases to be associated with first arriving direct P body waves followed by a secondary FZRW reflected from a fault zone interface.

Figure 4.4 illustrates the particle motion analysis for one example event (panel a) with FZHW and subsequent direct P arrival. We examine both the horizontal 2D (east-west and north-south) and 3D (vertical component added) particle motion of each waveform before and after the arrival of the FZHW and direct P waves as shown in panels (b-d). Following *Allam et al.* [2014], polarizations are also calculated (panel e) in narrow time windows of the displacement seismograms with the algorithm of *Jurkevics*, [1988]. FZHW should have

larger eigenvalues than the noise and the direct P waves should have larger eigenvalues than the FZHW [Allam *et al.*, 2014]. The changes in the main azimuth of polarization between the windows corresponding to the FZHW and direct P phase should be $> 50^\circ$ to satisfy the criterion for retaining the waveform for additional analysis. Figure 4.5 illustrates similar particle motion analysis leading to identification of first arriving direct P wave followed by a secondary arriving FZRW.

The procedure discussed so far provides two categories of events and waveforms considered for further analysis: the first with a FZHW followed by a direct P phase and the second with a direct P arrival followed by a FZRW. The arrival picks of both groups are refined in the process of the particle motion analysis. To summarize the results, we plot for each station the vertical component waveforms of both groups sorted according to the hypocentral distance, aligned on the direct P arrival and with the final FZHW and FZRW picks (Table 4.2, last two columns). This is illustrated in Figure 4.6 for data recorded by station FP and summarized in Figures. 4.7-4.8 for all used stations. Some stations (e.g. GE north of the Karadere fault and BV along the Düzce fault to the east) have no or very few FZHW.

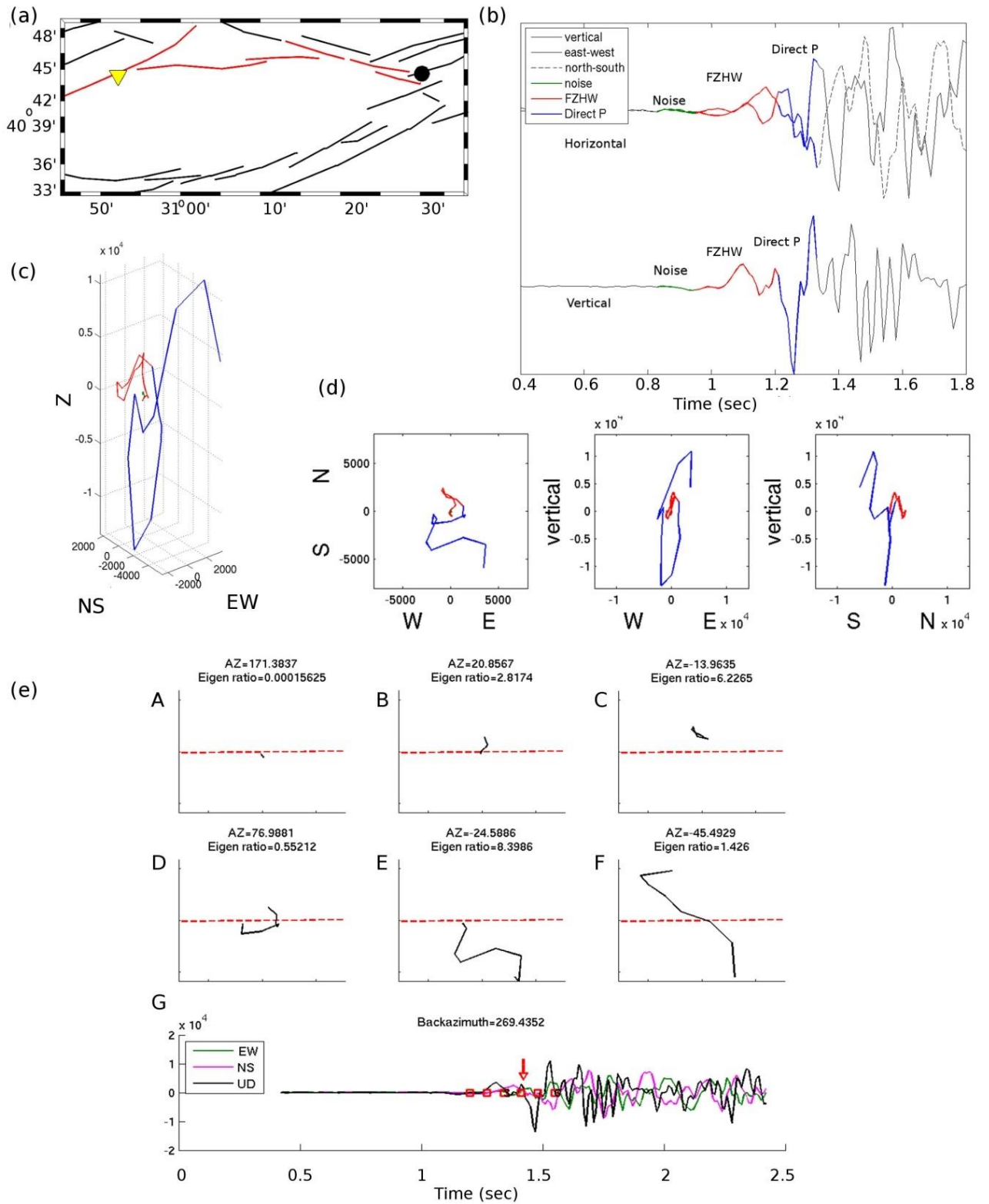


Figure 4.4. Example of a FZHW and direct P wave phases identified based on particle motion analysis. (a) Station (yellow triangle) - event (black circle) geometry in map view. The Karadere and Düzce faults are colored in red and other fault branches in black. (b) Waveforms recorded from the event shown in a) separated

into the two horizontal (above) and vertical (below) components, respectively. The north-south components are plotted with the dashed line. For each waveform the noise is plotted in green. The time window between the onset of the FZHW and the onset of the direct P wave is plotted in red. The first portion of the direct P wave is plotted in blue. Right after the FZHW arrival the two horizontal components are out of phase, while after the direct P arrival the phase shift vanishes. The polarity of the FZHW on the vertical component is positive while the direct P wave has a negative first motion in accordance with theory. (c) 3-D particle motion of noise (green), FZHW (red) and direct P wave (blue) obtained from the seismograms shown in (b). The three axes represent the EW, NS and up-down components of the seismograms. This is a useful tool to compare the changes in particle motion between noise, FZHW and direct P wave in space. (d) 2D projection of c) on the EW-NS, EW-vertical, and NS-vertical planes. In the EW-NS plane the FZHW (red) is polarized perpendicular to the fault while right after the direct P arrival (blue) it changes towards the event-station back azimuth as expected. This image is useful for future refining of FZHW and direct P wave picks if necessary. In the two other planes one can see the changes in the incidence angle between noise, FZHW and direct P wave. (e) Horizontal particle motion with a moving time window (A-F) and the respective waveforms (below) after *Allam et al.*, [2014]. Each particle motion plot corresponds to a time window marked with a square on the waveforms. The red arrow shows the direct P pick. The dashed red line on each plot represents the event-station back azimuth. Azimuth of the largest eigenvalue and the ratio of eigenvalues are shown in each window, which is a quantitative tool to track the changes of direction and amplitude between noise, FZHW and direct P wave arrivals. The FZHW onset is seen at the end of plot B and at the beginning of plot C. The arrival of the direct P wave is seen at plot D.

The results plotted in Figure 4.6-4.7 show a moveout between some FZHW and direct P waves with increasing hypocentral distance for events east of stations FI, FP and to lesser extent for station VO. This indicates the existence of a bimaterial interface across the Karadere fault at a crustal depth level. In addition, there is a substantial number of FZHW with approximately constant time difference with respect to the direct P wave. These ‘no moveout’ FZHW are observed at stations FI, MO, WF, FP and VO. A constant differential time between FZHW and direct P waves cannot be explained by a deep bimaterial interface. However, it can be produced by a shallow local bimaterial interface that affects the wavefield only near (below) the stations. We analyze and discuss this in more detail below.

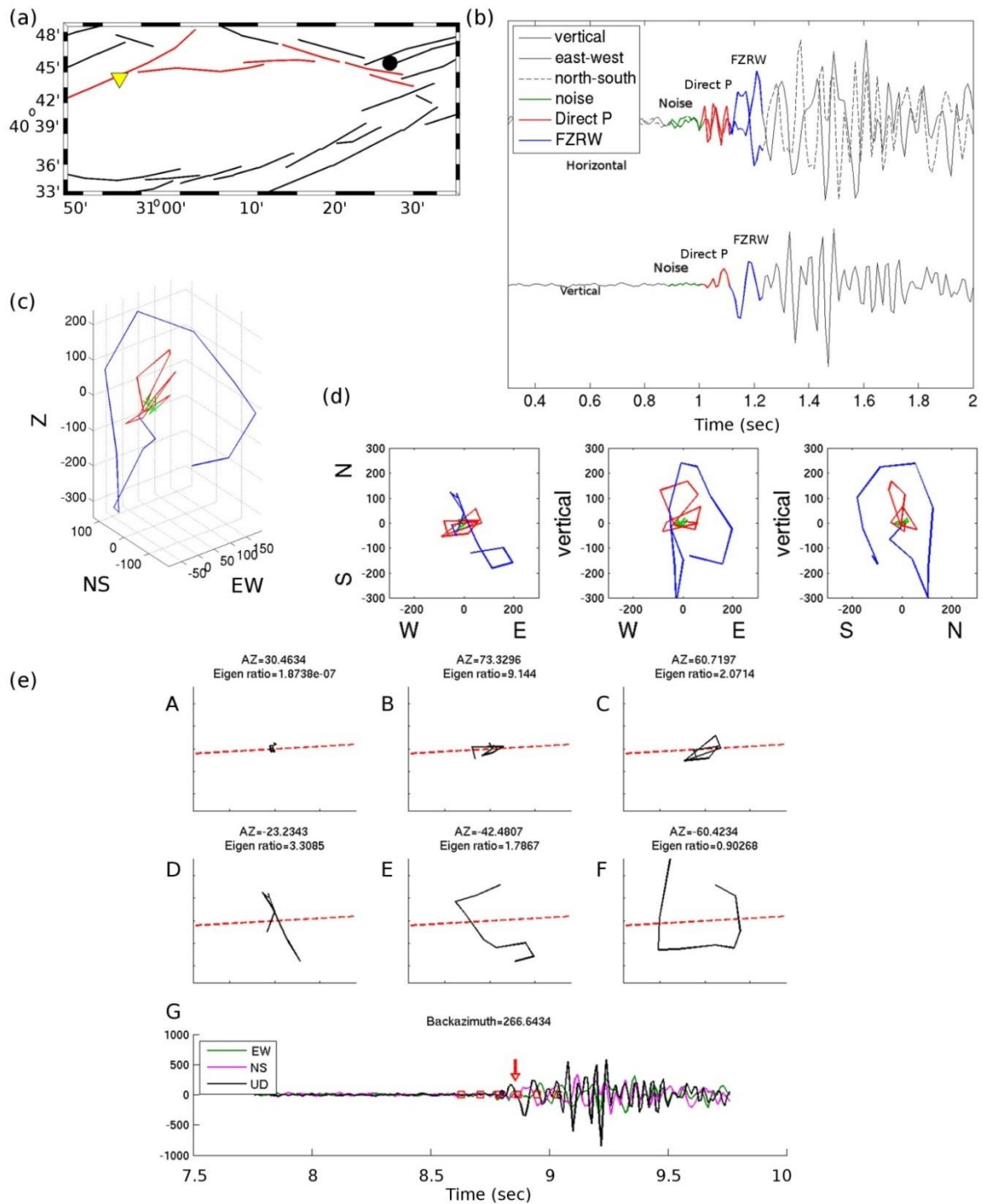


Figure 4.5. Example of a Fault-Zone Reflected Wave (FZRW) and direct P phases identified based on polarization analysis. All plots in subfigures are similar to Figure 4.4. (d) 2D particle motion plots. In the EW-NS plane, one can see that the direct P wave in red is coming from the epicenter and the later reflected phase in blue comes from the fault normal direction. This key difference from Figure 4.4-d distinguishes between the two groups with FZHW or FZRW. The NS-vertical plane shows that the FZRW comes from the north corresponding to the Karadere segment. (e) The red arrow marks the FZRW arrival corresponding to plot D in Figure 5e).

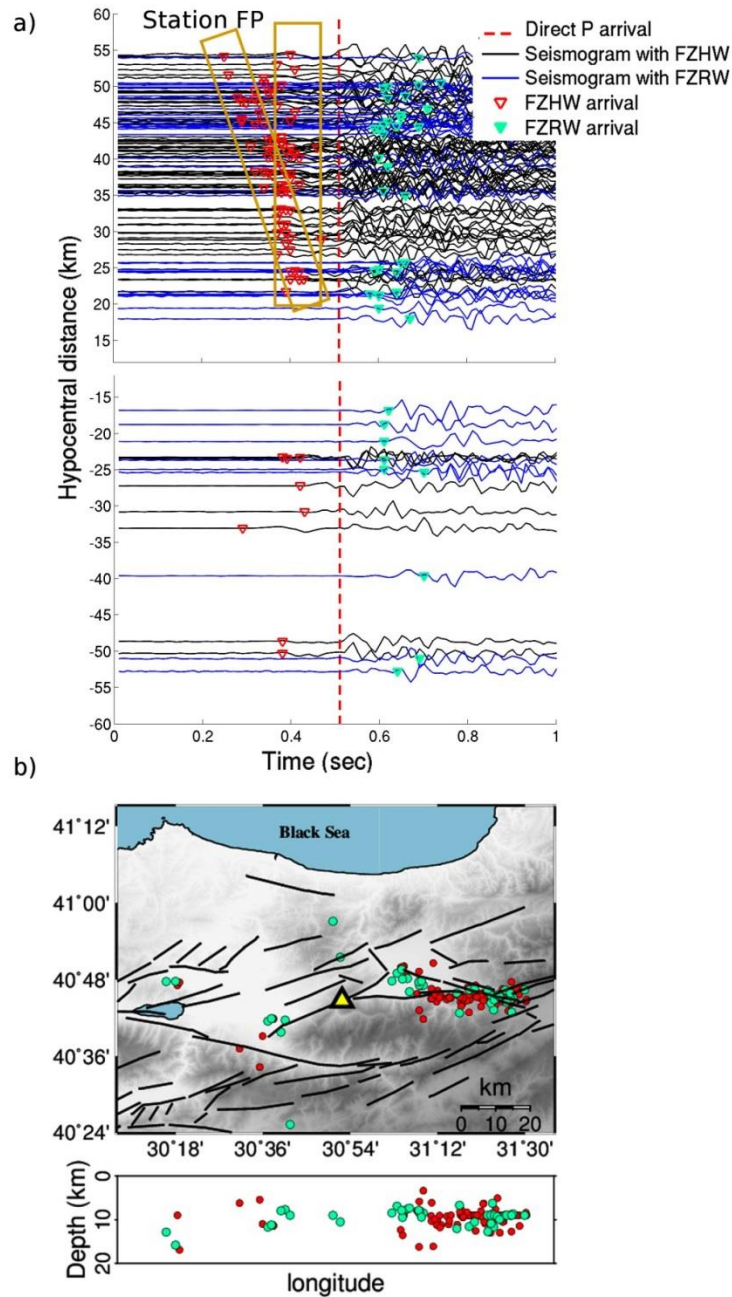


Figure 4.6. (a) Vertical component waveforms recorded by station FP with refined identification of direct P waves, FZHW and FZRW based on the particle motion analysis illustrated in Figure 4.4 and 4.5 and explained in the text. Waveforms either contain FZHW and direct P waves (color-coded in black) or direct P waves and FZRW (color-coded in blue). All seismograms are aligned on the direct P arrivals (red dashed line) and plotted with hypocentral distance. Positive and negative distance refers to earthquakes east and west of the station, respectively. FZHW arrivals are marked with red triangles (before the dashed line) and FZRW are marked with cyan triangles (after the dashed line). FZHW are divided into events showing moveout or no moveout of the FZHW with respect to direct P arrivals as framed by the yellow rectangles. (b) Epicentral (above) and depth (below) distribution of the events plotted in a). Station FP is marked by the yellow triangle. Events are color-coded as in a) where red and cyan refer to events producing FZHW or FZRW, respectively.

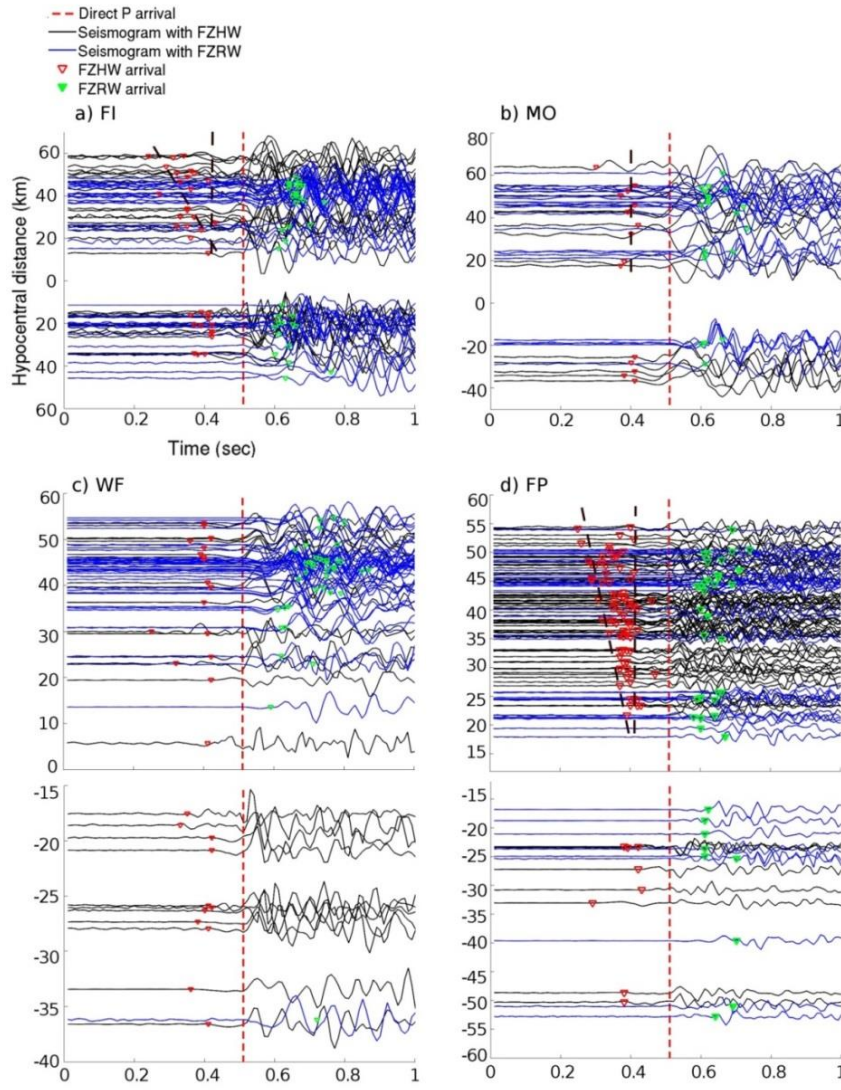


Figure 4.7. Vertical component seismograms recorded at the seven stations a) FI, b) MO, c) WF, d) FP, e) VO, f) GE and g) BV after performing the processing steps shown in Figure 4.2. A moveout between FZHW and direct P waves is seen at stations FI, FP (and to lesser extent also VO), while mostly a constant offset between FZHW and direct P waves can be identified at all stations with FZHW. Station GE located further away at northern side of the fault shows almost no FZHW but instead mostly FZRW. Station BV located further to the east of Düzce fault also shows no FZHW but instead FZRW. FZRW arrivals (after the dashed lines) are marked with green triangles and the rest of symbols are as in previous figures.

Figure 4.8 displays the epi- and hypo-central distribution of events producing ‘moveout’ and ‘non-moveout’ FZHW at different stations. Figure 4.9 shows the events producing FZHW at five stations, color-coded based on the time difference between the FZHW and direct P arrivals. We observe that events producing ‘moveout’ FZHW (warmer

colors in Figure 4.9) at stations FI and FP are located east of the stations and below 8-10 km depth.

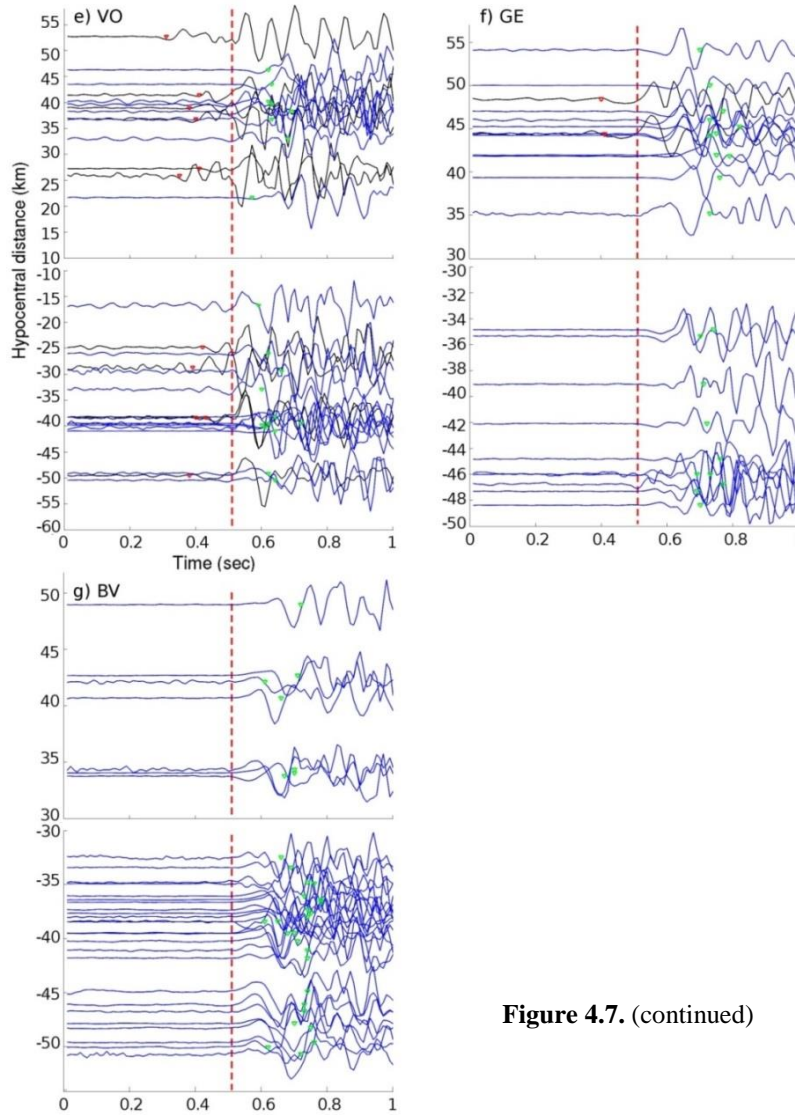


Figure 4.7. (continued)

Moreover, for station FI one can see a change from blue to red colors for increasing depth and towards the east reflecting the ‘moveout’ events. For station FP, a group of events with constant high moveout between FZHW and direct P waves is observed at a longitude of 31.4° with a depth between 6-14 km. These events may sample higher velocity contrast across the fault compared to the remaining seismicity. No systematic pattern between FZHW-P differential time and hypocenter location is observed for stations MO and VO located within the Izmit rupture/damage zone [Ben-Zion et al., 2003] and station WF south of the Karadere fault.

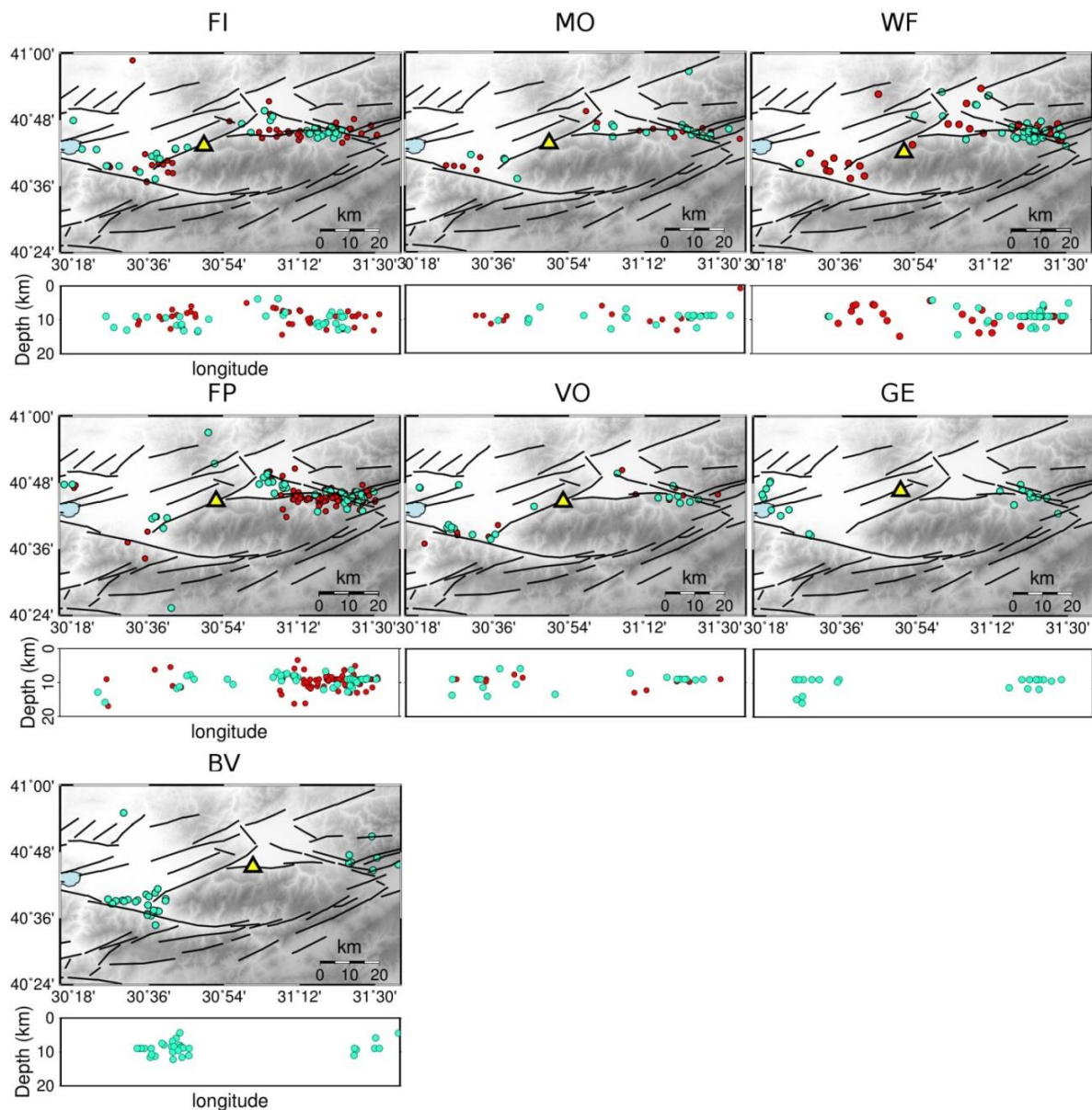


Figure 4.8. Epicentral (above) and depth (below) distribution of events for the seven stations shown in Figure 4.7 a)-g). Symbols are as in Figure 4.6b).

To infer on common characteristics of the ‘moveout’ and ‘non-moveout’ FZHW observed at the different stations, we combine all final FZHW picks from stations FI, MO, WF, FP and VO, plotting them with increasing hypocentral distance aligned with respect to the direct P pick (Fig 4.10a). A scattered but somewhat consistent pattern can be seen with a general average slope for the ‘moveout’ picks and a uniform differential time for the ‘non-moveout’ picks. The substantial scatter potentially reflects the heterogeneity of the structures below the different stations.

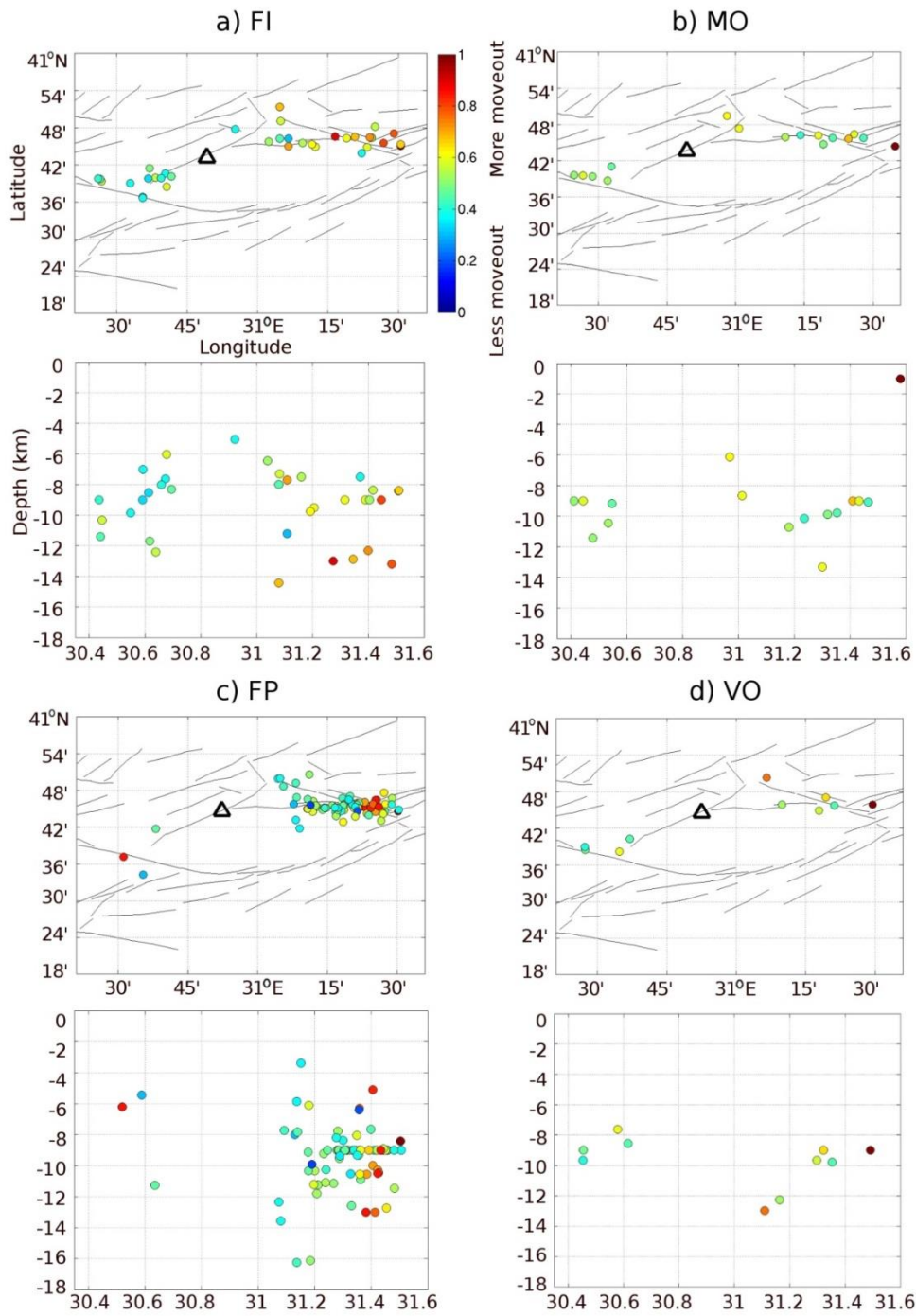


Figure 4.9. Epicentral (above) and depth (below) distribution of events producing FZHW at the five stations a) FI, b) MO, c) FP, d) VO, and e) WF, respectively (the other two stations GE and BV did not record enough FZHW, see Figure 4.7). Events are color-coded according to the differential time between direct P wave and FZHW. For each station, the differential times are normalized to the respective maximum. For stations FI and FP, a clear increase in differential time with hypocentral distance is observed indicating that the observed moveout is caused by a deep bimaterial interface. For the other stations no first-order moveout between direct P waves and FZHW was observed in the seismic sections (see Figure 4.7).

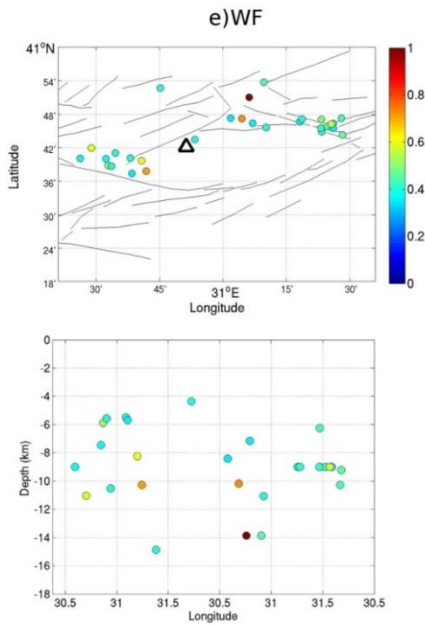


Figure 4.9. (continued)

We note that the summary plot in Figure 10a has overlapping symbols on top of each other. To better visualize the results we show in Figure 10b density plots associated with bins of 0.02 sec and 2 km length resulting in a pick density of up to 7 per bin. The shading results support the existence of two main average patterns with a consistent slope for the ‘moveout’ FZHW picks and a stable differential time for the ‘non-moveout’ picks.

To estimate the average properties of the bimaterial interfaces affecting the wavefields recorded by stations FI, MO, WF, FP and VO, we use a single pick from each bin in Figure 4.10b, to reduce the influence of multiple picks with same information, when calculating the change (moveout) of differential times vs. propagation distance. This is done in Figure 4.11a where we separate the remaining FZHW picks into two groups of ‘moveout’ (blue triangles) and ‘non-moveout’ (open red squares) arrivals. Some picks are common to the overall patterns of both groups and are considered in the estimates associated with the two groups. The locations of the events generating the wave arrivals are shown in Figure 4.11b. A least-squares fitting is done for the ‘moveout’ group separately to either general East or West direction from the stations (positive and negative hypocentral distances). The slopes are used in conjunction with Eq. 2.2 to estimate the average velocity contrast (AVC) associated with that direction. Assuming in Eq. 2.2 that the average P wave velocity for the depth section (up to 18 km) producing ‘moveout’ FZHW is 6 km/s, gives the AVC values (2.87%-3.91%) indicated in Figure 4.11a. Using instead an average P wave velocity of 5 km/s representative of shallower crustal depth decreases somewhat the AVC values (2.39% and 3.25%).

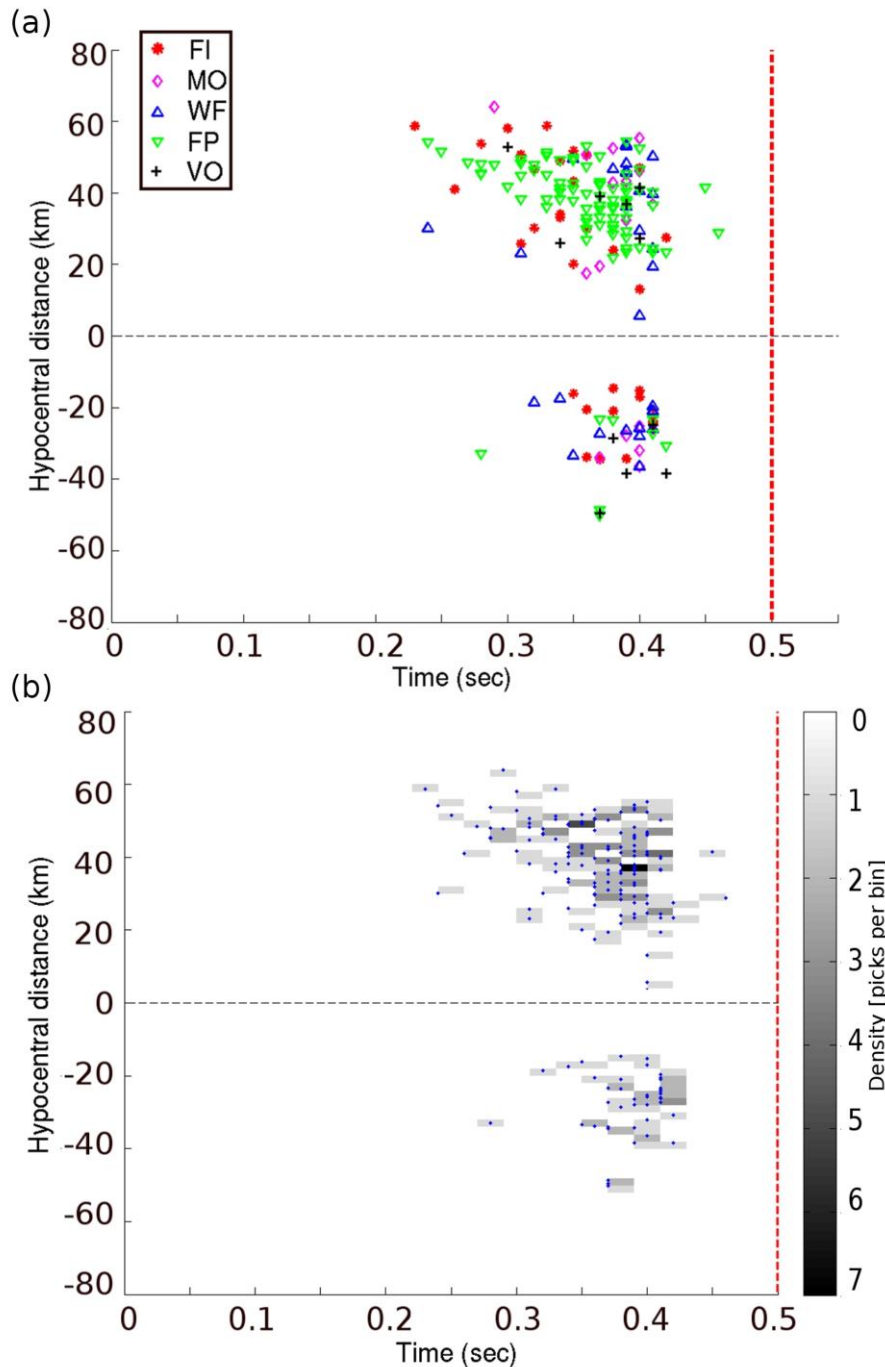


Figure 4.10.

(a) Combined plot of all five stations showing FZHW plotted with respect to the direct P arrivals (dashed line) and hypocentral distance. Positive and negative hypocentral distance refers to earthquakes occurring east or west of the respective station.

(b) Density plot showing the number of picks within each bin. The density is gray-shaded between minimum (0 picks per bin) and maximum (seven picks per bin).

Two types of errors produce uncertainties in the estimated velocity contrast across the fault. These are the location accuracy of the seismic events and the picking accuracy for the different wave used types (mainly FZHW since they have less accurate arrivals than the direct P waves). The average location uncertainty for the hypocenters is about 2-3 km [Seeber *et al.*, 2000; Ben-Zion *et al.*, 2003]. The average picking accuracy for the FZHW based on the automatic picker followed by manual changes based on the particle motion analysis is about 0.02 sec. This results in a standard deviation for the slopes at positive and negative hypocentral distances of 0.17 and 0.08, respectively. The slopes were calculated

under the assumption that the time difference between FZHW and direct P arrivals has to be zero at zero hypocentral distance (required by theory). The resulting uncertainty for the average velocity contrast of 3.4% is 0.2-0.3% (considering average velocity between 5 and 6.8 km/s for the crustal depth sampled here).

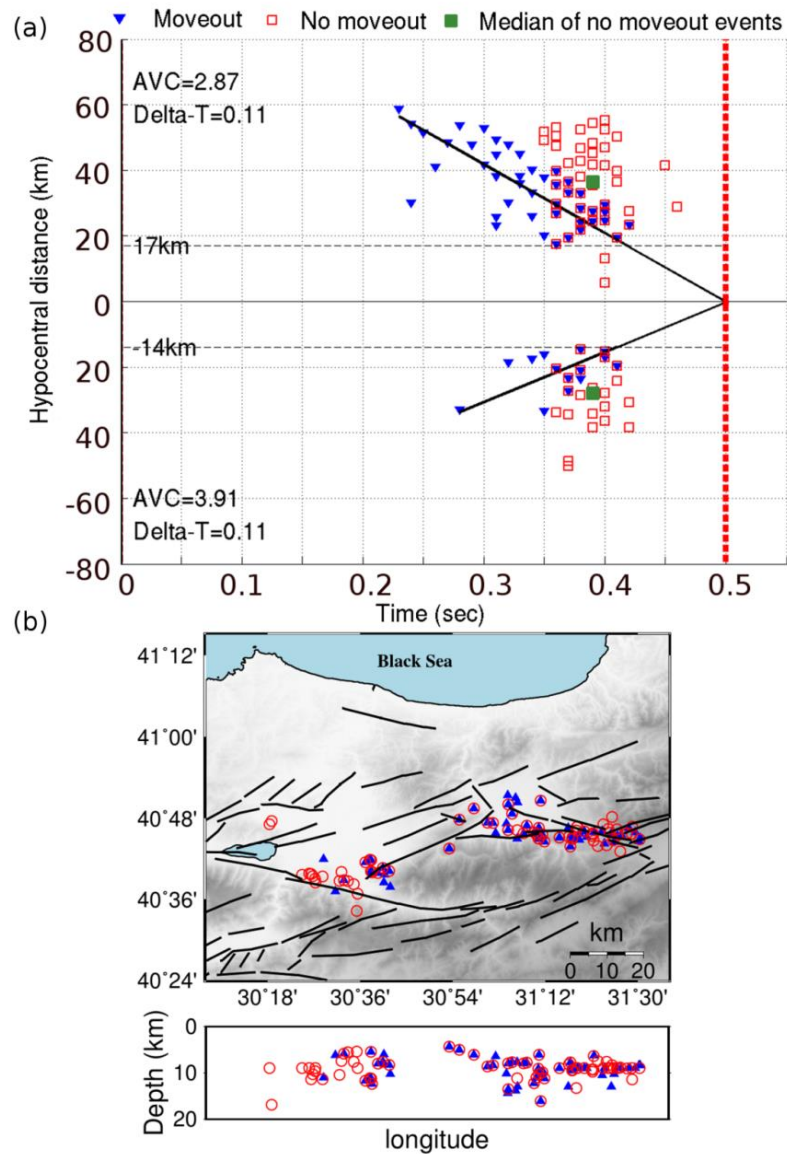


Figure 4.11. (a) A thinned set of FZHW as in Figure 4.10-a) but with picks subdivided into events showing a moveout from the direct P wave arrivals (blue filled rectangles) and events reflecting a constant differential time (no moveout, red open squares). FZHW picks with both symbols cannot be grouped clearly and thus may belong to ‘moveout’ or ‘non moveout’ producing events. The black lines show the fitted regression lines for the ‘moveout’ events to the east and west. The green filled squares show the median differential times between FZHW and direct P waves for the ‘non-moveout’ events. The calculated average velocity contrast (AVC), and differential time between FZHW and direct P waves (Delta) for the eastern and western events, respectively, are given in the figure (see text for details). The observed minimum hypocentral distance at which FZHW are observed is 17km to the east and 14 km to the west. (b) Epicentral (above) and

depth (below) distribution of the events shown in a). The moveout events are shown with filled blue rectangles and no moveout events with red circles.

For the ‘non-moveout’ group we calculate the median differential time in either direction (solid green squares). We assume that the ‘non-moveout’ FZHW arrivals are associated with the edge of a low velocity fault damage zone or trapping structure. Using in Eq. 2.2 a differential time of 0.11 s, an average P wave velocity of 5 km/s representative of the mid to shallow crust, and $\Delta\alpha$ of 50% for the velocity contrast between the damage zone and surrounding rock [e.g., *Ben-Zion et al.*, 2003; *Allam and Ben-Zion*, 2012; *Zigone et al.*, 2015], provides an estimated length scale of the local bimaterial interface of about 5.5 km. Assuming that this length has on average equal along-strike and depth components suggests that the down-dip extension of the local bimaterial interface is approximately $5.5/\sqrt{2}=3.8$ km. This is of the same order as the estimated depth values of the trapping structure and zone producing elevated fault-related-anisotropy in the area [*Ben-Zion et al.*, 2003; *Peng and Ben-Zion*, 2004]. We also observe in Figure 4.11a that a minimum propagation distance of about 15 km (14 and 17 km towards the west and east, respectively) is needed to produce ‘moveout’ FZHW in the employed stations. Using in Eq. 2.1 a distance of 15 km and $\Delta\alpha$ of 3.4% suggests that the average distance between stations FI, MO, WF, FP and VO from the deep bimaterial interface is about 4.0 km.

4.4. Discussion and Conclusions

We analyze about 100,000 waveforms recorded by seven stations located within and around the damage zone of the Karadere fault at the eastern portion of the 1999 Izmit rupture between the Akyazi and Düzce Basins (Figure 4.1). Applying a fully automated recent procedure for identification and picking of Fault Zone Head Waves and direct P arrivals [*Ross and Ben-Zion*, 2014] results in about 3,300 waveforms with two clear separate phases in the early waveforms. These phases are assumed initially to be FZHW followed by direct P arrival. Manually revising the automatic picks using particle motion analysis [*Bulut et al.*, 2012a; *Allam et al.*, 2014], we find that a substantial subset of these waveforms have first arriving direct P wave (particle motion pointing approximately to the source) followed by a phase that is reflected from a fault interface (particle motion pointing approximately to the fault normal). These secondary phases are labeled Fault Zone Reflected Waves. After the

manual analysis and application of strict quality criteria, we are left with 187 high quality FZHW picks and 215 high quality FZRW picks.

The tight network configuration with some stations within the fault damage zone allows us to distinguish between two types of FZHW propagating along different bimaterial interfaces in the fault zone structure. The first more-commonly observed type of FZHW have a systematic moveout from the direct P phases (increasing delay times between the head and direct P waves) with increasing propagation distance along the fault. These FZHW are associated with a large-scale bimaterial interface that extends to the bottom of the seismogenic zone and is continuous along strike for tens of kilometers [e.g., *Ben-Zion and Malin, 1991; Allam et al., 2014*]. The second type of FZHW have no moveout from the direct P waves (approximately constant delay times) with increasing hypocentral distance and are associated with a shallow local bimaterial interface. Such FZHW have been reported only recently in the context of the Garzê–Yushu fault in the Tibetan Plateau [*Yang et al., 2015*] and the San Jacinto fault zone in southern California [*Qiu et al., 2015*].

Observing FZHW from a deep bimaterial fault interface is best done with stations that are ~5 km away from the fault on the slow side, to avoid effects associated with the local damage structure [e.g., *McGuire and Ben-Zion, 2005*]. In the present study, stations MO and VO are located within (or very close to) the trapping structure of the Karadere fault [*Ben-Zion et al., 2003*] and are affected primarily by the shallow local bimaterial interfaces of the damage zone. Station WF also records primarily ‘non-moveout’ FZHW, suggesting it is located within a relatively broad damage zone [e.g., *Peng and Ben-Zion, 2004; Hamiel and Fialko, 2007*] that extends somewhat to the Almacik block. Stations FP and FI both record ample ‘moveout’ and ‘non-moveout’ FZHW, as well as ample FZRW, suggesting they are on the slow crustal block near the core damage zone. Stations GE and BV record essentially only FZRW. This suggests that station GE is too far from the deep bimaterial interface (outside x_c of Eq. 2.1), station BV is on the faster velocity block, and that both stations are not close to the edge of a significant broad damage zone that may produce ‘non-moveout’ FZHW.

Given the relatively large uncertainties in earthquake locations, we combine all the ‘moveout’ FZHW and calculate an average velocity contrast across the Karadere fault at depth. Using Eq. 2.2 and assuming an average velocity of 6 km/s, the average velocity contrast east and west of the stations are estimated to be about 2.87% and 3.91%, respectively in the top 15-18 km. The fact that events down to 18 km depth produce FZHW

with large moveout indicates that the deep bimaterial interface extends down to the base of the seismogenic crust. The velocity contrast typically decreases with depth [Ben-Zion *et al.*, 1992; Lewis *et al.*, 2007], so the average velocity contrast in the top 7.5-10 km is expected to be larger than the reported values. The obtained $\sim 3.4\% \pm 0.3\%$ average velocity contrast across the fault is somewhat lower than most values observed for other transform faults such as the San Andreas Fault at Parkfield (4-10%, Ben-Zion and Malin, [1991]; Zhao *et al.* [2010]) and south of Hollister (10-20%, McGuire and Ben-Zion, [2005]; Lewis *et al.* [2007]), the Hayward fault (3-8%, Allam *et al.* [2014]), the eastern California shear zone (15%, Hough *et al.*, [1994]), the Garzê–Yushu fault (5-8%, Yang *et al.*, [2015]) and the Sapanca/Mudurnu segment of the NAFZ (6%, Bulut *et al.* [2012a]).

The lower contrast for the Karadere fault than the Sapanca/Mudurnu segment [Bulut *et al.*, 2012a] may reflect the fact that it is one of two NAFZ branches (Figure 4.1), and thus presumably has less offset, compared to the single major fault in the Sapanca area further to the west. The derived relatively low velocity contrast for the Karadere fault may also be associated in part with the average analysis done jointly for all stations. The relatively low velocity contrast also means that during the particle motion analysis, we could have kept candidate FZHWs with smaller amount of rotation, which would have produced larger amount of fault zone phases. Our relatively stringent criterion of $> 50^\circ$ led to a smaller but presumably higher quality data set. We note that a reduction of the velocity contrast along the NAFZ at the Karadere fault may have contributed to the arrest of the 1999 Izmit rupture in that area. This is because the dynamic reduction of normal stress along a bimaterial interface increases with increasing velocity contrast up to about 30-40% contrast of *S* wave velocities [e.g., Ben-Zion and Andrews, 1998; Ranjith and Rice, 2001]. Thus, if the velocity contrast is larger to the west, the Izmit rupture encountered during propagation to the east an increasing frictional strength, due to the diminishing dynamic reduction of normal stress associated with the decreasing velocity contrast. Repeating rupture arrests along the Karadere fault can contribute to the development of a significant damage zone.

Combining all ‘non moveout’ phases in Figure 4.10, the mean differential time between the FZHW and direct P waves associated with these data is about 0.11 ± 0.02 sec. We note that the ‘non moveout’ type of FZHW are observed at stations on both sides of the mapped Karadere fault, in contrast to the more typical ‘moveout’ type FZHW that exist only on the slower crustal block. This suggests that the shallow low velocity body generating the ‘non moveout’ FZHW exists on both sides of the Karadere fault as shown schematically in

Figure 4.12a. Given the close proximity of the stations to the fault, the low velocity zone may represent as mentioned highly fractured damaged rocks. Using the average time delay of the ‘non moveout’ phases together with an average P wave velocity of 5 km/s for the mid to shallow crust, the depth extent of the bimaterial interface at the edge of the low velocity zone is estimated to be about 3.8 km. Alternatively, using 0.09 sec instead of 0.11 sec for the mean differential time between the FZHW and direct P waves, along with an average P wave velocity of 4.7 km/s instead of 5 km/s and 30% velocity contrast between the damage zone and surrounding rock instead of 50%, lead to a depth of 4.7 km. These values are similar to the estimated depth values of the trapping and anisotropic fault structures in the area [Ben-Zion et al., 2003; Peng and Ben-Zion, 2004], lending support to the interpretation of this rock body as damaged fault zone layer.

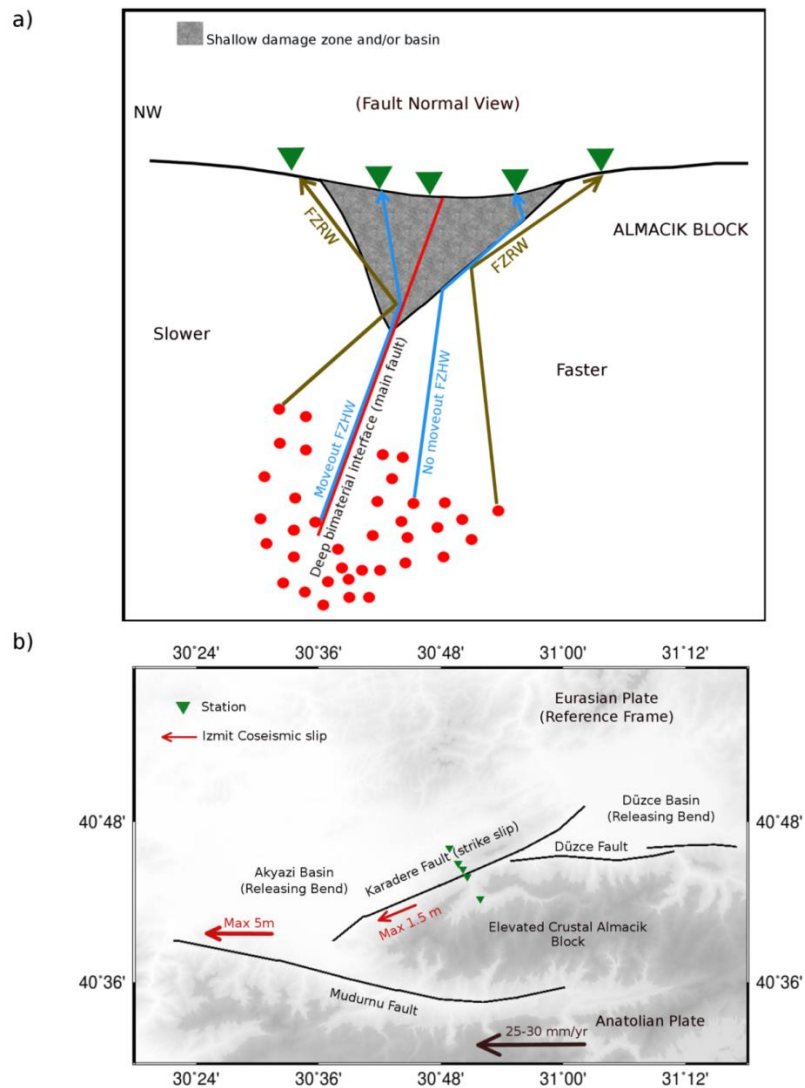


Figure 4.12. A conceptual model in (a) fault-normal and (b) map views. (a) A deep bimaterial interface marked with the oblique red line separates the fast Almacik block at the south (right) from the slower

northern side (left). A shallow damage zone or basin is shown in gray. Earthquakes are represented in red circles and two groups of rays, FZRW in dark green and FZHW in blue, reach various stations (green triangles). FZHW propagating along the deep bimaterial interface (main Karadere fault) produce moveout from the direct P waves with increasing hypocentral distance, while FZHW propagating along the shallow interface between the damage zone and the surrounding rocks represent FZHW with no moveout. Additional possible rays of FZRW and 'no moveout' FZHW propagating partially or fully through the damage zone are not shown to reduce clutter. (b) Stations are projected on a line across the Karadere fault to illustrate the various phases plotted in Fig 4.10 and Fig 4.11. The red arrows indicate maximum Izmit coseismic slip values and the black arrow indicates the GPS-derived horizontal velocity field with respect to stable Eurasia in the North.

The broader scale shallow low velocity zone seen by station WF may represent an evolving basin structure related to a progression of the two transtensional features at either end of the Karadere fault, the Akyazi Basin in the SW and the Düzce Basin in the NE (Figure 4.12b). In that case the Karadere fault, while still being dominated by right-lateral strike slip deformation as seen during the Izmit earthquake, might be in an early phase of a transition from a local strike-slip to an emerging transtensional formation linking the Akyazi and Düzce Basins. This kinematic model is supported by combined strike-slip and normal faulting mechanisms for Izmit aftershocks [Bohnhoff *et al.*, 2006] in this area. Such progressing basin development is also in accordance with observed positive isotropic source components of Izmit aftershocks [Stierle *et al.* 2014a;b] and rotations of the local stress tensor orientation [Ickrath *et al.*, 2014, 2015] in the early post-Izmit deformation in the area. However, these observations may also reflect generation of rock damage in the earthquake source volumes [e.g., Ben-Zion and Ampuero, 2009; Ross *et al.*, 2015] and a variety of fluid-related effects [e.g., Hardebeck and Hauksson, 2001; Ma *et al.*, 2012] rather than the structural evolution suggested above.

In addition to the two types of FZHW, we also identify FZRW that may provide additional information on the internal fault zone structure. However, quantitative interpretation of these waves requires accurate information on hypocenter locations and the fault geometry at depth [e.g., Li *et al.*, 2007; Yang *et al.*, 2014], and is best done with data of a linear array that crosses the fault, so is not attempted here. The detailed observations of this work highlight the existence of several types of fault zone interface waves that are recorded by stations close to large fault zones. The classical 'moveout' FZHW generated by a deep bimaterial interfaces exist only on the slower crustal block, but the 'non moveout' FZHW and the FZRW can exist generally on both sides of the main fault. These waves can

modify considerably the properties of early P waveforms recorded near faults from expectations associated with laterally-homogeneous structures. The FZHW and FZRW can be utilized to detect and quantify the seismic properties of major fault zone interfaces. As mentioned in the introduction, improved imaging of deep bimaterial and damage zone interfaces can provide important information on various topics of earthquake physics, seismotectonics and seismic hazard. At minimum, the first-arriving 'moveout' and 'non moveout' FZHW should be recognized as such, since their misidentification as direct P waves can produce biases in earthquake locations and focal mechanisms [e.g., *Oppenheimer et al.*, 1988; *McGuire and Ben-Zion*, 2005].

5. Imaging Mudurnu Segment of the North Anatolian Fault Zone from Waveforms of Small Earthquakes

Summary

We analyze waveforms of local seismicity occurring before, between, and after the two consecutive 1999 $M_w > 7$ İzmit and Düzce earthquakes in NW Turkey. The waveforms were recorded at three seismic stations located around the Mudurnu segment of the North Anatolian Fault Zone. We focus on the interpretation of two distinct secondary phases contained in the P-wave coda that are well separated from the direct P wave. The phases are produced by a structure near the stations, because they are visible at all waveforms and have a constant time delay after direct P-wave arrivals irrespective of epicentral distance, hypocentral depth, or back-azimuth. Based on a polarization analysis, the major secondary phase is a PS-converted wave. Its particle motion is consistent with the direct S wave and displays shear-wave splitting produced by the anisotropic upper crust. The particle motion of the minor secondary phase is nearly vertical and consistent with the P wave. Synthetic modeling indicates that the PS phase is converted at a horizontal interface at a depth of ~ 4 km. We discuss the role of the steep Mudurnu fault zone as a generator of the PS reflected conversions at shallow depths. This interpretation is in agreement with the near-surface setting indicating a juvenile pull-apart structure along the Mudurnu fault and fits well into the eastward progressing transtensional tectonic setting known for the region.

5.1. Introduction

Identification of down-dip extension of faults and a detailed structure of the upper crust is a key-issue in imaging the location and geometry of future ruptures. Active wide-aperture and multi-channel seismic profiling can provide such information but require substantial budgets for data acquisition and cannot image near-vertical fault planes [e.g., *Thybo et al.*, 2003; *Brückl et al.*, 2007; *Kaiser et al.*, 2009; *Yang*, 2015]. These difficulties can be overcome by studying local seismicity. Local earthquakes generate high-frequency seismic waves which can be reflected and/or converted at structural horizontal or inclined interfaces or faults representing a first-order discontinuity with a velocity contrast. Consequently, waveforms of earthquakes recorded at local seismic networks can provide information which can be utilized for imaging the velocity structure [e.g., *Sanford et al.*, 1973; *Eberhart-Phillips and Michael*, 1993; *Wu and Lees*, [1999] and as has been shown only recently also for imaging the interfaces at depths [*Hrubcová et al.*, 2013 ; 2016]. To perform this analysis, a novel concept for extracting crustal structure from high-frequency waveforms of local earthquakes was developed by *Hrubcová et al.* [2013 ; 2016] and applied for determining depth and topography of crustal discontinuities. The method was tested on two microseismic data sets allowing for imaging horizontal interfaces at the site of the Continental Super-Deep Drilling Project (KTB) in Germany and in the West Bohemia earthquake swarm region in the Czech Republic [*Hrubcová et al.*, 2016]

In this paper, we extend the technique of *Hrubcová et al.* [2013 ; 2016] to near-fault zone recordings along the North Anatolian Fault Zone (NAFZ) in northwestern Turkey and aim to image the structure around the strike-slip Mudurnu segment as a major NAFZ branch. We use local seismicity occurring before, between and after the two consecutive 1999 Mw > 7 İzmit and Düzce earthquakes [e.g., *Tibi et al.*, 2001; *Gülen et al.*, 2002] (Figure 5.1), which provide unique opportunity to study source processes in the focal zone [e.g., *Örgülü and Aktar*, 2001; *Li et al.*, 2002; *Stierle et al.* 2014a;b], local seismotectonic features [*Bohnhoff et al.*, 2006; *Bulut et al.*, 2007; *Bohnhoff et al.*, 2016a], and structural characteristics of the Mudurnu area [e.g., *Görgün et al.*, 2010; *Bulut et al.*, 2012a; *Beyhan and Alkan*, 2015]. A detail analysis of waveforms enabled us to identify secondary phases in the P-wave coda at near-fault stations and to invert them for imaging sedimentary and upper-crustal structure near the Mudurnu fault.

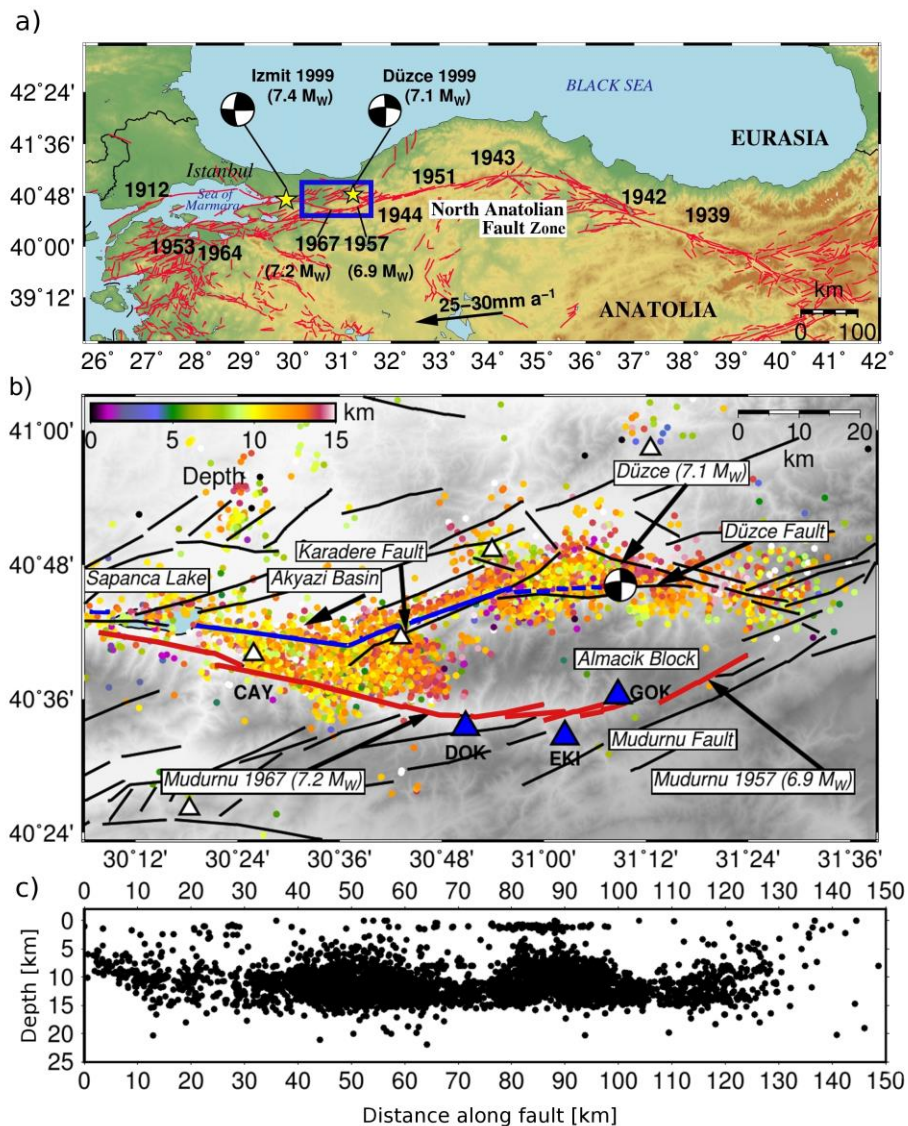


Figure 5.1. Mudurnu Fault and the seismicity studied (a) Regional tectonic setting of the northern Anatolian region with the North Anatolian Fault Zone (NAFZ) as the right-lateral transform plate boundary between Anatolia and Eurasia. The black arrow indicates the present GPS-derived average right-lateral slip along the NAFZ [after McClusky *et al.*, 2000]. Black numbers show the locations of the $M_w > 6.9$ earthquakes during the 20th century; note their westward migration with time. The 1999 İzmit and Düzce earthquakes are marked by yellow stars with corresponding focal mechanisms [after Özalaybey *et al.*, 2002]. Blue rectangle indicates the study area. (b) Study area with the Mudurnu fault (bold red line) as a major NAFZ branch that hosted large earthquakes in 1957 (M_w 6.9) and 1967 (M_w 7.1). The 1999 İzmit (blue line) and Düzce (dashed blue line) ruptures are indicated [after Barka *et al.*, 2002]. Additional NAFZ branches and nearby mapped faults are plotted by black lines. White triangles represent seismic stations of the SABONET network [Milkereit, 2000]; blue triangles stand for SABONET stations used in this study. The seismicity represents events from 1997 to 2001 as recorded by stations DOK, EKI, and GOK and is color-coded according to the hypocentral depth. The focal mechanism shows the epicenter and faulting mechanism of the Düzce earthquake. (c) Hypocentral depths of seismicity along the NAFZ section shown in (b).

5.2. Data

In this study, we use data from the seismic network SABONET (SApanca-BOLu NETwork) which consisted of 15 stations equipped with short-period seismometers of type MARK L4-3D, with a natural frequency of 1 Hz and sampled at a rate of 100 Hz [Milkereit *et al.*, 2000; Bindi *et al.*, 2007; Ickrath *et al.*, 2015]. The seismicity covered a 5 year (1997-2001) time window framing the two 1999 $M_w > 7$ İzmit and Düzce earthquakes and consisted of absolute and relocated seismic events [Ickrath *et al.*, 2015; Bohnhoff *et al.*, 2016a]. The majority of events occurred between depths of 6 and 16 km with only a small portion located near the surface (Figure 5.1). The absolute locations were improved based on a joint inversion for hypocentral parameters model from Bulut *et al.*, [2007] using selected events of the 10,000-event catalogue (see Bohnhoff *et al.* [2016a] for details).

To image the Mudurnu segment, we used seismic events located along the İzmit-Düzce rupture zone north of the Almacik block recorded at three SABONET stations EKI, DOK, and GOK distributed around the Mudurnu fault (Figure 5.1b). Each of the stations recorded about 4,000 earthquakes with magnitudes in range of 0.9-3.8. We manually revised phase onset picks and performed several processing steps to detect and characterize secondary phases recorded in the seismograms.

5.3. Data Analysis

5.3.1. Waveform Processing

In order to identify and systematically process the secondary phases in the P-wave coda, the entire seismic dataset of the earthquakes was divided according to their epicenters into 33 spatially distributed clusters. The clusters are formed by the earthquakes with either similar epicenters (a typical diameter of such clusters is about 6 km) or with a similar back-azimuth to the analyzed stations. The clusters cover the seismicity on both sides of the Karadere-Düzce fault from the west to the east. For each cluster, the waveforms were plotted with the aligned direct P-wave arrivals and sorted according to foci depths. To improve the alignment of the direct P-wave arrivals, waveforms were cross-correlated. Events with low signal to noise ratios were eliminated from the farther analysis. To enhance detection of secondary phases, the waveforms were filtered with a bandpass filter of 1-5 Hz and plotted

depth-sorted (or epicentral-distance-sorted) with equidistant step in the seismic sections. After filtering, the low frequency secondary phases were distinctly pronounced. Figure 5.2 shows the improvement in the secondary phases' detection in the seismic section after the waveform processing with filtering, alignment, hypocentral-depth sorting, and equidistant plotting.

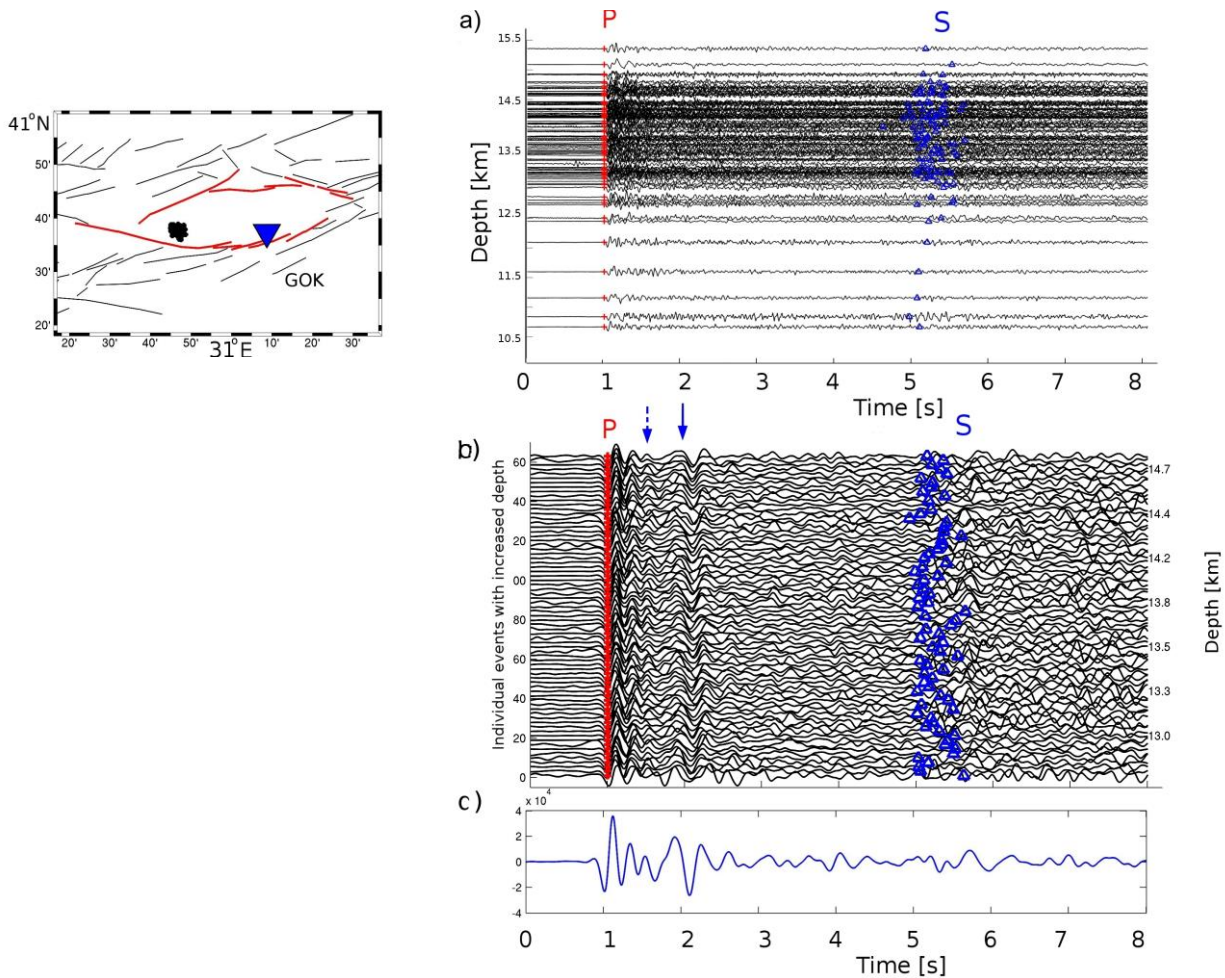


Figure 5.2. Waveform processing for enhancing detection of secondary phases in seismograms. (a) Unfiltered vertical component waveforms recorded at station GOK plotted with the P-wave alignment according to increased hypocentral depth. (b) Vertical component waveforms bandpass-filtered with 1-5 Hz, sorted according to hypocentral depth, and plotted equidistantly. The seismicity cluster is marked in the insert by black dots, the Karadere-Düzce and Mudurnu faults are color-coded in red. P-wave arrivals are marked by red crosses; S-wave arrivals are marked by blue triangles. The stacked seismogram is plotted below the section. Clear and consistent arrivals of the secondary phases after the direct P-wave are indicated by blue arrows (solid blue arrow – major, dashed blue arrow – minor secondary phase). Note the improvement in the secondary phases' detection after the waveform processing with filtering, P-wave alignment, hypocentral depth sorting, and equidistant plotting.

Such waveform processing was performed for each cluster enabling us to detect the secondary phases generated by local crustal discontinuities and to enhance their visibility in the seismic sections. A systematic processing of these time sections revealed the presence of

coherent secondary phases coming in the P-wave coda (Figure 5.2). The analysis at stations DOK, EKI, and GOK showed that the secondary phases were reasonably pronounced and well-separated from the direct P-waves at all stations (Figures 5.3 and 5.4). Noteworthy, the time difference between the secondary phases and the direct P arrivals did not change substantially within each cluster nor among clusters at each station (e.g., Figure 5.2). However, the wavefields varied substantially among the stations (see Figures 5.3 and 5.4).

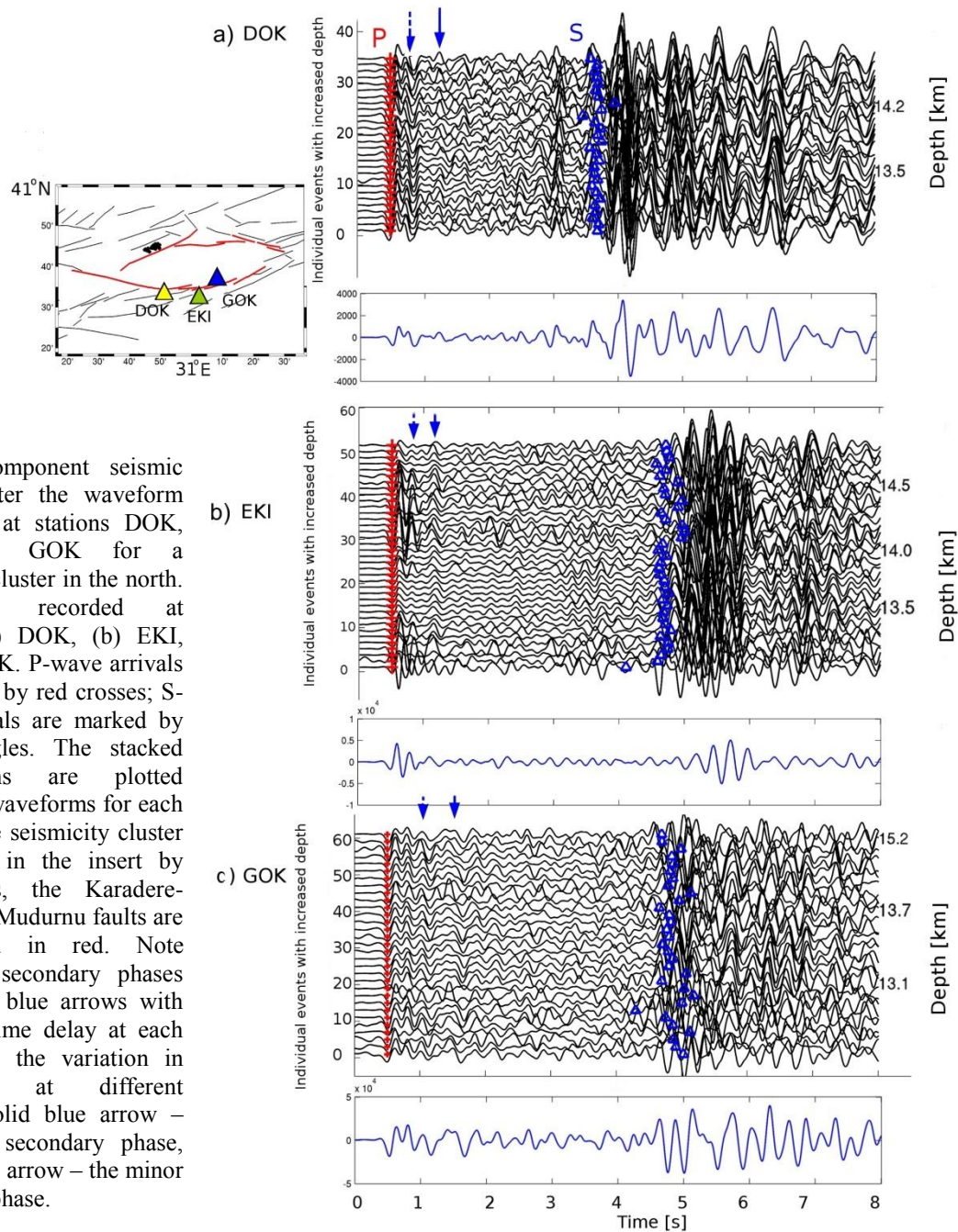


Figure 5.3. Vertical component seismic sections after the waveform processing at stations DOK, EKI, and GOK for a seismicity cluster in the north. Waveforms recorded at stations (a) DOK, (b) EKI, and (c) GOK. P-wave arrivals are marked by red crosses; S-wave arrivals are marked by blue triangles. The stacked seismograms are plotted below the waveforms for each station. The seismicity cluster is marked in the insert by black dots, the Karadere-Düzce and Mudurnu faults are color-coded in red. Note prominent secondary phases marked by blue arrows with the same time delay at each station and the variation in wavefields at different stations. Solid blue arrow – the major secondary phase, dashed blue arrow – the minor secondary phase.

The recordings at stations DOK and EKI showed generally less pronounced and less consistent arrivals of the secondary phases than the recordings at station GOK. Also, the time delay in the arrival times between direct P waves and the secondary phases varied for each station (see Figures 5.3 and 5.4).

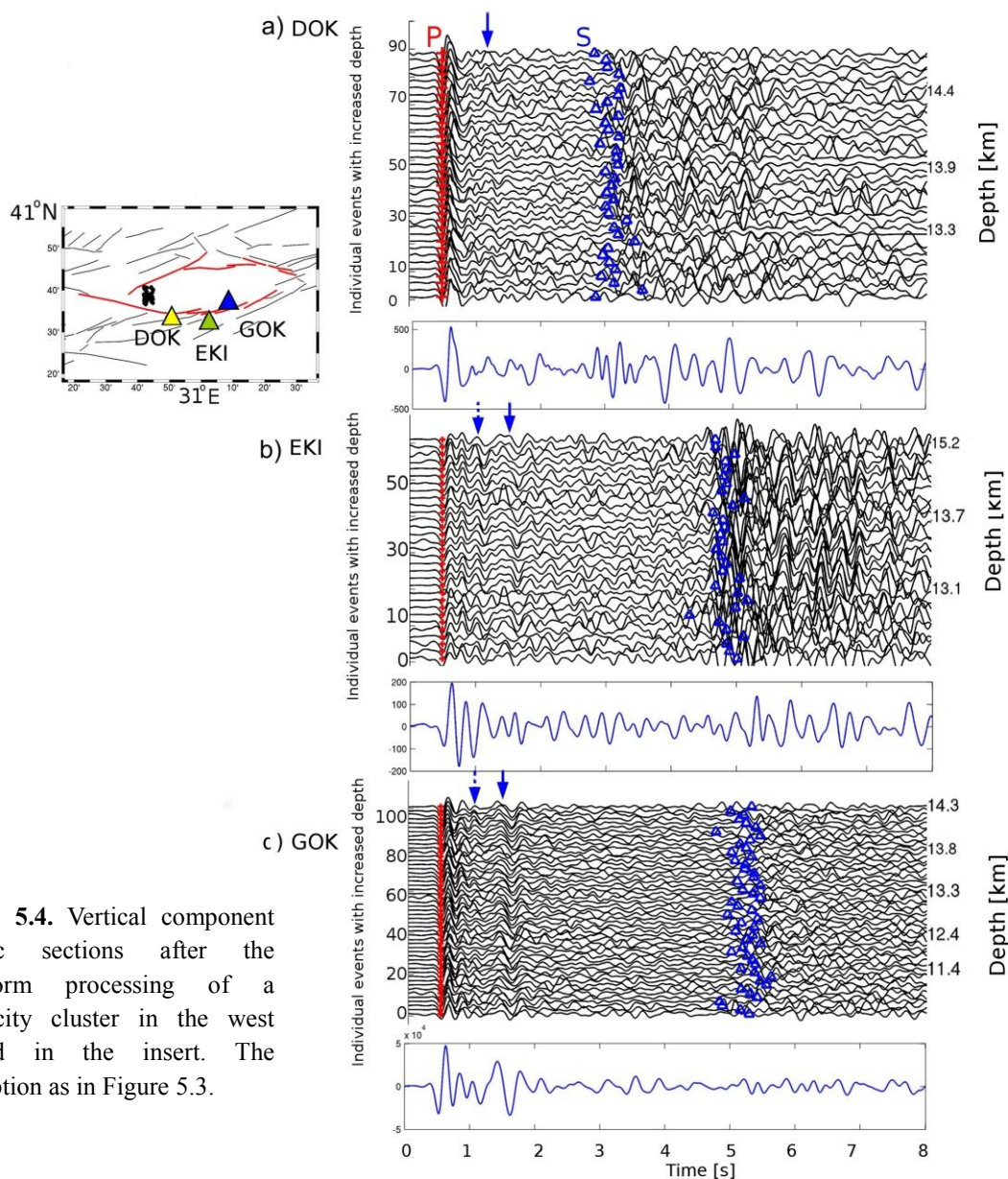


Figure 5.4. Vertical component seismic sections after the waveform processing of a seismicity cluster in the west marked in the insert. The description as in Figure 5.3.

Station DOK exhibited consistent onsets of secondary phases at 0.7 s after the P-wave first arrival, some of the sections from northern clusters showed also pronounced high-amplitude onsets of secondary phases at 0.2 s after the P wave and the high-amplitude phases before the S waves (see Figure 5.3a). Station EKI showed coherent secondary phases at 0.5 s, some clusters exhibited also onsets at 0.2 s and 0.8 s (see Figure 5.3b and 5.4b). The time

difference of the secondary phases at station GOK was 0.9 s, and almost all clusters also showed a preceding secondary phase at 0.5 s (Figure 5.3c and 5.4c).

Constant time difference of the secondary phases after the direct P-wave arrivals and variations in the arrival times and amplitudes of the secondary phases observed for individual stations express variations in local structure near the respective station. Since the recordings at station GOK showed the most prominent and consistent secondary phases well separated from the direct P wave for most of the clusters, in our analysis we focused on this station.

5.3.2. Epicentral and Depth Sorting Complemented by Azimuthal Analysis

To analyze the nature and origin of the secondary phases, we aim at studying in detail the difference in the arrival times of the direct P and the secondary phases (hereinafter the time delays) at station GOK.

First, we compared the time delays in depth-sorted sections of traces for clusters in different azimuths (Figure 5.5). Since we are interested in structural features generating the secondary phases, we intended to avoid the effect of focal mechanisms and subsequent variations in the first-motion polarity in the recorded waveforms. Therefore, we flip some of the waveforms to get the same first-motion polarity on all vertical recordings in each cluster. This was applied mainly to the recordings of the northern and eastern clusters, which resulted in an increased consistency of waveforms and in a higher visibility of the secondary phases in the seismic sections. As a result, clear secondary phase appears consistently in seismic sections of almost all clusters (see Figure 5.5a and c). The arrival times of this secondary phase with respect to the direct P wave is the same disregarding the cluster locations and at station GOK attains a value of 0.9 s (with minor fluctuation of 0.05 s). Some clusters at this station show also another preceding secondary phase at 0.5 s after the P wave, though its amplitude is smaller and less consistent (Figure 5.5).

Second, to confirm constant time delay between the P wave and the secondary phase, we sorted the waveforms according to their epicentral distance. In this case, the seismicity was separated into 36 azimuthally variable segments covering the whole seismicity. For each segment, waveforms were sorted according to epicentral distance in a narrow azimuthal range and plotted with the direct P-wave alignment. Figure 5.6 shows an example of seismic section for one epicentral-distance-sorted cluster located in the west. The figure indicates that

the alignment does not exhibit any moveout of the secondary phase with the increasing epicentral distance, similarly as for the depth sorting.

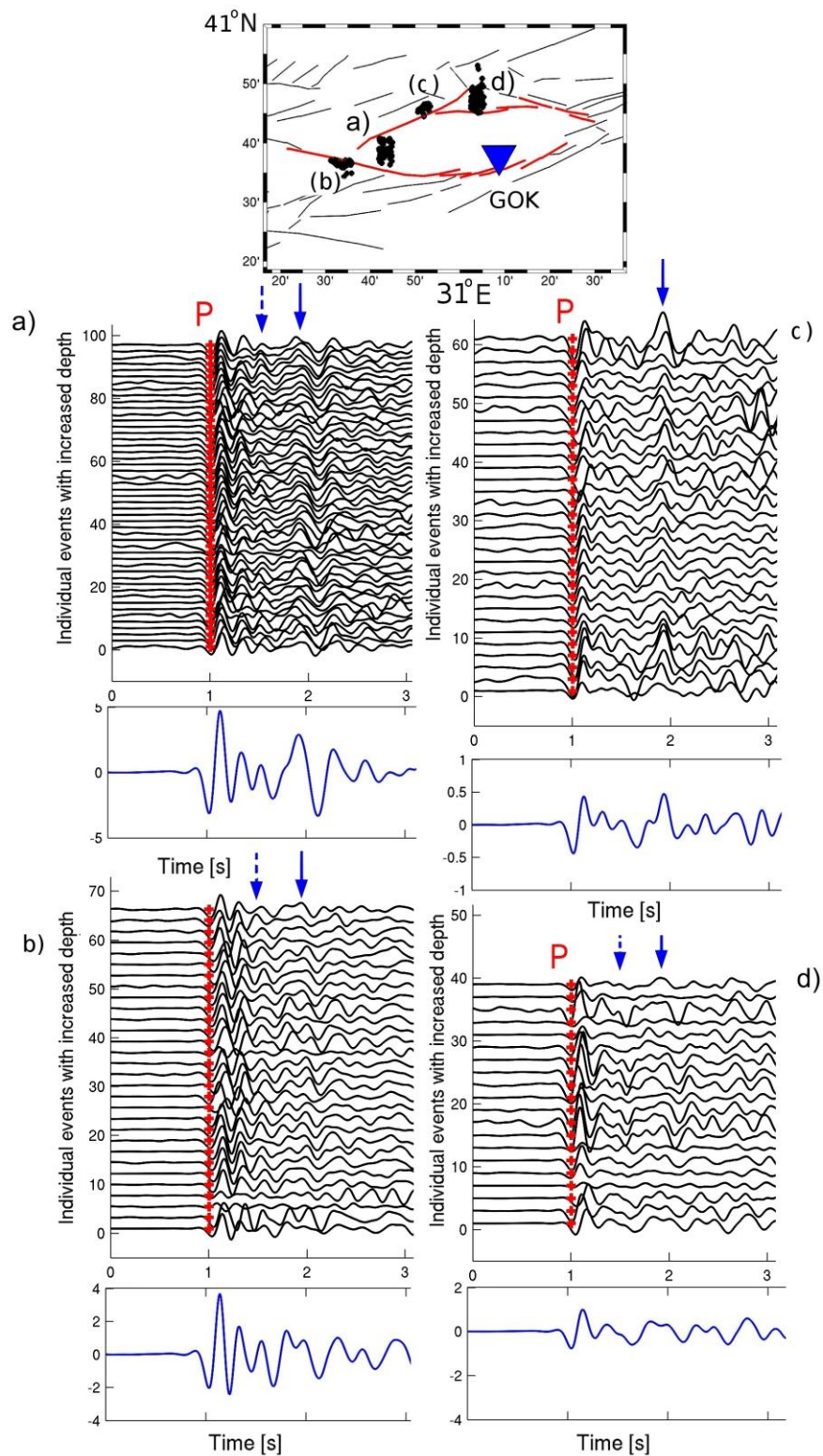


Figure 5.5. (a-d) Vertical component seismic sections after the waveform processing at station GOK at different azimuths. The stacked seismograms are presented beneath each seismic section. P-wave arrivals are marked by red crosses; blue arrows indicate the secondary phases (solid blue arrow – the major secondary phase, dashed blue arrow – the minor secondary phase). The seismicity clusters (a-d) are marked in the insert by black dots,

the Karadere-Düzce and Mudurnu faults are color-coded in red. Note the same time delay of the secondary phases after the P waves for all clusters.

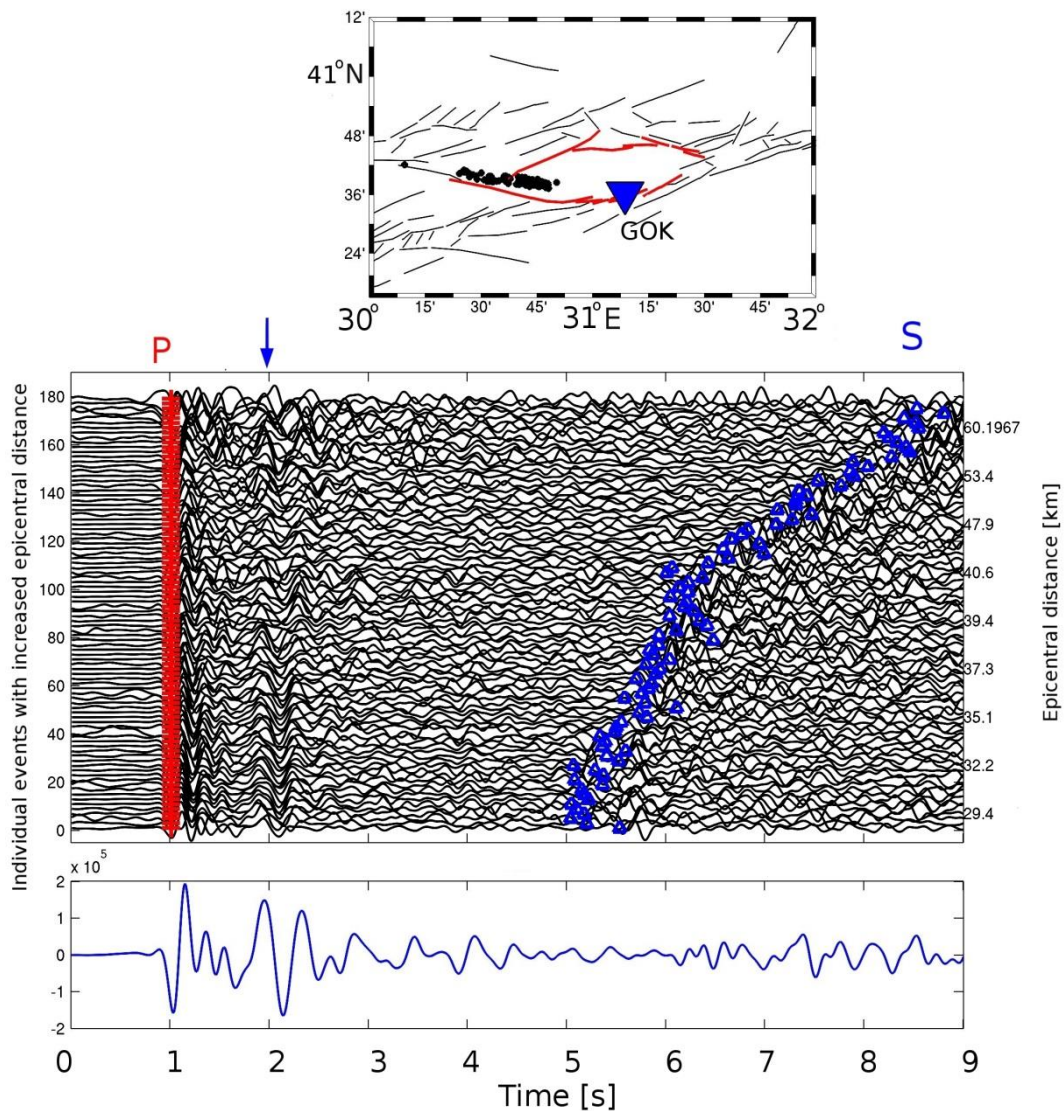


Figure 5.6. Vertical component seismic section after the waveform processing at station GOK plotted according to the increased epicentral distance. The stacked seismogram is presented beneath the section; note the comparable amplitudes of the secondary phase and the P wave. The seismicity cluster is marked in the insert by black dots, the Karadere-Düzce and Mudurnu faults are color-coded in red. P-wave arrivals are marked by red crosses; S-wave arrivals are marked by blue triangles; blue arrow indicates the secondary phases. Note the consistent time delay of the secondary phases after the P waves despite the increase of epicentral distance.

5.3.3. Detected Secondary Phases

All clusters exhibit a consistent time delay between the P wave and the secondary phase both in depth and epicentral-distance sorting. However, the character of the wavefield differs for clusters from the west to the east. The secondary phases in the recordings from the

western and northern clusters are more prominent compared to the recordings from the eastern clusters. Further to the east, the waveforms are noisier and less consistent within each cluster, which made the detection of the secondary phase more difficult (see Figure 5.7). The observations of less and more visible secondary phase in the seismic sections are consistent for all three stations and can be attributed to variations in radiation patterns of the earthquakes and to lateral inhomogeneities in the area.

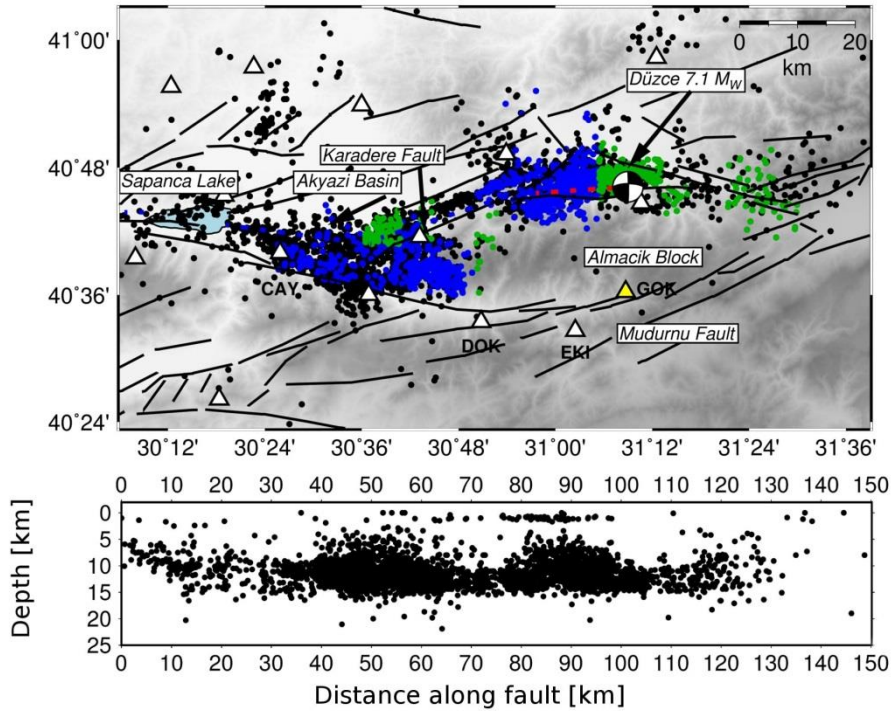


Figure 5.7. Seismicity along the Karadere-Düzce and partly Mudurnu faults with the events recorded at station GOK during 1997-2001. The events are color-coded according to the amplitudes and consistency of the secondary phases observed in the waveforms after processing: seismicity with well consistent secondary phases is marked in blue; seismicity with less consistent secondary phases is marked in green.

5.3.4. Particle Motion Analysis

The secondary phases in the P-wave coda are usually generated at a subsurface structure. They can be of P- or S-type being reflected or converted at subsurface layers. The type of the phases can be identified using the polarization analysis of the 3D particle motions. Therefore, in addition to analyzing seismic sections of vertical components of waveforms in each cluster recorded at station GOK, we included the horizontal components and analyzed the polarization of the P, S, and the secondary waves for all waveforms within each cluster (Figure 5.8).

The P-wave onsets are characterized by a nearly vertical polarization in the direction of back-azimuths. The S waves are polarized horizontally in the NW-SE direction (or perpendicularly to this direction), irrespective of the back-azimuth and are in agreement with the results of the shear-wave splitting analysis performed by *Hurd and Bohnhoff*, [2012].

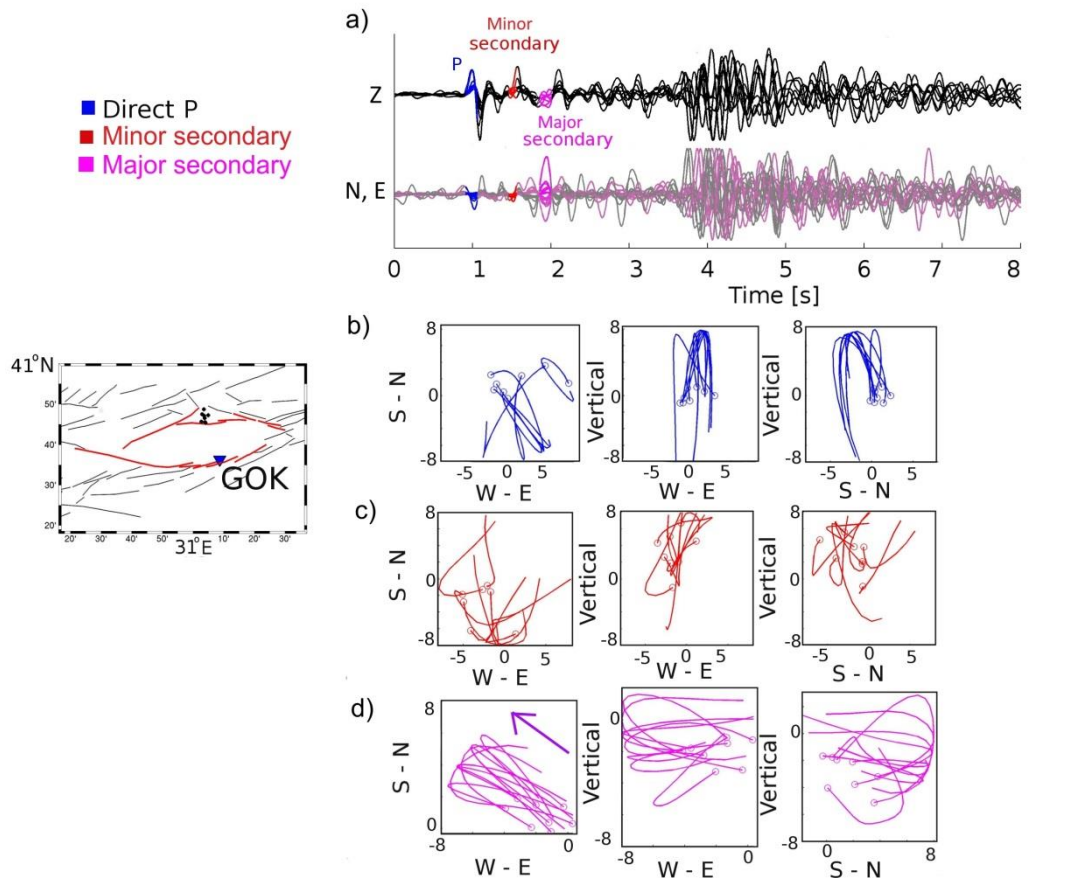


Figure 5.8. Particle motion analysis. (a) Three component waveforms recorded at station GOK. The seismicity cluster is marked in the insert by black dots; the Karadere-Düzce and Mudurnu faults are color-coded in red; the fast shear-wave polarization of the NW-SE direction is marked by violet arrow. The P waves (blue), major (pink), and minor (red) secondary phases are color-coded. (b-d) Particle motion plots for the P wave (b), major (c), and minor (d) secondary phases in the EW-SN (left), EW-Z (middle) and SN-Z (right) projections with colors as in a). Note the polarization of the major secondary phases (marked in pink) corresponding to the S-type phase being horizontal in the vertical projections; its concordant direction with the fast shear-wave axis (marked by purple arrow in the EW-SN projection, after *Hurd et al.* [2012]) indicates the influence by the anisotropy. The polarization of the minor secondary phase (marked in red) corresponds to the P-type phase being vertical or near vertical.

Apart from the P- and S-wave onsets, we concentrated on the polarization of the most prominent secondary phase at ~ 0.9 s after the P wave (major secondary phase). The particle motions of this phase exhibit a horizontal polarization in the NW-SE direction (and perpendicular) independent of the cluster locations being thus consistent with the directions

of the shear-wave splitting observed in the area [Hurd and Bohnhoff, 2012; Peng and Ben-Zion, 2004]. This indicates that the major secondary phase is a S-type phase (Figure 5.8d) being influenced by anisotropy of the upper crust [Hurd and Bohnhoff, 2012]. Therefore, we conclude that this phase is probably the PS phase converted at a shallow crustal structure.

In the next step, the lower-amplitude and less visible secondary phase detected at 0.5 s after the P wave (minor secondary phase) was analyzed in the seismic sections of some clusters. The particle motion of this phase shows a near vertical polarization corresponding to a P-type phase (Figure 5.8c). Therefore, the P-wave type secondary phase is probably the PPP reflected wave generated by a shallow subsurface layer. Variations in the incidence angle of the minor secondary phase and the direct P wave on the EW-NS plane for some clusters, however, do not exclude the possibility that the minor secondary phases are produced by reflections from a rather near-vertical structure (e.g., the Mudurnu fault).

5.4. Synthetics and Interpretation

Based on low frequency content and the polarization, the major secondary phase is likely the PS conversion of the direct P wave. Since the time delay of this phase does not change substantially with the epicentral distance of the analyzed clusters, the conversion point must be close to the station.

To evidence the origin of such PS phase, two possible scenarios were considered: (1) a near-horizontal converting interface and (2) a steep inclined interface as a converting reflector. Both scenarios are plausible because geological structure is complicated in the area where the NAFZ is separated into two branches, the Mudurnu and Karadere-Düzce faults. These faults delimit the whole-crustal high-velocity Almacik Block with velocities of 6 km s⁻¹ surrounded by lower crustal velocities of 5 km s⁻¹ as studied by Papaleo *et al.*, [2017] further to the west. To simulate the observed data, we applied real source-receiver geometry for station GOK, tested various focal mechanisms and simulated the sources of depth-sorted as well as epicentral-distance-sorted seismicity. Synthetic tests were performed for a simple velocity model consisted of two layers with velocities of 6 km s⁻¹ simulating structures of the Almacik Block and 5 km s⁻¹ representing crustal velocities in its vicinity. The pronounced discontinuity of 1 km s⁻¹ was assumed at varying depth and the goal was to find

the optimum depth for which the PS wave is separated from the P wave with the observed time delay of ~ 0.9 s.

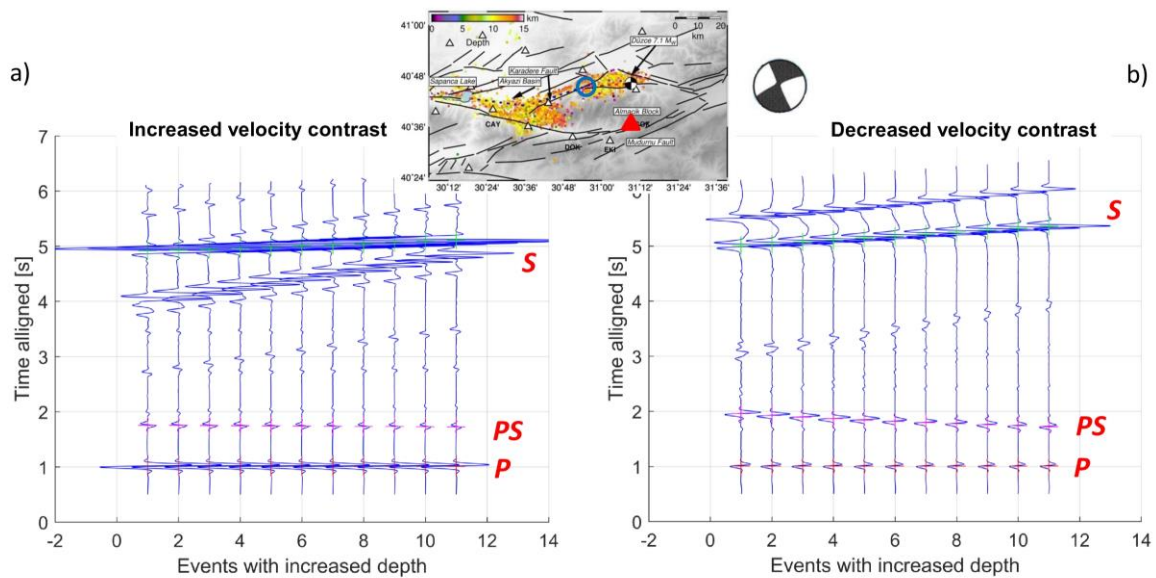


Figure 5.9. Vertical component synthetic sections for the depth-sorted seismicity at station GOK with two velocity contrasts at a horizontal interface. The seismicity cluster in the north is indicated in the insert, focal mechanisms applied after *Stierle et al.*, [2014b] (mechanism 33 interpreted for this location), filtered 1-10 Hz. (a) Positive velocity contrast with the downward velocity increased from 5 to 6 km s⁻¹ at the depth of 4 km. Note the constant time delay of the PS phase after the P wave. (b) Reverse velocity contrast with the downward velocity decreased from 6 to 5 km s⁻¹ at the depth of 3 km. Note the higher amplitude of the PS phase, though its time delay is not exactly constant.

For the horizontal converting interface, the synthetic waveforms were calculated by the discrete wavenumber approach [*Bouchon*, 1981]. Figure 5.9 documents the PS phase for 11 events located at a depth range of 10-15 km with a focal mechanism after *Stierle et al.*, [2014b] (Table 3, mechanism 33) for one northern depth-sorted cluster. Figure 5.9a presents the velocity contrast with the downward velocity increased from 5 to 6 km s⁻¹ at the depth of 4 km. The PS phase is at 0.9 s after the P wave and exhibits a constant time delay for all events. Figure 5.9b shows a reverse velocity contrast with the downward velocity decreased from 6 to 5 km s⁻¹ at the depth of 3 km. In this case, the PS phase is more pronounced; however, the PS arrival time after the P wave slightly varies with the depths of events.

To simulate the epicentral-distance-sorted seismic sections, we calculated synthetic waveforms for 13 events located at epicentral range of 30-60 km at the depth of 11.5 km; the focal mechanism was applied after *Stierle et al.*, [2014b] (Table 3, mechanism 16). Figure 5.10 shows the results for the horizontal interface with a velocity contrast from velocity of 5 to 6 km s⁻¹ at the depth of 4 km. As for the depth-sorted seismicity, the synthetic section

exhibits constant time delay of the PS phase after the P wave which agrees with the observed data.

For a steeply inclined interface, we simulated the Mudurnu fault zone located close to station GOK as the PS reflecting convertor. We tested the velocity contrast from 5 to 6 km s⁻¹ on both sides of the interface and its inclination. The 2D structure was modeled by using the ray-tracing program package SEIS83 [Červený and Pšenčík, 1984].

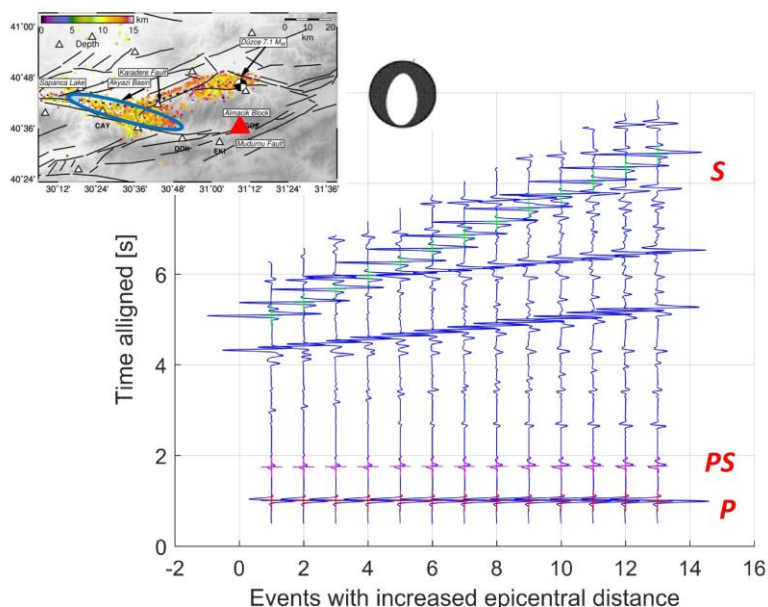
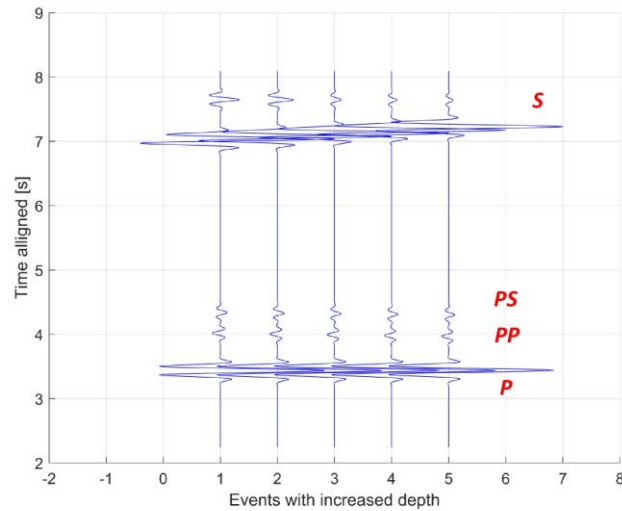


Figure 5.10. Vertical component synthetic section for the epicentral-sorted seismicity at station GOK for a horizontal interface. The seismicity cluster in the west is indicated in the insert, the focal mechanisms applied after *Stierle et al.*, [2014b] (mechanism 16 interpreted for this location), filtered with 1-10 Hz. The velocity contrast is positive with the downward velocity increased from 5 to 6 km s⁻¹ at the depth of 4 km. Note the constant time delay of the PS phase after the P wave.

The synthetic waveforms were calculated for events located at a depth range of 10.5-14.5 km simulating the same northern cluster as in the case of the model with the horizontal interface. The waveforms for a model with the inclined interface are more complex. The inclined interface produces not only the PS reflected conversions but also the P-to-P (PP) reflections from the same discontinuity. In addition, the tests show that the time delay of the PS phase is constant for both velocity contrasts (Figure 5.11). The PS amplitude depends on the incidence angle of the impinging rays at the interface and it is rather small for steeply inclined interfaces. Also, the preceded PP reflection from the same interface has comparably small amplitudes. Less inclined interfaces produce critical and over-critical PS rays with higher amplitudes. In this case, the amplitudes of the PP reflections are also overcritical, and

thus high and dominant in the waveforms. The impinging rays touch the interface at shallow depths of ~2-3 km.

Figure 5.11. Vertical component synthetic section for the depth-sorted seismicity at station GOK for an inclined interface. The seismicity cluster and focal mechanisms as in Figure 5.9; filtered 1-10 Hz. The velocity contrast is from 5 to 6 km s⁻¹. Note the constant time delay of the PS phase after the P wave together with the existence of the PP phase.



5.5. Discussion and Conclusions

We analyzed ~4,000 earthquakes recorded at three stations of the SABONET network located around the Mudurnu segment of the NAFZ in the NW Turkey. The earthquakes are located along the İzmit-Düzce rupture zone of the NAFZ north of the Almacik block and recorded at stations EKI, DOK, and GOK (Figure 5.1). We focused on the interpretation of the secondary phases in the P-wave coda well separated from the direct P wave. The analyzed earthquakes were sorted into clusters covering the entire seismically active zone. In order to reliably detect the secondary phases in the waveforms, the waveform processing consisted of the following steps:

- low-frequency filtering (1-5 Hz) to enhance the signal-to-noise ratio for the secondary phases,
- P-wave alignment of traces based on waveform cross-correlation,
- polarity flipping of some traces to obtain uniform P-wave polarities for all traces and to suppress azimuthal dependence of body-wave polarity on focal mechanisms,
- epicentral-distance and depth sorting,
- equidistant plotting in seismic sections.

The waveform processing was further supported by the particle motion analysis to recognize the type of the secondary phases.

The analysis revealed prominent secondary phases in recordings of all studied stations with a constant time delay after direct P-wave arrivals. The time delay of the major secondary phases is independent of the location and depth of the earthquakes, especially at station GOK. Polarization analysis performed for high-quality recordings of station GOK suggests two types of the secondary phases. The major phase is a PS conversion with the time delay of ~ 0.9 s after the direct P-wave onset. Its polarization is consistent with the direct S wave, which displays the shear-wave splitting produced by the anisotropic upper crust in the area observed by *Hurd and Bohnhoff*, [2012]. The minor secondary phase is less consistent within the clusters and has smaller amplitudes. It is detected at ~ 0.5 s after the P-wave onsets and its vertical polarization indicates a P-type phase.

In synthetic tests, we concentrated on modeling of the most prominent PS phase. Since the time delay of this phase does not change substantially for the analyzed clusters, it should be generated at a structure near the station. The time delay of ~ 0.9 s is fitted by a velocity model with a horizontal interface at the depth of 4 km with the downward increased velocities. The minor P-type phase preceding the PS conversion can be simulated by a PPP phase reflected from an uppermost discontinuity beneath the station. By nature, this triple P phase arrives at a station with the same time delay after the P wave for all events irrespective of their depths and epicentral distances [*Hrubcová et al.*, 2016]. Assuming the P-wave velocity to be in a range of ~ 3.2 - 3.8 km s⁻¹ in the subsurface layer, the time delay of 0.5 s between the P and PPP phases indicates the bottom of this layer at ~ 800 - 900 m. This agrees with a low-velocity weathered layer of hard rocks exposed at the surface as reported for many other areas by, e.g., *Vavryčuk et al.* [2004]. The velocity model with horizontal layers is quite common in crustal studies [e.g., *Kennett et al.*, 1995; *Hrubcová et al.*, 2016], and represents the most robust solution for the systematically observed PS conversions in our interpretation.

Alternatively, a steeply inclined interface reflecting the geological setting of the Mudurnu fault with a higher velocity at its southern side as observed further to the west [*Bulut et al.*, 2012a] can be considered. This model produces also the PS conversions with a roughly constant time delay after the P-wave arrival. The amplitude of this PS is, however,

rather small. On the other hand, this model predicts the PP reflections preceding the PS phase which is generated at the same interface.

Figure 5.12a presents a schematic sketch with the horizontal interface producing the PS phase combined with a shallow layer producing the triple P reflected phase preceding the PS conversions. Figure 5.12b presents a schematic sketch with a steeply inclined reflecting/converting interface (or fault zone) producing both major PS reflected conversions and minor PP reflections.

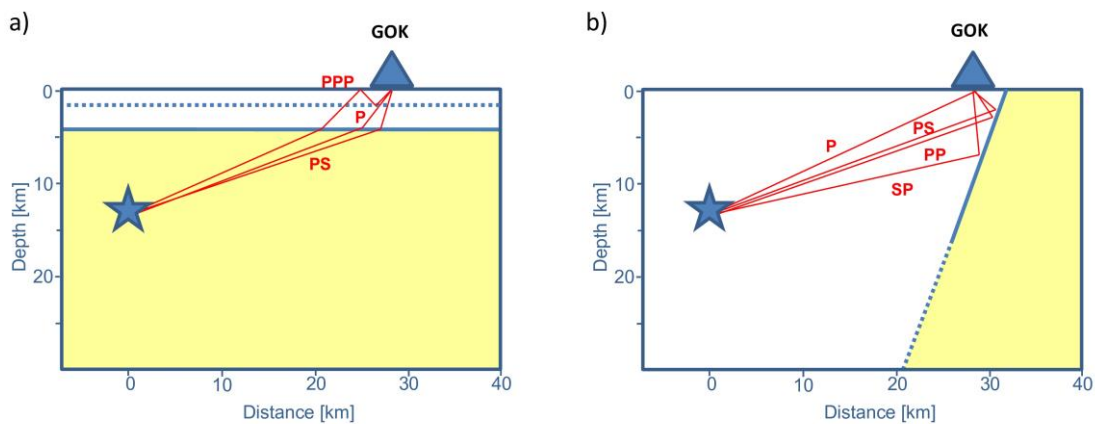


Figure 5.12. (a) Schematic sketch with the horizontal interface producing the PS phase combined with the shallow layer producing triple P reflected phase. (b) Schematic sketch with a steeply inclined reflecting/converting interface (or fault zone) producing both major PS reflected conversions and minor PP reflections. The rays are indicated by red lines; the interfaces are indicated by blue lines.

Unfortunately, the analysis of the particle motions of the direct and the secondary phases does not help us to further discriminate between the two models. Because of anisotropy in the upper crust both direct and converted S phases are affected by shear-wave splitting, which poses limitations on the interface identification. In addition, the minor P-type secondary phase is noisy and it is difficult to resolve whether it is produced by the horizontal layered or steeply inclined structure. Thus, a horizontal interface at ~ 4 km depth is the most plausible origin of the PS conversions systematically observed in the Mudurnu data. Its effect can be enhanced by the proximity of steep Mudurnu fault zone as a generator of the PS reflected conversions at shallow depths of ~ 2 -3 km.

To conclude we can state that both, a horizontal interface (the most robust solution in crustal studies) as well as a steeply inclined interface (which also explains the observed secondary phases and is known to exist as the Mudurnu fault) can explain our observations. Probably in fact, both such structures are present along the Mudurnu fault finally resulting in the clear secondary phases observed at the studied seismograms.

Najdahmadi et al., [2016] reported fault zone head waves with a constant time delay prior to the direct P arrivals along the Karadere fault. This observation was interpreted with a shallow low velocity zone or an evolving pull-apart basin structure (see Figure 5.13) related to a progression of the two transtensional features at either end of the Karadere fault, the Akyazi Basin in the SW, and the Düzce Basin in the NE (Figure 5.13a).

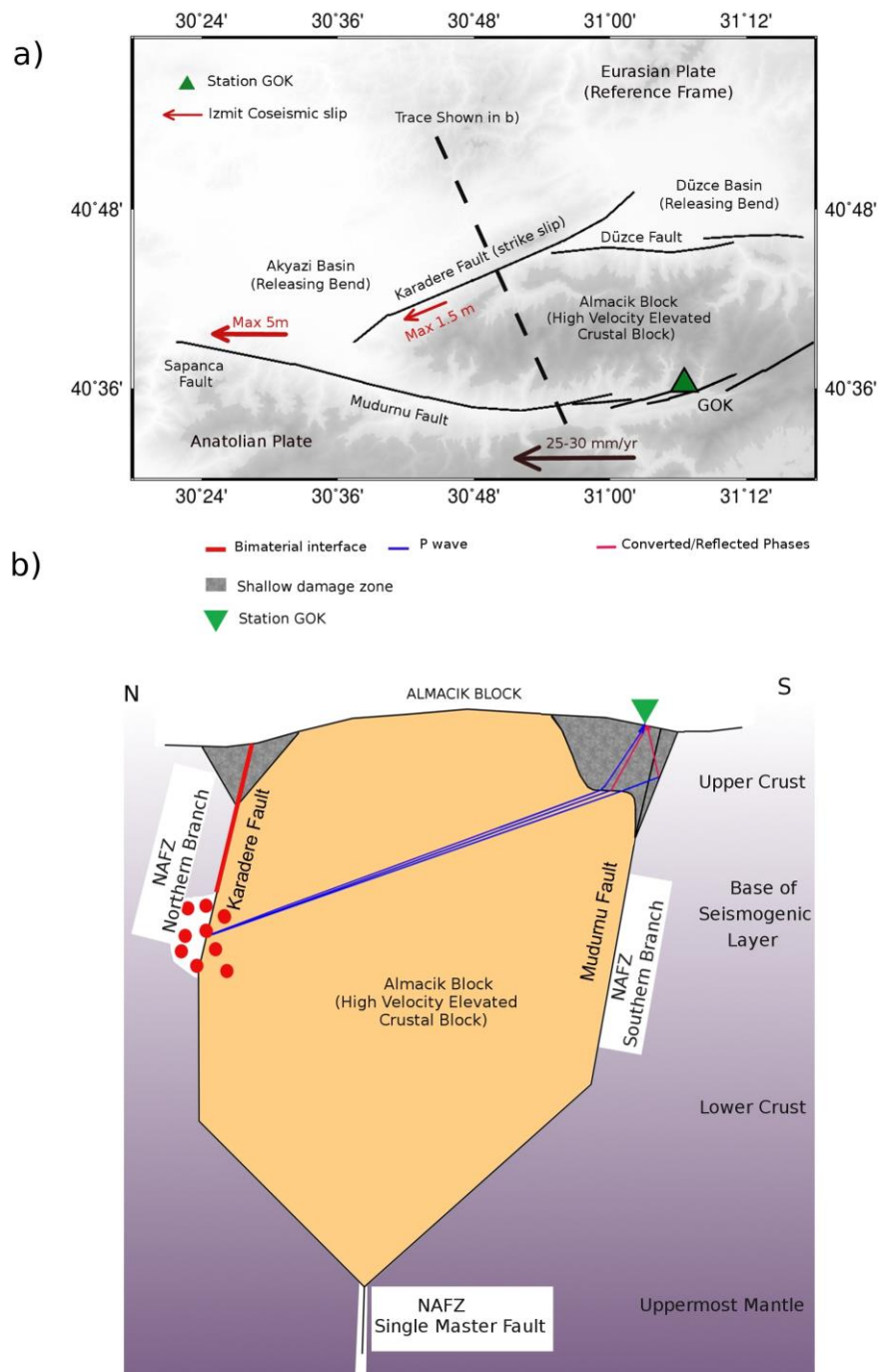


Figure 5.13. Conceptual model in (a) map and (b) fault-normal views. (a) Red arrows show values of the maximum İzmit coseismic slip. Black arrow shows the horizontal velocity of the Anatolian Plate with respect to the Eurasian Plate in the north. (b) The Almacik block is colored in yellow. Gray area north of the Almacik block at the Karadere fault represents a shallow low velocity zone or damaged basin; the red line

represents the deep bimaterial interface detected by *Najdahmadi et al.*, [2016]. Gray area south of the Almacik block at the Mudurnu fault shows a similar structure trapped between two hard blocks where the secondary phases interpreted in this study were produced. Red circles represent the earthquakes; blue lines represent the rays for direct waves; pink lines represent rays for reflected and converted waves observed in this study.

Our interpretation of the secondary phases with a constant time delay after the direct P-wave arrivals could be another manifestation of such a juvenile and evolving early stage of a pull-apart structure at the southern side of the Almacik block, the Mudurnu fault, which would be in good agreement with the regional transtensional setting (see Figure 5.13b).

In our study, we focused on the recordings at station GOK located in front of the Mudurnu fault in respect to the analyzed seismicity. Application of the method to data recorded at stations at the other side of this fault may help to disclose the complex structure of the Mudurnu area. Above, the technique applied here may serve to image the near-vertical faults in other areas and determine potential hazard-prone faults thereby contributing to better constrain future rupture planes.

6. Further Remarks on FZHW analysis

The studies presented in the two previous chapters have shown the potential of FZHW, reflected/converted phases to image and characterize fault zones, first and second order discontinuities. Furthermore, I have studied an adjacent fault segment of the NAFZ that did not lead to results solid enough to be published. However it is important to report on those results as well, which is presented in the following.

The best diagnostic signal to detect and study velocity contrast across a fault is provided by FZHWs that propagate along the interface and are radiated from there to the slow side of the fault [Ben-Zion, 1989; 1990]. Several characteristics can be used to identify FZHWs in general. As mentioned in chapter 2 some of these properties are as follows: FZHWs being short emergent pulses truncated by the closely following sharper direct P wave, having opposite first-motion polarity than the more impulsive following direct waves [Ben-Zion and Malin, 1991]. However, several factors must be considered in FZHW analysis in order to have the correct detections of phases. These factors are described in detail. Also an example of the very first attempt I made in detection of FZHW using a manual approach with possible false detections in the manual approach is expressed.

The first station that I investigated in order to check for existence of bimaterial interfaces was Reşadiye-TOKAT (RSDY), which is one of the Kandili network stations and is located at the eastern part of the NAFZ (Figure 6.1). The station is roughly located in the vicinity of the 1939 Erzincan ($M_s = 7.8-8$) and 1942 Niksar-Erbaa ($M_s = 7.1$) earthquakes, closer to Niksar earthquake. Largest values for the age of the NAFZ are reported for the eastern part decreasing westward. The estimated age of NAFZ from previous studies at the location of RSDY is between 6 to 11 Ma [Bohnhoff *et al.*, 2016b] and the NAFZ is expected to be more mature in this area comparing to the western parts. The Cumulative fault-zone offset in this area is about 80 km [Bohnhoff *et al.*, 2016b; Barka *et al.*, 2000].

Bulut *et al.* [2012a] found bimaterial interfaces across the Mudurnu segment of NAFZ, west of Almacik block, which was the first FZHW analysis performed in the NAFZ. The first station that was chosen afterwards for FZHW analysis was RSDY station, since the NAFZ in this area is more mature. Therefore, in case of existence of a prominent velocity contrast across the fault at this segment FZHWs were expected to be observed clearly.

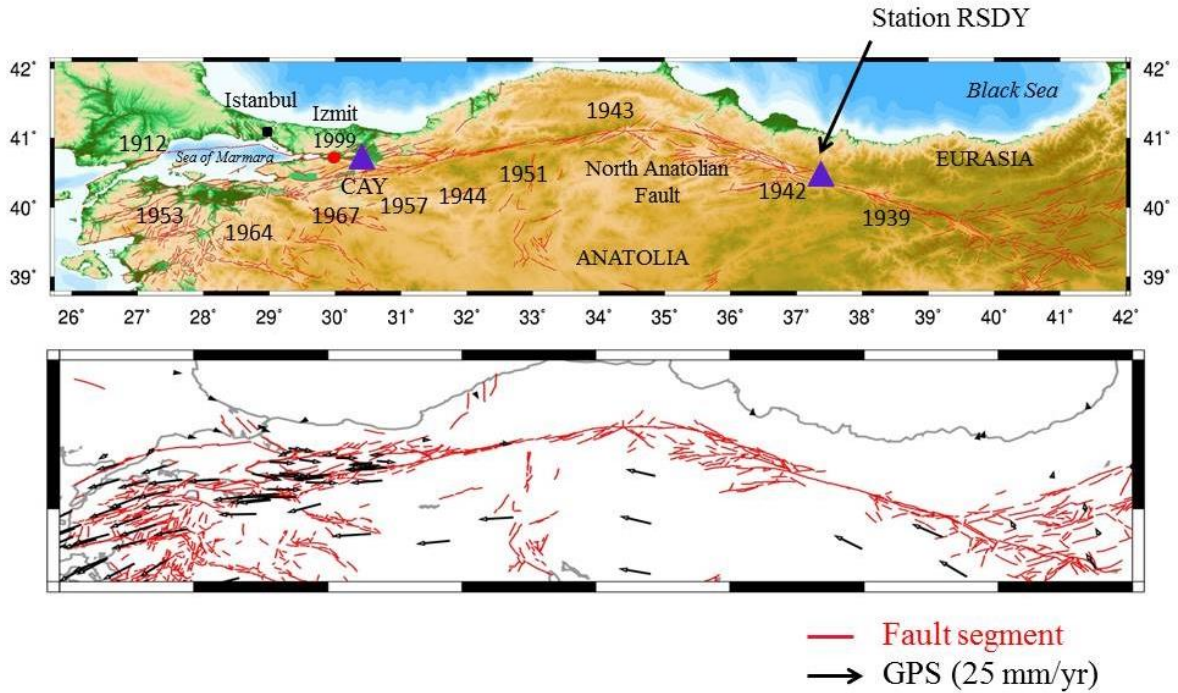


Figure 6.1. North Anatolian Fault Zone and the preliminary area of study. (a) Topography map and RSDY station (triangle) along the fault (red lines). (b) NAFZ and the GPS deformation rates. Fault segments are after <http://www.deprem.gov.tr> and GPS deformation rates are after *Reilinger et al.* [2006].

At that time, no automatic picker for picking fault zone head waves was available. Therefore, in order to look for FZHW, I started by selecting events near the fault (Figure 6.2). Several event selections were tested in this area. An example is a relatively large length along the fault (~150 km) and distance from the fault (~15 km), which was partly due to lack of sufficient seismicity at the southern block and in the vicinity of the station to the west. Next step was finding waveforms with emergent phases (possible FZHW) before a sharp incoming direct P phase.

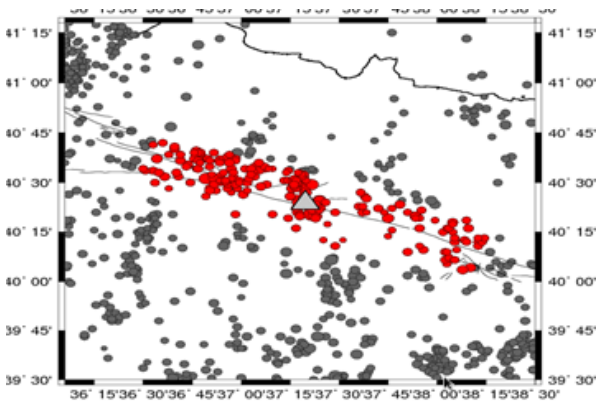


Figure 6.2. Selection of events along the fault. Gray circles represent the seismicity in the area and the red circles are the seismicity selected for identification of FZHW with the manual approach.

After selection of waveforms with apparent characteristics of FZHW on the vertical components, polarization of the horizontal components was tested. At this stage, events with apparent FZHW coming from fault-normal direction and direct-P phase coming from event-station direction were selected. Few events remained as seen in Figure 6.3. Red boxes show the arrival of phases, supposedly the FZHW and green boxes show possible direct P arrivals. The green dashed line is the apparent move out of direct P as waveforms were aligned on the FZHW phase and sorted according to S-P time, suggesting a moveout of phases.

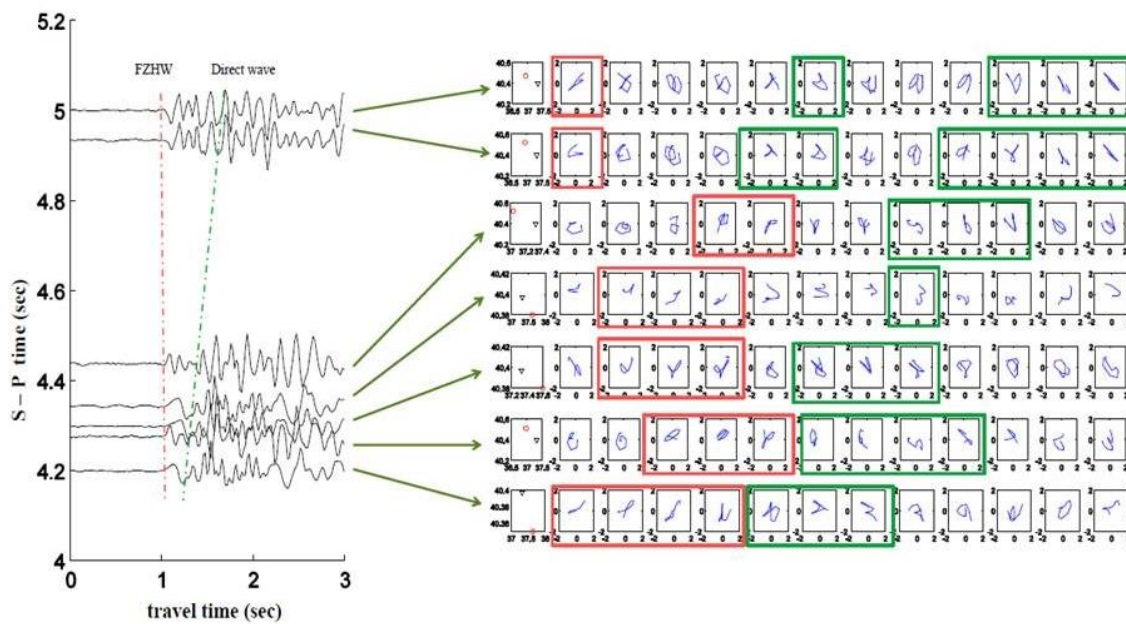


Figure 6.3. Example of vertical P-waveforms and corresponding particle motions after a manual analysis. Vertical P-waveforms recorded at station RSDY (left) and corresponding particle motion of incoming P-wave based on horizontal recordings at RSDY station (right). The onset of apparent FZHW on each series of particle motion is enclosed with red box and the arrival of apparent direct-P phase, is enclosed with green boxes.

Also 2D rotation of the horizontal components was done in order to refine the results of Particle motions, which did not lead to improvements or higher number of detections. As seen in the Figure 6.3, waveforms with apparent FZHW and direct-P as well as rotations of particle motions exist. However, since the number of final seismograms that could possibly contain FZHW phases was not high enough and some other properties of apparent FZHW and direct-P did not match the expectations from theory well (e.g. frequency, amplitude), it was not possible to conclude that a bimaterial interface exists.

To further check the possibility of existence of velocity contrast across the fault at this segment Wadati plots were used [Wadati and Oki, 1933] and VP/VS ratio at two different sides of the fault were calculated. This could reveal more information about one side of the

fault being stiffer than the other side. Results of Wadati plots (Figure 6.4) showed no significant difference between the VP/VS ratios at the northern block in comparison to the southern block of the NAFZ, where station RSDY is located.

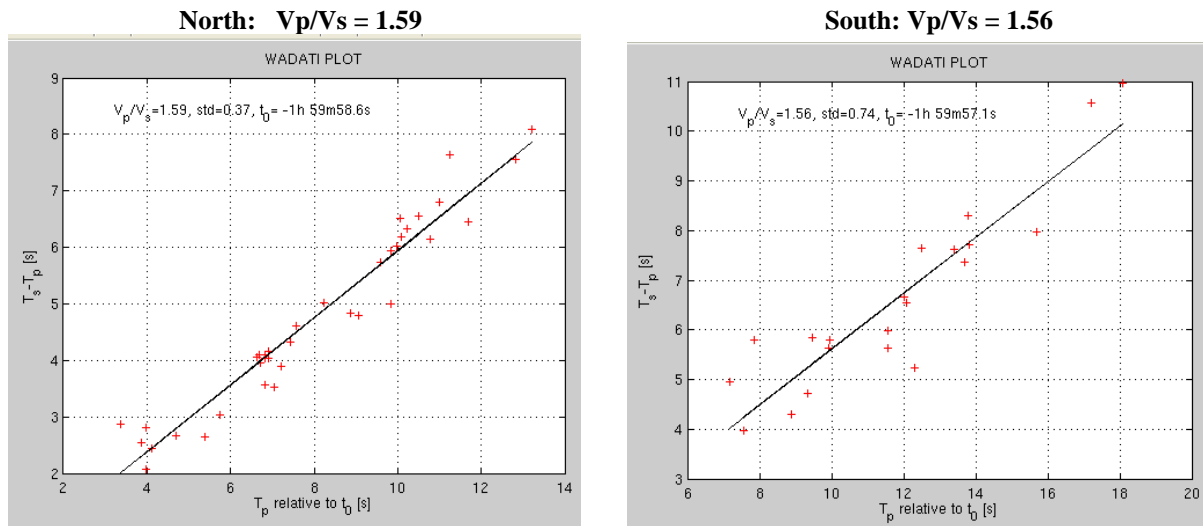


Figure 6.4. Wadati plots. Time separation of the P and S phase ($T_s - T_p$) is plotted against the arrival time of the P-wave for events north of the fault (left) and events south of the fault (right).

This is an example of importance of several factors that need to be considered carefully while performing –manual- FZHW analysis:

- FZHW are emergent phases in comparison to direct P phases.
- Having a strike slip regime in the area, polarities of FZHW and direct P are expected to be opposite. However, if the event mechanisms are more complex, this might not be the case.
- Quality of phases based on the clarity of separation and relative amplitude of FZHW and direct P phases, consistency of polarity with the general right-lateral focal mechanisms of the area, signal-to-noise-ratio, and impulsiveness of the direct P arrival matters [Allam *et al.*, 2014].
- As described in chapter 4, it is possible to observe FZHWs without any move out between FZHW and direct P arrivals, as the distance along the fault increases. This can be an indication of the existence of a shallow low velocity zone in the area. In other words, move out of FZHW is not necessarily a criterion in finding FZHW and its onset.

- During the polarization analysis, consistency of polarization directions and changes between the amplitudes (eigenvalue ratios) give us confidence that the second phase is a direct P wave and that the preceding arrival is a headwave [Allam *et al.*, 2014].
- The expected direction for incoming FZHW, being approximately fault normal direction, can carry uncertainties due to lack of knowledge on the geometry of the fault in certain areas. Therefore, it is important to observe to the consistency of polarization directions carefully and not only consider the supposed fault normal polarizations, which can decrease the number of detections for fault segments with rather unknown directions.
- Because head waves are emergent, first-arriving, and low in amplitude compared to body waves, filtering needs to be chosen carefully. “In general, acausal filters can produce small oscillations preceding high-amplitude arrivals (e.g., P waves). Causal filters lack such acausal effects, but can produce a phase shift” [Allam *et al.*, 2014, P. 3009]. The causal filter can affect the arrival picks of both the head and P waves. Such effects need to be checked on the data before proceeding [Allam *et al.*, 2014].

Due to all complexities that could arise in FZHW analysis, usage of tools such as an automatic picker of FZHW [Ross and Ben-Zion, 2014] and quantified polarization analysis [Allam *et al.*, 2014] are highly recommended. Automatic picker of FZHW can reject many waveforms, which might seem to be FZHW to a person not very experienced or familiar with this topic. Additionally automatic picker of FZHW and direct P wave has high efficiency in time in processing large number of data - without necessity in selecting input events - as the output can be checked further manually.

Following the criteria mentioned above carefully and also using the automatic picker of FZHW no – significant - number of FZHW is detected in this area for further analysis. This can be a result of the northern block being the faster block and might be in accordance with the westward propagation of the 1939 and 1942 earthquakes. As explained in section 2.1.3., the general westward propagation of earthquakes of the NAF is a result of the southern block of North Anatolian Block, being the slower block [e.g., Sengör *et al.*, 2005]. Having no FZHW detected by a station at the northern block, can be an indication of the northern block being the faster block, or having no velocity contrast across the fault. Therefore, better analysis in this section of the NAF, would have been possible in case at least one more station existed at the other side of the fault. Best FZHW analysis is done with record sections of seismograms generated by a large number of earthquakes on the fault of

interest and observed at near-fault stations [e.g., *McGuire and Ben-Zion, 2005; Zhao et al., 2010*].

7. Conclusion and Perspectives

Imaging faults, especially those that are known to produce large earthquakes in the future with subsequent seismic hazard and risk implications, is a challenging yet pressing task. In particular understanding the in part non-homogenous velocity structures along and across the faults is needed in estimating future rupture scenarios. In addition, such studies also provide key information on the local fault zone structure and seismotectonic setting. High resolution seismic survey can provide useful details on crustal structures, but it is expensive especially considering the necessity of using boreholes in order to image vertical structures. Therefore development of other alternative methods with simple and systematic procedure is of high importance.

One of the best tools in studying the velocity contrast across a fault is FZHW. As described in chapter 4, the FZHW analysis was successfully performed to image the velocity contrast across the Karadere segment of NAFZ using seven stations located within and around the damage zone of the Karadere fault. In order to perform the FZHW analysis systematically, an automatic procedure for the identification and picking of FZHW and direct P arrivals [Ross and Ben-Zion, 2014] was used. Next, a manual revision of the automatic picks using a particle motion analysis [Bulut et al., 2012a; Allam et al., 2014] was performed. In addition to the final FZHWs, a substantial subset of waveforms appeared to have first arriving direct P wave followed by a phase that was reflected from a fault interface (FZRW). After the manual analysis and application of strict quality criteria, 187 high quality FZHW picks and 215 high quality FZRW picks were left. Furthermore, due to the tight network coverage, two types of FZHW were detected. The first type of FZHW had a systematic moveout from the direct P phases with increasing propagation distance along the fault, which are commonly observed in other FZHW analysis studies. These FZHW are associated with a large-scale bimaterial interface that extends to the bottom of the seismogenic zone and is continuous along the strike for tens of kilometers [e.g., Ben-Zion and Malin, 1991; Allam et al., 2014]. The second type of FZHW that was detected had no moveout from the direct P waves with an increasing hypocentral distance, which was a novel observation at the time the study was performed. This type of FZHW is associated with a shallow local bimaterial interface.

In the reported study of chapter 4, two stations were very close to the fault or within the trapping structure of the fault and were affected by the shallow local bimaterial interface

of the damage zone, which had primarily non-moveout of the FZHW recorded. Observations suggested an extension of a relatively broad damage zone to the Almacik block in some parts. Stations that recorded both ample moveout and non-moveout FZHW were an indication of being located on the slow block, near the core of the damage zone. Stations that were too far from the deep bimaterial interface or on the faster block and further away from the damage zone, did not record FZHWs (moveout or non-moveout).

The average velocity contrast east and west of the stations were estimated to be about 2.87% and 3.91%, respectively in the top 15-18 km. The fact that events down to 18 km depth produce FZHW with large moveout indicates that the deep bimaterial interface extends down to the base of the seismogenic crust. The obtained $\sim 3.4\% \pm 0.3\%$ average velocity contrast across the fault is somewhat lower than most values observed for other transform faults.

A reduction of the velocity contrast along the NAFZ at the Karadere fault may have helped to stop the 1999 Izmit rupture in that area, since the dynamic reduction of normal stress along a bimaterial interface increases with growing velocity contrast up to about 30-40% contrast of *S* wave velocities [e.g., *Ben-Zion and Andrews, 1998; Ranjith and Rice, 2001*]. Thus, if the velocity contrast is lower to the east, the Izmit rupture propagation to the east encountered an increasing frictional strength, due to the diminishing dynamic reduction of normal stress associated with the decreasing velocity contrast. A significant damage zone can be the consequence of repeating rupture arrests along the Karadere fault.

Combining all 'non moveout' phases, the mean differential time between the FZHW and direct P waves were associated with the data was about 0.11 ± 0.02 sec. The shallow low velocity body generating the 'non moveout' FZHW exists on both sides of the Karadere fault. The depth extent of the bimaterial interface at the edge of the low velocity zone is estimated to be about 3.8 to 4.7 km. These values are similar to the estimated depth values of the trapping and anisotropic fault structures in the area [*Ben-Zion et al., 2003; Peng and Ben-Zion, 2004*], supporting the damaged fault zone layer interpretation.

A second approach in imaging faults was performed by modification of a recent method developed by *Hrubcová et al. [2016]*, which was used to image the structures in the vicinity of Mudurnu segment of the NAFZ. About 4000 events recorded by three stations of Sabonet network around the Mudurnu segment of NAFZ were analyzed cluster by cluster. The results showed existence of several phases in the recordings of all stations with constant time difference from direct P arrivals as waveforms were plotted accordingly to depth or

epicentral distance, which suggested that the phases were generated at structures near the stations.

In addition to detecting phases on the vertical components with criteria such as amplitude of phases, arrival times and time difference in each cluster, the horizontal components were included in the investigation and the rest of it was done, particularly for recordings of one station with higher data quality. The first phase with higher time difference of 0.5 sec after the direct P arrival (minor phase) had mostly characteristics of a P-type phase. The prominent phase afterwards around 0.9 sec (major phase) seemed to be a converted PS phase and its polarization was in agreement with the observations of *Hurd and Bohnhoff*, [2012] with shear wave splitting in the area.

Synthetics tests were mostly done for the prominent PS phase. For the case of horizontal layers producing the converted phases, discrete wavenumber method of *Bouchon*, [1981] was used. The time delay of ~ 0.9 s was fitted by a velocity model with a horizontal interface at the depth of 4 km with the downward increased velocities. The minor P-type phase preceding the PS conversion could be a PPP phase reflected from an uppermost discontinuity beneath the station. Assuming the P-wave velocity to be in a range of ~ 3.2 - 3.8 km/s in the subsurface layer, the time delay of 0.5 s between the P and PPP phases indicated the bottom of this layer to be at ~ 800 - 900 m.

Alternatively, to tests the second possible model, which was a steeply inclined interface reflecting the geological setting of the Mudurnu fault with higher velocity at its southern side, synthetics were performed using the ray tracing method of *Červený and Pšenčík*, [1984]. The synthetics produced the PS conversions with a roughly constant time delay after the P-wave arrival, but with rather small amplitudes. Synthetics also produced the PP reflections preceding the PS phase, generated at the same interface.

The analysis of the particle motions of the direct and the secondary phases did not help us to further discriminate between the two models. Because of anisotropy in the upper crust both direct and converted S phases were affected by shear-wave splitting that increased the limitations on the interface identification. The minor P-type secondary phase had rather complicated polarization, which made it is difficult to resolve whether it was produced by the horizontal layered or steeply inclined structure. Finally, the combination of a horizontal interface (the most robust solution in crustal studies) at ~ 4 km as well as a steeply inclined interface, producing PS reflected conversions at shallow depths of ~ 2 - 3 km (also explaining

the observed secondary phases and in accordance with the existing Mudurnu fault) was the best model in the interpretation of the observations.

The existence of FZHW with a constant time difference from the direct P arrivals at the Karadere segment was interpreted to reflect a shallow and low velocity/damage zone or an evolving pull-apart basin structure related to a progression of the two transtensional features at either end of the Karadere Fault, the Akyazi Basin in the SW, and the Düzce Basin in the NE. The existence of major and minor phases, their corresponding polarizations and synthetics results, suggest the existence of a similar pull-apart structure at early stage, south of the Almacik block (Mudurnu fault) in agreement with the transtensional setting in the area.

The techniques applied here to image velocity contrast across the Karadere fault and the near-vertical Mudurnu fault may serve to use near-fault recordings in other areas to image potential hazard-prone faults thereby contribute to better constraining of future rupture planes and associated seismic hazard and risk.

7.1. Perspectives

The achieved results from this research are followed by these perspectives:

- **Application of methods in the Sea of Marmara:** This includes both methods of the Identification of velocity contrast across the fault using FZHW as described in chapter 4 and identification of crustal discontinuities inferred from microearthquakes using the method described in chapter 5. The Marmara section of the NAFZ is located between the 1912 Ganos and 1999 Izmit ruptures and has produced the last major earthquake in 1766 at an average recurrence time of 200-250 years [Ambraseys and Jackson, 2000; Bohnhoff *et al.*, 2016b]. It is currently overdue for an $M > 7$ earthquake.

As a result, this fault section and in particular its eastern part along the Princes Islands segment is the target region for the number of scientific projects to study this earthquake-prone fault and its implications for seismic hazard and risk for the nearby 15-million population center of Istanbul [Bohnhoff *et al.*, 2013]. Consequently, the eastern Sea of Marmara is the target area for an ICDP-driven borehole based near-fault monitoring observatory (GONAF – Geophysical Observatory at the North Anatolian Fault). GONAF has been implemented between 2012-2015 and includes a total of seven 300m deep

boreholes instrumented with vertical seismic arrays around the target fault [Prevedel *et al.*, 2015]. The high quality data from GONAF boreholes, beside other networks in the Sea of Marmara can be used as the next step to gain information on the structure of the NAFZ and velocity changes across the fault, which will have substantial implications for directivity effects and associated seismic hazard of pending large earthquakes of the region.

Furthermore, the Ganos fault was activated in a M7.4 event in 1912 and believed to be a straight vertical fault that is currently locked down to ~15 km depth and can be a potential segment for future studies.

- **Fault Zone Trapped Wave and other signals as additional tools:** Throughout the analysis of other segments Fault Zone Trapped Waves (FZTW) can be used for a better understanding of structure of faults as well. The amplitude, frequency content and duration of FZTW are very sensitive to the width of the fault as well as velocity reduction, attenuation coefficient and propagation distance within the fault zone layer [Ben-Zion and Andrews, 1998]. Thus FZTW can provide information on the mentioned properties [e.g., Li *et al.*, 1990; Peng *et al.*, 2003; Lewis *et al.*, 2005; Mizuno and Nishigami, 2006; Calderoni *et al.*, 2012]. However, the modelling approach should account for the significant trade-offs between model parameters [Ben-Zion and Andrews, 1998; Jahnke *et al.*, 2002; Lewis and Ben-Zion, 2010]. FZTW, along with FZHW, teleseismic delay time analysis and local P-wave delay time analysis can be used in case of having access to a dense linear array crossing the surface trace of a fault, in order to image the fault with high resolution [Qiu *et al.*, 2017]. Also Seismic imaging from data provided by earthquake seismograms has time resolution limited by event rates, where ambient noise imaging has relatively low time resolution. Space resolution of earthquake seismograms can go down to an interface, where space resolution of imaging using ambient noise techniques is between 10 to 100 meters. Earthquake data provide detailed information on the seismogenic sections (depth 3-15 km), where ambient noise data provide detailed information on the shallower structure. Therefore, analysis of seismograms with earthquake and noise signals can give the best output from both imaging techniques.

Overall, investigating the previously mentioned issues not only has important insights into the structure of the NAFZ in the mentioned segments and provide information useful for

seismic hazard studies in the area, but can also improve the existing methods in imaging fault zone structures.

References

- Adams, G. G. (1995), Self-Excited Oscillations of Two Elastic Half-Spaces Sliding With a Constant Coefficient of Friction, *Journal of Applied Mechanics*, 62(4), 867-872, doi:10.1115/1.2896013.
- Aki, K., and P. G. Richards (2002), *Quantitative seismology*.
- Allam, A. A., and Y. Ben-Zion (2012), Seismic velocity structures in the southern California plate-boundary environment from double-difference tomography, *Geophysical Journal International*, 190(2), 1181-1196, doi:10.1111/j.1365-246X.2012.05544.x.
- Allam, A. A., Y. Ben-Zion, and Z. Peng (2014), Seismic Imaging of a Bimaterial Interface Along the Hayward Fault, CA, with Fault Zone Head Waves and Direct P Arrivals, *Pure and Applied Geophysics*, 171(11), 2993-3011, doi:10.1007/s00024-014-0784-0.
- Ambraseys, N. N., and J. A. Jackson (2000), Seismicity of the Sea of Marmara (Turkey) since 1500, *Geophysical Journal International*, 141(3), F1-F6, doi:10.1046/j.1365-246x.2000.00137.x.
- Ambraseys, N. N., and A. Zatopek (1969), The Mudurnu Valley, West Anatolia, Turkey, earthquake of 22 July 1967, *Bulletin of the Seismological Society of America*, 59(2), 521-589.
- Ampuero, J.-P., and Y. Ben-Zion (2008), Cracks, pulses and macroscopic asymmetry of dynamic rupture on a bimaterial interface with velocity-weakening friction, *Geophysical Journal International*, 173(2), 674-692.
- Andrews, D. J., and Y. Ben-Zion (1997), Wrinkle-like slip pulse on a fault between different materials, *Journal of Geophysical Research: Solid Earth*, 102(B1), 553-571, doi:10.1029/96JB02856.
- Bakku, S. (2008), Introduction to Seismology, (*MIT OpenCourseWare: Massachusetts Institute of Technology*), <https://ocw.mit.edu/courses/earth-atmospheric-and-planetary-sciences/12-510-introduction-to-seismology-spring-2010/#>, License: Creative commons BY-NC-SA.
- Barka, A. (1992), The north Anatolian fault zone, paper presented at Annales tectonicae.
- Barka, A. (1999), The 17 august 1999 Izmit earthquake.
- Barka, A., H. Akyüz, E. Altunel, G. Sunal, Z. Cakir, A. Dikbas, B. Yerli, R. Armijo, B. Meyer, and J. De Chabalier (2002), The surface rupture and slip distribution of the 17 August 1999 Izmit earthquake (M 7.4), North Anatolian fault, *Bulletin of the Seismological Society of America*, 92(1), 43-60.
- Barka, A., H. S. Akyüz, H. A. Cohen, and F. Watchorn (2000), Tectonic evolution of the Niksar and Tasova-Erbaa pull-apart basins, North Anatolian Fault Zone: their significance for the motion of the Anatolian block, *Tectonophysics*, 322(3), 243-264.
- Ben-Zion, Y. (1989), The response of two joined quarter spaces to SH line sources located at the material discontinuity interface, *Geophysical Journal International*, 98(2), 213-222.
- Ben-Zion, Y. (1990), The response of two half spaces to point dislocations at the material interface, *Geophysical Journal International*, 101(3), 507-528.
- Ben-Zion, Y. (2001), Dynamic ruptures in recent models of earthquake faults, *Journal of the Mechanics and Physics of Solids*, 49(9), 2209-2244.
- Ben-Zion, Y. (2013), Multi-scale 4D imaging of fault zone environments; Erice Mai Workshop;
- Ben-Zion, Y., and K. Aki (1990), Seismic radiation from an SH line source in a laterally heterogeneous planar fault zone, *Bulletin of the Seismological Society of America*, 80(4), 971-994.
- Ben-Zion, Y., and J.-P. Ampuero (2009), Seismic radiation from regions sustaining material damage, *Geophysical Journal International*, 178(3), 1351-1356.
- Ben-Zion, Y., and D. Andrews (1998), Properties and implications of dynamic rupture along a material interface, *Bulletin of the Seismological Society of America*, 88(4), 1085-1094.

- Ben-Zion, Y., and P. Malin (1991), San Andreas fault zone head waves near Parkfield, California, *Science*, 251(5001), 1592-1594.
- Ben-Zion, Y., S. Katz, and P. Leary (1992), Joint inversion of fault zone head waves and direct P arrivals for crustal structure near major faults, *Journal of Geophysical Research: Solid Earth*, 97(B2), 1943-1951, doi:10.1029/91JB02748.
- Ben-Zion, Y., Z. Peng, D. Okaya, L. Seeber, J. G. Armbruster, N. Ozer, A. J. Michael, S. Baris, and M. Aktar (2003), A shallow fault-zone structure illuminated by trapped waves in the Karadere–Duzce branch of the North Anatolian Fault, western Turkey, *Geophysical Journal International*, 152(3), 699-717.
- Ben-Zion, Y., T. K. Rockwell, Z. Shi, and S. Xu (2012), Reversed-polarity secondary deformation structures near fault stepovers, *Journal of Applied Mechanics*, 79(3), 031025.
- Ben-Zion, Y., and C. G. Sammis (2003), Characterization of Fault Zones, *pure and applied geophysics*, 160(3), 677-715, doi:10.1007/pl00012554.
- Ben-Zion, Y., and Z. Shi (2005), Dynamic rupture on a material interface with spontaneous generation of plastic strain in the bulk, *Earth and Planetary Science Letters*, 236(1–2), 486-496, doi:<http://dx.doi.org/10.1016/j.epsl.2005.03.025>.
- Benites, R., K. Aki, and K. Yomogida (1992), Multiple scattering of SH waves in 2-D media with many cavities, *pure and applied geophysics*, 138(3), 353-390, doi:10.1007/bf00876878.
- Beyhan, G., and M. A. Alkan (2015), Three-dimensional structure of Vp in the upper crust of the Sakarya Basin, NW Turkey, *Arabian Journal of Geosciences*, 8(8), 6371-6383, doi:10.1007/s12517-014-1605-6.
- Bindi, D., S. Parolai, E. Görgün, H. Grosser, C. Milkereit, M. Bohnhoff, and E. Durukal (2007), ML scale in Northwestern Turkey from 1999 Izmit aftershocks: updates, *Bulletin of the Seismological Society of America*, 97(1B), 331-338.
- Bohnhoff, M., F. Bulut, G. Dresen, P. E. Malin, T. Eken, and M. Aktar (2013), An earthquake gap south of Istanbul, *Nature communications*, 4.
- Bohnhoff, M., H. Grosser, and G. Dresen (2006), Strain partitioning and stress rotation at the North Anatolian fault zone from aftershock focal mechanisms of the 1999 Izmit Mw= 7.4 earthquake, *Geophysical Journal International*, 166(1), 373-385, doi:10.1111/j.1365-246X.2006.03027.x.
- Bohnhoff, M., H.-P. Harjes, and T. Meier (2005), Deformation and stress regimes in the Hellenic subduction zone from focal mechanisms, *Journal of Seismology*, 9(3), 341-366.
- Bohnhoff, M., M. Ickrath, and G. Dresen (2016a), Seismicity distribution in conjunction with spatiotemporal variations of coseismic slip and postseismic creep along the combined 1999 Izmit–Düzce rupture, *Tectonophysics*, 686, 132-145.
- Bohnhoff, M., P. Martínez-Garzón, F. Bulut, E. Stierle, and Y. Ben-Zion (2016b), Maximum earthquake magnitudes along different sections of the North Anatolian fault zone, *Tectonophysics*, 674, 147-165.
- Boness, N. L., and M. D. Zoback (2006), A multiscale study of the mechanisms controlling shear velocity anisotropy in the San Andreas Fault Observatory at Depth, *GEOPHYSICS*, 71(5), F131-F146, doi:10.1190/1.2231107.
- Bormann, P., Engdahl, E. R., & Kind, R. (2012a), Seismic Wave Propagation and Earth models, *Deutsches GeoForschungsZentrum (GFZ)*, doi:https://doi.org/10.2312/GFZ.NMSOP-2_ch2.
- Bormann, P. E. (2012b), New Manual of Seismological Observatory Practice (NMSOP-2), IASPEI, *GFZ German Research Centre for Geosciences, Potsdam*; <http://nmsop.gfz-potsdam.de/>, doi:DOI: 10.2312/GFZ.NMSOP-2.
- Bouchon, M. (1981), A simple method to calculate Green's functions for elastic layered media, *Bulletin of the Seismological Society of America*, 71(4), 959-971.

- Bouchon, M., M. Campillo, and S. Gaffet (1989), A boundary integral equation-discrete wavenumber representation method to study wave propagation in multilayered media having irregular interfaces, *Geophysics*, 54(9), 1134-1140.
- Brietzke, G. B., and Y. Ben-Zion (2006), Examining tendencies of in-plane rupture to migrate to material interfaces, *Geophysical Journal International*, 167(2), 807-819, doi:10.1111/j.1365-246X.2006.03137.x.
- Brossier, R. V., J (2011), Lecture Notes on Full Waveform Inversion, *SEISCOPE Consortium*, <http://seiscope.oca.eu>.
- Brückl, E., et al. (2007), Crustal structure due to collisional and escape tectonics in the Eastern Alps region based on profiles Alp01 and Alp02 from the ALP 2002 seismic experiment, *Journal of Geophysical Research: Solid Earth*, 112(B6), n/a-n/a, doi:10.1029/2006JB004687.
- Bulut, F., Y. Ben-Zion, and M. Bohnhoff (2012a), Evidence for a bimaterial interface along the Mudurnu segment of the North Anatolian Fault Zone from polarization analysis of P waves, *Earth and Planetary Science Letters*, 327, 17-22.
- Bulut, F., M. Bohnhoff, M. Aktar, and G. Dresen (2007), Characterization of aftershock fault plane orientations of the 1999 Izmit (Turkey) earthquake using high-resolution aftershock locations, *Geophysical Research Letters*, 34(20).
- Bulut, F., M. Bohnhoff, T. Eken, C. Janssen, T. Kılıç, and G. Dresen (2012b), The East Anatolian Fault Zone: Seismotectonic setting and spatiotemporal characteristics of seismicity based on precise earthquake locations, *Journal of Geophysical Research: Solid Earth*, 117(B7), doi:10.1029/2011JB008966.
- Burchfiel, B., and J. Stewart (1966), "Pull-apart" origin of the central segment of Death Valley, California, *Geological Society of America Bulletin*, 77(4), 439-442.
- Calderoni, G., R. Di Giovambattista, P. Vannoli, S. Pucillo, and A. Rovelli (2012), Fault-trapped waves depict continuity of the fault system responsible for the 6 April 2009 M w 6.3 L'Aquila earthquake, central Italy, *Earth and Planetary Science Letters*, 323, 1-8.
- Calderoni, G., A. Rovelli, Y. Ben-Zion, and R. Di Giovambattista (2015), Along-strike rupture directivity of earthquakes of the 2009 L'Aquila, central Italy, seismic sequence, *Geophysical Journal International*, 203(1), 399-415.
- Červený, V. (2001), *Seismic Ray Theory*, Cambridge University Press.
- Červený, V., Pšenčík, I (1977), *Ray method in seismology*, Praha : Univerzita Karlova, 1977. 214 p. : ill. ; 24 cm.
- Červený, V., L. Klimeš, and I. Pšenčík (2007), Seismic ray method: Recent developments, *Advances in Geophysics*, 48, 1-126.
- Cervený, V., Pšenčík, I (1984), SEIS83 - Numerical modeling of seismic wave fields in 2-D laterally varying layered structures by the ray method, *Engdahl E.R. (Ed.), Documentation of Earthquake Algorithms. Report SE-35. World Data Center A for Solid Earth Geophysics, Boulder, CO*, 36-40.
- Chapman, C. H. (2002), Seismic ray theory and finite frequency extensions. In: Lee, W. H. K., Kanamori, H., Jennings, P. C., and Kisslinger, C. (Eds.) (2002). *International Handbook of Earthquake and Engineering Seismology, Part A. Academic Press, Amsterdam*, 103-123.
- Chavarria, J. A., P. Malin, R. D. Catchings, and E. Shalev (2003), A look inside the San Andreas fault at Parkfield through vertical seismic profiling, *Science*, 302(5651), 1746-1748.
- Chávez-Pérez, S. L., John N. (1998), Crustal imaging in southern California using earthquake sequences, *Tectonophysics*, 286(1), 223-236, doi:[http://dx.doi.org/10.1016/S0040-1951\(97\)00267-9](http://dx.doi.org/10.1016/S0040-1951(97)00267-9).
- Cochran, E. S., Vidale, J.E. & Li, Y.-G., (2003), Near-fault anisotropy following the Hector Mine earthquake, *J. geophys. Res.*, doi:10.1029/2002JB002352.

- Copley, A., and D. McKenzie (2007), Models of crustal flow in the India-Asia collision zone, *Geophysical Journal International*, 169(2), 683-698.
- Crowell, J. C. (1974), Origin of late Cenozoic basins in southern California.
- Dor, O., T. K. Rockwell, and Y. Ben-Zion (2006), Geological Observations of Damage Asymmetry in the Structure of the San Jacinto, San Andreas and Punchbowl Faults in Southern California: A Possible Indicator for Preferred Rupture Propagation Direction, *pure and applied geophysics*, 163(2), 301-349, doi:10.1007/s00024-005-0023-9.
- Dor, O., C. Yildirim, T. K. Rockwell, Y. Ben-Zion, O. Emre, M. Sisk, and T. Y. Duman (2008), Geological and geomorphologic asymmetry across the rupture zones of the 1943 and 1944 earthquakes on the North Anatolian Fault: possible signals for preferred earthquake propagation direction, *Geophysical Journal International*, 173(2), 483-504.
- Eberhart-Phillips, D., and A. J. Michael (1993), Three-dimensional velocity structure, seismicity, and fault structure in the Parkfield Region, central California, *Journal of Geophysical Research: Solid Earth*, 98(B9), 15737-15758, doi:10.1029/93JB01029.
- Eken, T., M. Bohnhoff, F. Bulut, B. Can, and M. Aktar (2013), Crustal anisotropy in the eastern Sea of Marmara region in northwestern Turkey, *Bulletin of the Seismological Society of America*, 103(2A), 911-924.
- Finzi, Y., E. H. Hearn, Y. Ben-Zion, and V. Lyakhovsky (2009), Structural properties and deformation patterns of evolving strike-slip faults: Numerical simulations incorporating damage rheology, *Pure and Applied Geophysics*, 166(10-11), 1537-1573.
- Fisher, A., and K. Becker (2000), Channelized fluid flow in oceanic crust reconciles heat-flow and permeability data, *Nature*, 403(6765), 71-74.
- Flerit, F., R. Armijo, G. King, and B. Meyer (2004), The mechanical interaction between the propagating North Anatolian Fault and the back-arc extension in the Aegean, *Earth and Planetary Science Letters*, 224(3), 347-362.
- Fuchs, K., and G. Müller (1971), Computation of Synthetic Seismograms with the Reflectivity Method and Comparison with Observations, *Geophysical Journal of the Royal Astronomical Society*, 23(4), 417-433, doi:10.1111/j.1365-246X.1971.tb01834.x.
- Fukao, Y., S. Hori, and M. Ukawa (1983), A seismological constraint on the depth of basalt–eclogite transition in a subducting oceanic crust.
- Görgün, E., M. Bohnhoff, F. Bulut, and G. Dresen (2010), Seismotectonic setting of the Karadere–Düzce branch of the North Anatolian Fault Zone between the 1999 Izmit and Düzce ruptures from analysis of Izmit aftershock focal mechanisms, *Tectonophysics*, 482(1), 170-181.
- Gülen, L., A. Pinar, D. Kalafat, N. Özel, G. Horasan, M. Yilmazer, and A. M. Işıkara (2002), Surface Fault Breaks, Aftershock Distribution, and Rupture Process of the 17 August 1999 İzmit, Turkey, Earthquake, *Bulletin of the Seismological Society of America*, 92(1), 230-244, doi:10.1785/0120000815.
- Hamiel, Y., and Y. Fialko (2007), Structure and mechanical properties of faults in the North Anatolian Fault system from InSAR observations of coseismic deformation due to the 1999 Izmit (Turkey) earthquake, *Journal of Geophysical Research: Solid Earth (1978–2012)*, 112(B7).
- Hardebeck, J. L., and E. Hauksson (2001), Crustal stress field in southern California and its implications for fault mechanics, *Journal of Geophysical Research: Solid Earth (1978–2012)*, 106(B10), 21859-21882.
- Hartleb, R. D., J. F. Dolan, H. S. Akyüz, T. E. Dawson, A. Z. Tucker, B. Yerli, T. K. Rockwell, E. Toraman, Z. Çakir, and A. Dikbaş (2002), Surface rupture and slip distribution along the Karadere segment of the 17 August 1999 Izmit and the western section of the 12 November 1999 Düzce, Turkey, earthquakes, *Bulletin of the Seismological Society of America*, 92(1), 67-78.

- Haskell, N. A. (1953), The dispersion of surface waves on multilayered media, *Bulletin of the Seismological Society of America*, 43(1), 17-34.
- Hearn, E. H., R. Bürgmann, and R. E. Reilinger (2002), Dynamics of Izmit earthquake postseismic deformation and loading of the Düzce earthquake hypocenter, *Bulletin of the Seismological Society of America*, 92(1), 172-193.
- Hickman, S. H. (1991), Stress in the lithosphere and the strength of active faults, *Rev. Geophys*, 29, 759-775.
- Hole, J. A. (1992), Nonlinear high-resolution three-dimensional seismic travel time tomography, *Journal of Geophysical Research: Solid Earth*, 97(B5), 6553-6562, doi:10.1029/92JB00235.
- Hough, S., Y. Ben-Zion, and P. Leary (1994), Fault-zone waves observed at the southern Joshua Tree earthquake rupture zone, *Bulletin of the Seismological Society of America*, 84(3), 761-767.
- Hrubcová, P., V. Vavryčuk, A. Boušková, and M. Bohnhoff (2016), Shallow crustal discontinuities inferred from waveforms of microearthquakes: Method and application to KTB Drill Site and West Bohemia Swarm Area, *Journal of Geophysical Research: Solid Earth*.
- Hrubcová, P., V. Vavryčuk, A. Boušková, and J. Horálek (2013), Moho depth determination from waveforms of microearthquakes in the West Bohemia/Vogtland swarm area, *Journal of Geophysical Research: Solid Earth*, 118(1), 120-137, doi:10.1029/2012JB009360.
- Huang, Y., and J.-P. Ampuero (2011), Pulse-like ruptures induced by low-velocity fault zones, *Journal of Geophysical Research: Solid Earth*, 116(B12), n/a-n/a, doi:10.1029/2011JB008684.
- Hubert-Ferrari, A., R. Armijo, G. King, B. Meyer, and A. Barka (2002), Morphology, displacement, and slip rates along the North Anatolian Fault, Turkey, *Journal of Geophysical Research: Solid Earth (1978–2012)*, 107(B10), ETG 9-1-ETG 9-33.
- Hudson, J. A. (2000), Principles of seismology Agustín Udias, Cambridge University Press, Cambridge, 2000, 475 + xiv pp, ISBN 0 521 62478 9, Paperback, £24.95, *Geophysical Journal International*, 143(3), 988-988, doi:10.1046/j.0956-540X.2000.01273_143_3.x.
- Hurd, O., and M. Bohnhoff (2012), Stress and Structure-Induced Shear-Wave Anisotropy along the 1999 Izmit Rupture, Northwest Turkey, *Bulletin of the Seismological Society of America*, 102(5), 2177-2188, doi:10.1785/0120110270.
- Ickrath, M., M. Bohnhoff, F. Bulut, and G. Dresen (2014), Stress rotation and recovery in conjunction with the 1999 Izmit Mw 7.4 earthquake, *Geophysical Journal International*, 196(2), 951-956, doi:10.1093/gji/ggt409.
- Ickrath, M., M. Bohnhoff, G. Dresen, P. Martínez-Garzón, F. Bulut, G. Kwiątek, and O. Germer (2015), Detailed analysis of spatiotemporal variations of the stress field orientation along the Izmit-Düzce rupture in NW Turkey from inversion of first-motion polarity data, *Geophysical Journal International*, 202(3), 2120-2132.
- Jahnke, G., H. Igel, and Y. Ben-Zion (2002), Three-dimensional calculations of fault-zone-guided waves in various irregular structures, *Geophysical Journal International*, 151(2), 416-426, doi:10.1046/j.1365-246X.2002.01784.x.
- Jongmans, D., and P. E. Malin (1995), Microearthquake S-wave observations from 0 to 1 km in the Varian well at Parkfield, California, *Bulletin of the Seismological Society of America*, 85(6), 1805-1820.
- Jurkevics, A. (1988), Polarization analysis of three-component array data, *Bulletin of the Seismological Society of America*, 78(5), 1725-1743.
- Kaiser, A. E., A. G. Green, F. M. Campbell, H. Horstmeyer, E. Manukyan, R. M. Langridge, A. F. McClymont, N. Mancktelow, M. Finnemore, and D. C. Nobes (2009), Ultrahigh-resolution seismic reflection imaging of the Alpine Fault, New Zealand, *Journal of Geophysical Research: Solid Earth*, 114(B11), n/a-n/a, doi:10.1029/2009JB006338.

- McGuire, J., and Y. Ben-Zion (2005), High-resolution imaging of the Bear Valley section of the San Andreas Fault at seismogenic depths with fault-zone head waves and relocated seismicity, *Geophysical Journal International*, 163(1), 152-164.
- Kennett, B., E. Engdahl, and R. Buland (1995), Constraints on seismic velocities in the Earth from traveltimes, *Geophysical Journal International*, 122(1), 108-124.
- Kennett, B. L. N. (1983), Seismic wave propagation in stratified media. ISBN 0-521-23933-8, Cambridge University Press, Cambridge, viii + 242 pp.
- Koerner, A., E. Kissling, and S. A. Miller (2004), A model of deep crustal fluid flow following the Mw = 8.0 Antofagasta, Chile, earthquake, *Journal of Geophysical Research: Solid Earth*, 109(B6), n/a-n/a, doi:10.1029/2003JB002816.
- Korneev, V. A., R. M. Nadeau, and T. V. McEvilly (2003), Seismological Studies at Parkfield IX: Fault-Zone Imaging Using Guided Wave Attenuation, *Bulletin of the Seismological Society of America*, 93(4), 1415-1426, doi:10.1785/0120020114.
- Kulhánek, O. (1990), Anatomy of seismograms, edited, Elsevier, Amsterdam; New York.
- Kurzon, I., F. Vernon, Y. Ben-Zion, and G. Atkinson (2014), Ground motion prediction equations in the San Jacinto fault zone: significant effects of rupture directivity and fault zone amplification, *Pure and Applied Geophysics*, 171(11), 3045-3081.
- Latorre, D., T. Blacic, J. Virieux, and T. Monfret (2008), Converted phases analysis for passive/active seismic data, *Conception, verification and application of innovative techniques to study active volcanoes*, 249.
- Latorre D., V. J., Monfret Tony, Lyon-Caen H. (2004), Converted seismic wave investigation in the Gulf of Corinth from local earthquakes, *Académie des sciences. Published by Elsevier SAS*, doi:10.1016/j.crte.2003.11.014.
- Le Meur, H., J. Virieux and P. Podvin (1997), Seismic tomography of the Gulf of Corinth: a comparison of methods, *Ann. Geophys.*, XL, 1-25.
- Le Pichon, X., C. Kreemer, and N. Chamot-Rooke (2005), Asymmetry in elastic properties and the evolution of large continental strike-slip faults, *Journal of Geophysical Research: Solid Earth (1978–2012)*, 110(B3).
- Lengliné, O., and J. L. Got (2011), Rupture directivity of microearthquake sequences near Parkfield, California, *Geophysical Research Letters*, 38(8).
- Lewis, M., Y. Ben-Zion, and J. J. McGuire (2007), Imaging the deep structure of the San Andreas Fault south of Hollister with joint analysis of fault zone head and direct P arrivals, *Geophysical Journal International*, 169(3), 1028-1042.
- Lewis, M., Z. Peng, Y. Ben-Zion, and F. Vernon (2005), Shallow seismic trapping structure in the San Jacinto fault zone near Anza, California, *Geophysical Journal International*, 162(3), 867-881.
- Lewis, M. A., and Y. Ben-Zion (2010), Diversity of fault zone damage and trapping structures in the Parkfield section of the San Andreas Fault from comprehensive analysis of near fault seismograms, *Geophysical Journal International*, 183(3), 1579-1595, doi:10.1111/j.1365-246X.2010.04816.x.
- Li, H., L. Zhu, and H. Yang (2007), High-resolution structures of the Landers fault zone inferred from aftershock waveform data, *Geophysical Journal International*, 171(3), 1295-1307.
- Li, X., V. F. Cormier, and M. N. Toksöz (2002), Complex Source Process of the 17 August 1999 İzmit, Turkey, Earthquake, *Bulletin of the Seismological Society of America*, 92(1), 267-277, doi:10.1785/0120000839.
- Li, Y.-G., P. Leary, K. Aki, and P. Malin (1990), Seismic trapped modes in the Oroville and San Andreas fault zones, *Science*, 249(4970), 763-767.

- Liu, Y., T.-L. Teng, and Y. Ben-Zion (2005), Near-surface seismic anisotropy, attenuation and dispersion in the aftershock region of the 1999 Chi-Chi earthquake, *Geophysical Journal International*, 160(2), 695-706.
- Lomnitz-Adler, J. (1991), Model for steady state friction, *Journal of Geophysical Research: Solid Earth*, 96(B4), 6121-6131, doi:10.1029/90JB02536.
- Lyakhovskiy, V., and Y. Ben-Zion (2009), Evolving geometrical and material properties of fault zones in a damage rheology model, *Geochemistry, Geophysics, Geosystems*, 10(11).
- Ma, K.-F., Y.-Y. Lin, S.-J. Lee, J. Mori, and E. E. Brodsky (2012), Isotropic events observed with a borehole array in the Chelungpu fault zone, Taiwan, *Science*, 337(6093), 459-463.
- Mayne, W. H. (1962), Common reflection point horizontal data stacking techniques, *Geophysics*, 27(6), 927-938, doi:10.1190/1.1439118.
- McClusky, S., S. Balassanian, A. Barka, C. Demir, S. Ergintav, I. Georgiev, O. Gurkan, M. Hamburger, K. Hurst, and H. Kahle (2000), Global Positioning System constraints on plate kinematics and dynamics in the eastern Mediterranean and Caucasus, *Journal of Geophysical Research: Solid Earth (1978–2012)*, 105(B3), 5695-5719.
- McGuire, J., and Y. Ben-Zion (2005), High-resolution imaging of the Bear Valley section of the San Andreas Fault at seismogenic depths with fault-zone head waves and relocated seismicity, *Geophysical Journal International*, 163(1), 152-164.
- Melosh, H. J. (1979), Acoustic fluidization: A new geologic process?, *Journal of Geophysical Research: Solid Earth*, 84(B13), 7513-7520, doi:10.1029/JB084iB13p07513.
- Michellini, A., and T. V. McEvilly (1991), Seismological studies at Parkfield. I. Simultaneous inversion for velocity structure and hypocenters using cubic B-splines parameterization, *Bulletin of the Seismological Society of America*, 81(2), 524-552.
- Milkereit, C., S. Zünbül, S. Karakisa, Y. Iravul, J. Zschau, M. Baumbach, H. Grosser, E. Günther, N. Umutlu, T. Kuru, E. Erkul, K. Klinge, M. Ibs von Seht, A. Karahan, (2000), Preliminary aftershock analysis of the Mw=7.4 Izmit and Mw=7.1 Düzce earthquake in Western Turkey. - In: Kozaci, Ö., Barka, A. (Eds.), in *The 1999 Izmit and Düzce Earthquakes: preliminary results*, edited by A. Barka, Kozaci, Ö., Akyüz, S pp. 179-187, Istanbul Technical University.
- Mizuno, T., and K. y. Nishigami (2006), Deep structure of the Nojima Fault, southwest Japan, estimated from borehole observations of fault-zone trapped waves, *Tectonophysics*, 417(3–4), 231-247, doi:https://doi.org/10.1016/j.tecto.2006.01.003.
- Monteiller, V., J.-L. Got, J. Virieux, and P. Okubo (2005), An efficient algorithm for double-difference tomography and location in heterogeneous media, with an application to the Kilauea volcano, *Journal of Geophysical Research: Solid Earth*, 110(B12), n/a-n/a, doi:10.1029/2004JB003466.
- Mora, P., and D. Place (1994), Simulation of the frictional stick-slip instability, *pure and applied geophysics*, 143(1), 61-87, doi:10.1007/bf00874324.
- Müller, G. (1985), The reflectivity method: a tutorial, *J. Geophys.*, 58, 153–174.
- Najdahmadi, B., M. Bohnhoff, and Y. Ben-Zion (2016), Bimaterial interfaces at the Karadere segment of the North Anatolian Fault, northwestern Turkey, *Journal of Geophysical Research: Solid Earth*.
- Najdahmadi, B. H., P.; Vavryčuk, V.; Bohnhoff, M.; (2017), Imaging Mudurnu Segment of the North Anatolian Fault Zone from Waveforms of Small Earthquakes., *Submitted to the Journal of Geophysical Research, Solid Earth*.
- Nishigami, K. y. (2000), Deep crustal heterogeneity along and around the San Andreas fault system in central California and its relation to the segmentation, *Journal of Geophysical Research: Solid Earth*, 105(B4), 7983-7998, doi:10.1029/1999JB900381.
- Nisii, V., A. Zollo, and G. Iannaccone (2004), Depth of a Midcrustal Discontinuity beneath Mt. Vesuvius from the Stacking of Reflected and Converted Waves on Local Earthquake Records, *Bulletin of the Seismological Society of America*, 94(5), 1842-1849, doi:10.1785/012003063.

- Oppenheimer, D. H., P. A. Reasenber, and R. W. Simpson (1988), Fault plane solutions for the 1984 Morgan Hill, California, earthquake sequence: Evidence for the state of stress on the Calaveras fault, *Journal of Geophysical Research: Solid Earth (1978–2012)*, 93(B8), 9007-9026.
- Örgülü, G., and M. Aktar (2001), Regional moment tensor inversion for strong aftershocks of the August 17, 1999 Izmit Earthquake (Mw=7.4), *Geophysical Research Letters*, 28(2), 371-374, doi:10.1029/2000GL011991.
- Ozakin, Y., Y. Ben-Zion, M. Aktar, H. Karabulut, and Z. Peng (2012), Velocity contrast across the 1944 rupture zone of the North Anatolian fault east of Ismetpasa from analysis of teleseismic arrivals, *Geophysical Research Letters*, 39(8).
- Özalaybey, S., M. Ergin, M. Aktar, C. Tapirdamaz, F. Biçmen, and A. Yörük (2002), The 1999 Izmit earthquake sequence in Turkey: seismological and tectonic aspects, *Bulletin of the Seismological Society of America*, 92(1), 376-386.
- Özeren, M. S., and W. E. Holt (2010), The dynamics of the eastern Mediterranean and eastern Turkey, *Geophysical Journal International*, 183(3), 1165-1184.
- Pantosti, D., S. Pucci, N. Palyvos, P. M. De Martini, G. D'Addezio, P. E. F. Collins, and C. Zabcı (2008), Paleoearthquakes of the Düzce fault (North Anatolian Fault Zone): Insights for large surface faulting earthquake recurrence, *Journal of Geophysical Research: Solid Earth*, 113(B1), n/a-n/a, doi:10.1029/2006JB004679.
- Papaleo, E., D. G. Cornwell, and N. Rawlinson (2017), Seismic tomography of the North Anatolian Fault: New insights into structural heterogeneity along a continental strike-slip fault, *Geophysical Research Letters*, 44(5), 2186-2193, doi:10.1002/2017GL072726.
- Parsons, T. (2004), Recalculated probability of $M \geq 7$ earthquakes beneath the Sea of Marmara, Turkey, *Journal of Geophysical Research: Solid Earth (1978–2012)*, 109(B5).
- Peng, Z., and Y. Ben-Zion (2004), Systematic analysis of crustal anisotropy along the Karadere—Düzce branch of the North Anatolian fault, *Geophysical Journal International*, 159(1), 253-274.
- Peng, Z., and Y. Ben-Zion (2005), Spatiotemporal variations of crustal anisotropy from similar events in aftershocks of the 1999 M7. 4 Izmit and M7. 1 Düzce, Turkey, earthquake sequences, *Geophysical Journal International*, 160(3), 1027-1043.
- Peng, Z., and Y. Ben-Zion (2006), Temporal changes of shallow seismic velocity around the Karadere-Düzce branch of the north Anatolian fault and strong ground motion, *Pure and Applied Geophysics*, 163(2-3), 567-600.
- Peng, Z., Y. Ben-Zion, A. J. Michael, and L. Zhu (2003), Quantitative analysis of seismic fault zone waves in the rupture zone of the 1992 Landers, California, earthquake: evidence for a shallow trapping structure, *Geophysical Journal International*, 155(3), 1021-1041, doi:10.1111/j.1365-246X.2003.02109.x.
- Pieter-Ewald Share, Y. B.-Z., Zachary E. Ross, Hongrui Qiu and Frank Vernon (2017), Internal structure of the San Jacinto fault zone at Blackburn Saddle from seismic data of a dense linear array.
- Prevedel, B., F. Bulut, M. Bohnhoff, C. Raub, R. F. Kartal, F. Alver, and P. E. Malin (2015), Downhole geophysical observatories: best installation practices and a case history from Turkey, *International Journal of Earth Sciences*, 104(6), 1537-1547, doi:10.1007/s00531-015-1147-5.
- Qiu, H., Y. Ben-Zion, Z. Ross, P.-E. Share, and F. Vernon (2017a), Internal structure of the San Jacinto fault zone at Jackass Flat from data recorded by a dense linear array, *Geophysical Journal International*, 209(3), 1369-1388.
- Qiu, H., Y. Ben-Zion, Z. Ross, P. Share, and F. Vernon (2015), Internal structure of the San Jacinto fault zone at Jackass Flat from earthquake data recorded by a dense linear array, paper presented at Abstract of the annual SSA meeting.

Ranjith, K., and J. Rice (2001), Slip dynamics at an interface between dissimilar materials, *Journal of the Mechanics and Physics of Solids*, 49(2), 341-361.

Rebaï, S., H. Philip, and A. Taboada (1992), Modern tectonic stress field in the Mediterranean region: evidence for variation in stress directions at different scales, *Geophysical Journal International*, 110(1), 106-140, doi:10.1111/j.1365-246X.1992.tb00717.x.

Reilinger, R., et al. (2006), GPS constraints on continental deformation in the Africa-Arabia-Eurasia continental collision zone and implications for the dynamics of plate interactions, *Journal of Geophysical Research: Solid Earth*, 111(B5), n/a-n/a, doi:10.1029/2005JB004051.

Revenaugh, J. (2000), The relation of crustal scattering to seismicity in southern California, *Journal of Geophysical Research: Solid Earth*, 105(B11), 25403-25422, doi:10.1029/2000JB900304.

Rockwell, T. K., and Y. Ben-Zion (2007), High localization of primary slip zones in large earthquakes from paleoseismic trenches: Observations and implications for earthquake physics, *Journal of Geophysical Research: Solid Earth*, 112(B10), n/a-n/a, doi:10.1029/2006JB004764.

Ross, Z., Y. Ben-Zion, and L. Zhu (2015), Isotropic source terms of San Jacinto fault zone earthquakes based on waveform inversions with a generalized CAP method, *Geophysical Journal International*, 200(2), 1269-1280.

Ross, Z. E., and Y. Ben-Zion (2014), Automatic picking of direct P, S seismic phases and fault zone head waves, *Geophysical Journal International*, 199(1), 368-381.

Rowe, C. D., and W. A. Griffith (2015), Do faults preserve a record of seismic slip: A second opinion, *Journal of Structural Geology*, 78, 1-26, doi:https://doi.org/10.1016/j.jsg.2015.06.006.

Rubin, A. M., and D. Gillard (2000), Aftershock asymmetry/rupture directivity among central San Andreas fault microearthquakes, *Journal of Geophysical Research: Solid Earth (1978–2012)*, 105(B8), 19095-19109.

Rudnicki, J. W., and J. R. Rice (2006), Effective normal stress alteration due to pore pressure changes induced by dynamic slip propagation on a plane between dissimilar materials, *Journal of Geophysical Research: Solid Earth*, 111(B10), n/a-n/a, doi:10.1029/2006JB004396.

Sanford, A. R., Ö. Alptekin, and T. R. Topozada (1973), Use of reflection phases on microearthquake seismograms to map an unusual discontinuity beneath the Rio Grande rift, *Bulletin of the Seismological Society of America*, 63(6-1), 2021-2034.

Saragiotis, C. D. (2002), PAI-S/K: A robust automatic seismic P phase arrival identification scheme, *IEEE Trans. Geosci. Remote Sens.*, 40, 1395–1404.

Sato, H., Fehler, M. C. (1998), Seismic wave propagation and scattering in the heterogeneous Earth, *AIP Press/Springer, New York*.

Schulte-Pelkum, V., and Y. Ben-Zion (2012), Apparent Vertical Moho Offsets under Continental Strike-Slip Faults from Lithology Contrasts in the Seismogenic Crust, *Bulletin of the Seismological Society of America*, 102(6), 2757-2763.

Seeber, L., J. G. Armbruster, N. Ozer, M. Aktar, S. Baris, D. Okaya, Y. Ben-Zion, and E. Field (2000), The 1999 earthquake sequence along the North Anatolia transform at the juncture between the two main ruptures, *The 1999 Izmit and Duzce Earthquakes: Preliminary Results*, 209-223.

Sengör, A., O. Tüysüz, C. Imren, M. Sakiñç, H. Eyidogan, N. Görür, X. Le Pichon, and C. Rangin (2005), The North Anatolian fault: A new look, *Annu. Rev. Earth Planet. Sci.*, 33, 37-112.

Share, P.-E., and Y. Ben-Zion (2016), Bimaterial interfaces in the south San Andreas Fault with opposite velocity contrasts NW and SE from San Gorgonio Pass, *Geophysical Research Letters*, 43(20), 10,680-610,687, doi:10.1002/2016GL070774.

Share, P.-E., Y. Ben-Zion, Z. E. Ross, H. Qiu, and F. Vernon (2017), Internal structure of the San Jacinto fault zone at Blackburn Saddle from seismic data of a linear array, *Geophysical Journal International*, ggx191.

- Share, P.-E., Y. Ben-Zion, Z. Ross, H. Qiu and F. Vernon (2015), Characterization of the San Jacinto Fault Zone northwest of the trifurcation area from dense linear array data, *Abstract of the annual SSA meeting*.
- Shearer, P. M. (2009), *Introduction to seismology*, edited, Cambridge University Press.
- Sibson, R. H. (1986), Rupture interaction with fault jogs, *Earthquake Source Mechanics*, 37, 157-167.
- Stein, R. S., A. A. Barka, and J. H. Dieterich (1997), Progressive failure on the North Anatolian fault since 1939 by earthquake stress triggering, *Geophysical Journal International*, 128(3), 594-604, doi:10.1111/j.1365-246X.1997.tb05321.x.
- Stein, S., and M. Wysession (2003), *An introduction to seismology, earthquakes, and earth structure*, John Wiley & Sons.
- Stierle, E., M. Bohnhoff, and V. Vavryčuk (2014a), Resolution of non-double-couple components in the seismic moment tensor using regional networks—II: application to aftershocks of the 1999 Mw 7.4 Izmit earthquake, *Geophysical Journal International*, 196(3), 1878-1888.
- Stierle, E., V. Vavryčuk, J. Šílený, and M. Bohnhoff (2014b), Resolution of non-double-couple components in the seismic moment tensor using regional networks—I: a synthetic case study, *Geophysical Journal International*, ggt502.
- Stroujkova, A., and P. Malin (2000), A magma mass beneath Casa Diablo? Further evidence from reflected seismic waves, *Bulletin of the Seismological Society of America*, 90(2), 500-511.
- Sun, W., and B. L. N. Kennett (2016), Receiver structure from teleseisms: Autocorrelation and cross correlation, *Geophysical Research Letters*, 43(12), 6234-6242, doi:10.1002/2016GL069564.
- Templeton, E. L., and J. R. Rice (2008), Off-fault plasticity and earthquake rupture dynamics: 1. Dry materials or neglect of fluid pressure changes, *Journal of Geophysical Research: Solid Earth*, 113(B9), n/a-n/a, doi:10.1029/2007JB005529.
- Thomson, W. T. (1950), Transmission of Elastic Waves through a Stratified Solid Medium, *Journal of Applied Physics*, 21(2), 89-93, doi:10.1063/1.1699629.
- Thurber, C., H. Zhang, F. Waldhauser, J. Hardebeck, A. Michael, and D. Eberhart-Phillips (2006), Three-Dimensional Compressional Wavespeed Model, Earthquake Relocations, and Focal Mechanisms for the Parkfield, California, Region, *Bulletin of the Seismological Society of America*, 96(4B), S38-S49, doi:10.1785/0120050825.
- Thurber, C. H. (1983), Earthquake locations and three-dimensional crustal structure in the Coyote Lake Area, central California, *Journal of Geophysical Research: Solid Earth*, 88(B10), 8226-8236, doi:10.1029/JB088iB10p08226.
- Thybo, H., T. Janik, V. Omelchenko, M. Grad, R. Gareltsky, A. Belinsky, G. Karatayev, G. Zlotzki, M. Knudsen, and R. Sand (2003), Upper lithospheric seismic velocity structure across the Pripyat Trough and the Ukrainian Shield along the EUROBRIDGE'97 profile, *Tectonophysics*, 371(1), 41-79.
- Tibi, R., G. Bock, Y. Xia, M. Baumbach, H. Grosser, C. Milkereit, S. Karakisa, S. Zünbül, R. Kind, and J. Zschau (2001), Rupture processes of the 1999 August 17 Izmit and November 12 Düzce (Turkey) earthquakes, *Geophysical Journal International*, 144(2), F1-F7.
- Udías, A. (2000), *Principles of Seismology*, Cambridge University Press, Cambridge, doi:DOI: 10.1017/CBO9781139164306.
- Vavryčuk, V., P. Hrubcová, M. Brož, and J. Málek (2004), Azimuthal variation of Pg velocity in the Moldanubian, Czech Republic: observations based on a multi-azimuthal common-shot experiment, *Tectonophysics*, 387(1-4), 189-203, doi:https://doi.org/10.1016/j.tecto.2004.06.015.
- Wadati, K., and S. Oki (1933), On the Travel Time of Earthquake Waves. (Part II), *Journal of the Meteorological Society of Japan. Ser. II*, 11(1), 14-28, doi:10.2151/jmsj1923.11.1_14.
- Wdowinski, S., B. Smith-Konter, Y. Bock, and D. Sandwell (2007), Diffuse interseismic deformation across the Pacific–North America plate boundary, *Geology*, 35(4), 311-314.

- Wechsler, N., E. E. Allen, T. K. Rockwell, G. Girty, J. S. Chester, and Y. Ben-Zion (2011), Characterization of pulverized granitoids in a shallow core along the San Andreas Fault, Littlerock, CA, *Geophysical Journal International*, 186(2), 401-417, doi:10.1111/j.1365-246X.2011.05059.x.
- Wechsler, N., T. K. Rockwell, and Y. Ben-Zion (2009), Application of high resolution DEM data to detect rock damage from geomorphic signals along the central San Jacinto Fault, *Geomorphology*, 113(1), 82-96.
- Weertman, J. (1980), Unstable slippage across a fault that separates elastic media of different elastic constants, *Journal of Geophysical Research: Solid Earth*, 85(B3), 1455-1461, doi:10.1029/JB085iB03p01455.
- Weertman, J. (2002), Subsonic type earthquake dislocation moving at approximately \times shear wave velocity on interface between half spaces of slightly different elastic constants, *Geophysical Research Letters*, 29(10), 109-101-109-104, doi:10.1029/2001GL013916.
- Wessel, P., and W. H. F. Smith (1998), New, improved version of generic mapping tools released, *Eos, Transactions American Geophysical Union*, 79(47), 579-579, doi:10.1029/98EO00426.
- Wu, R.-S. (2003), Wave Propagation, Scattering and Imaging Using Dual-domain One-way and One-return Propagators, *pure and applied geophysics*, 160(3), 509-539, doi:10.1007/pl00012548.
- Wu, C., Z. Peng, and Y. Ben-Zion (2009), Non-linearity and temporal changes of fault zone site response associated with strong ground motion, *Geophysical Journal International*, 176(1), 265-278, doi:10.1111/j.1365-246X.2008.04005.x.
- Wu, H., and J. M. Lees (1999), Three-dimensional P and S wave velocity structures of the Coso Geothermal Area, California, from microseismic travel time data, *Journal of Geophysical Research: Solid Earth*, 104(B6), 13217-13233, doi:10.1029/1998JB900101.
- Wu, J., J. A. Hole, J. A. Snoke, and M. G. Imhof (2008), Depth extent of the fault-zone seismic waveguide: effects of increasing velocity with depth, *Geophysical Journal International*, 173(2), 611-622, doi:10.1111/j.1365-246X.2008.03755.x.
- Yang H. (2015), Recent advances in imaging crustal fault zones: a review, *Earthquake Science*, 28(2), 151-162, doi:10.1007/s11589-015-0114-3.
- Yang, H., Z. Li, Z. Peng, Y. Ben-Zion, and F. Vernon (2014), Low-velocity zones along the San Jacinto Fault, Southern California, from body waves recorded in dense linear arrays, *Journal of Geophysical Research: Solid Earth*, 119(12), 8976-8990.
- Yang, W., Z. Peng, and Y. Ben-Zion (2009), Variations of strain-drops of aftershocks of the 1999 İzmit and Düzce earthquakes around the Karadere-Düzce branch of the North Anatolian Fault, *Geophysical Journal International*, 177(1), 235-246.
- Yang, W., Z. Peng, B. Wang, Z. Li, and S. Yuan (2015), Velocity contrast along the rupture zone of the 2010 Mw6.9 Yushu, China, earthquake from fault zone head waves, *Earth and Planetary Science Letters*, 416, 91-97.
- Yilmaz, Ö. (2001), *Seismic Data Analysis: Processing, inversion, and interpretation of seismic data*, Soc. of Explor. Geophys., doi:10.1190/1.9781560801580.
- Zaliapin, I., and Y. Ben-Zion (2011), Asymmetric distribution of aftershocks on large faults in California, *Geophysical Journal International*, 185(3), 1288-1304.
- Zhao, P., and Z. Peng (2008), Velocity contrast along the Calaveras fault from analysis of fault zone head waves generated by repeating earthquakes, *Geophysical Research Letters*, 35(1).
- Zhao, P., Z. Peng, Z. Shi, M. A. Lewis, and Y. Ben-Zion (2010), Variations of the velocity contrast and rupture properties of M6 earthquakes along the Parkfield section of the San Andreas fault, *Geophysical Journal International*, 180(2), 765-780.
- Zigone, D., Y. Ben-Zion, M. Campillo, and P. Roux (2015), Seismic tomography of the Southern California plate boundary region from noise-based Rayleigh and Love waves, *Pure and Applied Geophysics*, 172(5), 1007-1032.

List of Figures

Chapter 1: General Introduction

1.1: An example of bimaterial interface	2
---	---

Chapter 2: Theory

2.1: Different polarization of direct P and FZHW	7
2.2: Schematic diagram showing a bimaterial interface	9
2.3: Particle velocities at a given time.....	12
2.4: An example of previous investigations on FZHW analysis	14
2.5. A plane wave reaching an interface	16
2.6. Simple velocity model and the corresponding ray paths and travel-time curve.....	17
2.7. An incident P wave at a solid-solid boundary	18
2.8. Reflection coefficients at the boundary between country rock and a LVFZ	19
2.9. Example of various crustal phases and the corresponding ray traces	19
2.10 Example of travel-time curves and ray-tracing crustal models for regional earthquakes.....	20
2.11: Example of high-frequency velocity waveforms with converted SP phases	23

Chapter 3: Tectonic setting of areas of study

3.1. Areas of study	26
---------------------------	----

Chapter 4: Bimaterial interfaces at the Karadere segment of the North Anatolian Fault, northwestern Turkey

4.1. Karadere Fault and seismicity	32
4.2. Data analysis procedure	34
4.3. Preliminary results for station FP	35
4.4. FZHW and direct P wave detection based on particle motion analysis	38
4.5. FZRW and direct P wave detection based on particle motion analysis	40
4.6. Final vertical component waveforms recorded by station FP	41
4.7. Final vertical component seismograms of other stations	42 & 43
4.8. Distribution of final FZHW and FZRW events	44
4.9. Distribution of final events color-coded with differential times	45 & 46
4.10. Combined plot of all FZHW and P arrivals for all five stations	47
4.11. Thinned set of FZHW and P arrivals with and without moveout	48
4.12. Conceptual model	52

Chapter 5: Imaging Mudurnu Segment of the North Anatolian Fault Zone from Waveforms of Small Earthquakes

5.1. Mudurnu Fault and seismicity	57
5.2. Waveform processing for enhancing detection of secondary phases	59
5.3. Vertical component seismic sections after the waveform processing (cluster in the north)	60
5.4. Vertical component seismic sections after the waveform processing (cluster in the west)	61
5.5. Final Vertical seismograms of station GOK for different azimuths	63
5.6. Seismic section after the waveform processing at station (epicentral sorting)	64
5.7. Seismicity color-coded according to the amplitudes and consistency of secondary phases	65
5.8. Particle motion analysis	66
5.9. Synthetic sections for a horizontal interface	68
5.10. Synthetic section for the epicentral-sorted seismicity and a horizontal interface	69
5.11. Synthetic section for the depth-sorted seismicity and an inclined interface	70
5.12. Schematic sketch with horizontal and inclined interfaces	72
5.13. Conceptual model	73

Chapter 6: Further Remarks on FZHW analysis

6.1. NAFZ and the location of the very first studied station	76
6.2. Selection of events	76
6.3. Results of the manual analysis performed	77
6.4. Wadati plots	78

Curriculum Vitae

For reasons of data protection, the Curriculum vitae is not published in the online version.

Acknowledgements

I would like to thank my supervisor Prof. Marco Bohnhoff for supporting me, guiding me, for his encouragement and patience throughout my doctoral studies. It was also a great opportunity for me to be able to participate in many national and international conferences as well as in GONAF borehole installations. I was able to expand my knowledge in practice and got to know many other researchers throughout my PhD studies. I would also like to thank him for making it possible for me to collaborate with other great scientists for my PhD studies.

I am very grateful to Prof. Yehuda Ben-Zion, for all I learned from him about physics of earthquakes and faults, for his interest in my PhD project and for his support and guidance at conferences, through emails, as he visited us in GFZ and as I joined his group at the University of Southern California. I am also very grateful to Dr. Pavla Hrubcová and Dr. Vaclav Vavryčuk for their guidance, patience, fruitful discussions and for all I learned from them in their visits to GFZ and as I visited them in Prague.

A special thank goes to Dr. Amir Allam and Dr. Zachary Ross for providing codes for polarization analysis and automatic phase detection. Special thanks to Lion Krischer for helping me with my ObsPy questions and to other developers of the ObsPy open-source project.

I would like to thank the members of section 4.2, “Geomechanics and Rheology” of GFZ for all their help and all the good times we had. I especially thank Tina, Michele, Claudius, Christopher, Patricia, Grzegorz, Digidem, Eva, Marc, Elma and many others who are not mentioned here. A special thank goes to Professor Dresden for his support as well. I would also like to thank Dr. Fatih Bulut for his help and support in an early stage of my PhD. Last but not least, I would like to thank the Albert Einstein Park’s cat for –sometimes- being there too.

I appreciate all the help and support from friends and colleagues during my visit to the University of Southern California including Niloufar, Hongrui, Pieter, Xin, Marshall, Yaman, Dimitri and the Pohl family.

A special thank goes to Rita for her patience, great assistance and for creating such a warm atmosphere in her office and in other special gatherings of our section.

Finally, many thanks go to Jens, Homa, Hale, Julia, Samar, Helia, Siavash and Nassim. Most importantly, I would like to thank my family, Minoo, Cyrus and Tara for all their love, enthusiasm and encouragement. Your great support and understanding helped me throughout every step of my life and my PhD studies.